INTERACTION OF GROUNDWATER FLOW SYSTEMS AND THERMAL REGIMES IN MOUNTAINOUS TERRAIN: A NUMERICAL STUDY

By

CRAIG BURTON FORSTER

B.Sc., The University of British Columbia, 1975

M.Sc., The University of Waterloo, 1979

A THESIS SUBMITTED IN PARTIAL FULFILLMENT OF
THE REQUIREMENTS FOR THE DEGREE OF
DOCTOR OF PHILOSOPHY

in

THE FACULTY OF GRADUATE STUDIES
(Department of Geological Sciences)

We accept this thesis as conforming
to the required standard

THE UNIVERSITY OF BRITISH COLUMBIA

October 1987

In presenting this thesis in partial fulfilment of the requirements for an advanced degree at the University of British Columbia, I agree that the Library shall make it freely available for reference and study. I further agree that permission for extensive copying of this thesis for scholarly purposes may be granted by the head of my department or by his or her representatives. It is understood that copying or publication of this thesis for financial gain shall not be allowed without my written permission.

Department of GEOLOGICAL SCIENCES

The University of British Columbia
1956 Main Mall
Vancouver, Canada
V6T 1Y3

Date October 15, 1987

ABSTRACT

It is widely recognized that topographically-driven groundwater flow can perturb conductive thermal regimes. High-relief topography amplifies the impact of factors controlling groundwater flow and advective heat transfer. A finite element method is developed to model the influence of geology, climate, surface topography and regional heat flux on steady groundwater flow and heat transfer. Because fluid viscosity (hence fluid flux) depends upon temperature, groundwater flow is influenced by the regional heat flux. As a consequence, isothermal approaches to modeling deep groundwater flow in mountains may be inappropriate. Using a free-surface approach, the water table is represented as an internal characteristic of the groundwater flow system, rather than the upper boundary for fluid flow. Thick unsaturated zones are expected in high-permeability terrain (greater than 10^{-15} m^2) with arid climate, or where groundwater recharge is restricted by extensive alpine glaciers. Only vertical fluid flow is assumed to occur in the unsaturated zone, therefore, heat transfer above the water table is represented by one-dimensional advection and two-dimensional conduction. Simulation results indicate that water table elevations are highly sensitive to changes in the controlling factors, but have little impact on the thermal regime. Conductive thermal regimes are predicted in low-permeability terrain (less than 10^{-18} m^2) or in high-permeability terrain with arid climate (recharge rates

less than 10^{-11} m/sec). Strong advective heat transfer masks the regional heat flux when permeability exceeds 10^{-16} m^2 in terrain with relief of 2 km over a horizontal distance of 6 km. Less than one percent of typical mean annual precipitation is transmitted through deep groundwater flow systems under these conditions. Asymmetric surface topography complicates efforts to interpret chemical and thermal data collected near the valley floor. Fracture zones outcropping at the valley floor can capture a large percentage of groundwater flowing through the system and a significant percentage of the basal heat flux. Maximum spring temperatures are indicated when bulk permeability is between 10^{-17} m^2 and 10^{-15} m^2. Outside this range, spring temperatures approach ambient air temperature. Topographically-driven groundwater flow can distort and obliterate free-convection cells that might otherwise develop within a mountain massif.

TABLE OF CONTENTS

TABLE OF CONTENTS - Cont'd

TABLE OF CONTENTS - Cont'd

LIST OF TABLES

LIST OF FIGURES

LIST OF FIGURES - Cont'd

LIST OF FIGURES - Cont'd

ACKNOWLEDGEMENTS

It is with great pleasure that I acknowledge the generous supply of insight, encouragement and financial support provided by Leslie Smith throughout the course of this project. This research has benefitted from the many hours spent discussing the thermal implications with David Chapman. I would also like to thank Allan Freeze and Gedeon Dagan for sharing their views on the development of seepage faces in mountainous terrain and the use of hodograph methods. Brian Fairbank and the staff of Nevin Sadlier-Brown Goodbrand Co. Ltd. (NSBG) are to be thanked for taking an active interest in this research and providing access to their office facilities and technical library. The efforts of my supervisory committee Tom Brown, Allan Freeze and John Ross are gratefully acknowledged. Thanks are extended to Charles Mase for providing the software to compute water properties and to Gord Hodge for drafting the figures. This work was funded by grants from the Natural Sciences and Engineering Research Council of Canada (NSERC) and a GREAT award provided by the British Columbia Science Council (in cooperation with NSBG). Computations were carried out on an FPS 164/MAX Array Processor supported by an NSERC Major Installation Grant to the University of British Columbia.

CHAPTER 1

INTRODUCTION

Recent interest in the thermal regimes of mountains has developed in response to continuing studies of the earth's thermal state and the desire to exploit geothermal energy resources. A number of thermal data sets collected in mountainous terrain indicate a strong advective disturbance of conductive thermal regimes by groundwater flow (Black *et al.*, 1983; Mase *et al.*, 1982; Reader and Fairbank, 1983). This disturbance complicates the interpretion of borehole temperature logs used in estimating regional heat flow and may mask the thermal signature of underlying geothermal systems. When interpreting a thermal data set, or developing conceptual models of geothermal systems in mountainous terrain, it is essential that the potential impact of groundwater flow be addressed.

Conductive thermal regimes are modified when heat is redistributed by fluid flow. Fluid flow may be driven by topographic relief in regional groundwater flow systems (advection or forced-convection), by temperature-induced density contrasts in regions of high heat flow (thermal buoyancy-driven or free-convection) or by a combination of both mechanisms. Studies of buoyancy-driven flow systems in

flat topography are reviewed by Cheng (1978). These studies, common in the geothermal literature, emphasize fluid circulation within a localized region of the flow system (or within a geothermal reservoir) and neglect the possible influence of advective heat transfer by regional groundwater flow. Early efforts to examine the influence of regional flow are described by Prats (1966) and Elder (1967). Using numerical methods, they show how free-convection cells can be modified and obliterated when arbitrarily-defined external flows are imposed on simple buoyancy-driven flow systems. Model studies that attempt to link, in a quantitative manner, a thermal disturbance with the regional groundwater flow system are presented by Faust *et al.*, (1984), Blackwell (1985), and Sorey (1985a), among others.

Interest in the thermal regimes of sedimentary basins has prompted field analyses, and model studies, that recognize the influence of topographically-driven groundwater flow on heat transfer in low-relief terrain. Typical field studies are described by Majorowicz *et al.* (1985) and Gosnold (1985). Model studies are presented by Domenico and Palciauskas (1973), Smith and Chapman (1983, 1985), Garven and Freeze (1984), and Woodbury and Smith (1985).

It is commonly recognized that topographically-driven groundwater flow causes advective heat transfer in

mountainous terrain. The details of groundwater flow within the mountain massif, however, are poorly understood. Upper regions of flow have been explored, to a limited extent, in field studies that emphasize the interface between surface hydrology and shallow groundwater flow (Halstead, 1969; Sklash and Farvolden, 1979; Bortolami *et al.*, 1979; Martinec *et al.*, 1982; Smart, 1985). Although these studies provide insight into the hydrology of alpine watersheds and the relationships between water table fluctuations and seasonal snowmelt, they yield little information on the deep flow systems that control advective heat transfer in mountainous terrain.

Information on the character and distribution of permeable zones within a mountain massif is available in reports describing inflows to alpine tunnels (Schadt, 1905; Fox, 1907; Hennings, 1910; Keays, 1928; Mears, 1932). Unfortunately, measurements of fluid pressure that could aid in defining the nature of mountain flow systems are generally lacking. Jamier (1975) assessed the hydraulic characteristics of fractured crystalline rock deep within Mount Blanc (France) on the basis of geochemical and hydraulic data obtained during construction of a highway tunnel, yet an integrated description of the flow system within the mountain massif was not attempted. Summit water table and hydraulic head data are rare because most wells and boreholes are located on the lower flanks of mountain slopes. Two summit water level measurements are noted in the

literature; at a depth of 30 m in fractured crystalline rock at Mt. Kobau, B.C. (Halstead, 1969) and at a depth of 488 m in the basalts of Mt. Kilauea, Hawaii (Zablocki *et al.*, 1974).

Numerical studies of mountain-scale flow systems have been presented by Jamieson and Freeze (1983) and Ingebritsen and Sorey (1985). Jamieson and Freeze (1983) used a free-surface model and a water budget approach to estimate the range of hydraulic conductivity that might be found within Meager Mountain, British Columbia. Ingebritsen and Sorey (1985) incorporate the influence of high-relief topography in their numerical model of advection-dominated heat transfer at Mt. Lassen, California. In using a basal source of heated fluid to represent the circulation and heating of groundwater recharged on the mountain flanks, the relationship between the magnitude of the fluid source and rates of groundwater recharge at the ground surface is poorly defined. In this thesis, a modeling approach is adopted that specifies recharge to the flow system as infiltration at the ground surface and solves for the temperature of groundwater circulating through a mountain massif.

The nature of deep groundwater flow is of particular interest in studies of geothermal systems in mountainous terrain. Groundwater samples obtained from springs and boreholes during geothermal exploration often provide

geochemical indications of a resource at depth. Identifying the source of a chemical signature requires an understanding of the rates and patterns of groundwater flow. Efforts to identify a geothermal resource also rely on temperature data collected in shallow boreholes. Unfortunately, advective disturbance of conductive thermal regimes by groundwater flow can complicate the interpretation of borehole temperature logs and may mask the thermal signature of an underlying resource. Geochemical and thermal data have been used by several workers (Lahsen and Trujillo, 1975; Blackwell and Steele, 1983; Sorey, 1985b) to form generalizations on the nature of mountain hydrothermal systems. A comprehensive, quantitative analysis of groundwater flow systems in mountainous terrain has yet to be reported in the literature.

The objective of this thesis is to investigate the nature of topographically-driven groundwater flow systems in mountainous terrain and their influence on conductive thermal regimes. A numerical modeling approach provides a quantitative basis for examining the influence of factors controlling the rates and patterns of groundwater flow and heat transfer. In this study, idealized mountainous terrain is modeled for a range of conditions representative of the Western Cordillera in North America. Mountainous terrain is defined as rugged topography with local relief in excess of 600 m (Thompson, 1964). In the Coast Mountains of British Columbia and the central Cascades of the Pacific Northwest,

topographic relief of 2 km over a horizontal distance of 6 km is typical. In the Rocky Mountains of Canada and U.S.A., a more subdued relief of 1 km over 6 km is not uncommon. Vertical sections and schematic groundwater pathlines representative of the Coast Mountains of British Columbia and the Rocky Mountains at the Alberta-British Columbia border are shown in Figures 1.1a and 1.1b. For comparison, Figure 1.1c shows flow systems in a low-relief topography similar to those described by Freeze and Witherspoon (1967).

Groundwater flow systems in mountains differ from those found in low-relief terrain in two important respects:

1. For a given set of conditions, with greater topographic relief a greater range in water table elevation and form is possible. In low-relief terrain, water table configurations can be defined with reasonable accuracy using water level elevations and hydraulic head data obtained from boreholes and wells located across the region of interest. In many instances, estimated water table elevations are used in defining the upper boundary of regional flow systems. In mountainous terrain measured water table elevations and hydraulic head data are sparse and, where available, usually concentrate on the lower flanks of mountain slopes. This restricted distribution of data leads to considerable uncertainty in defining water table configurations beneath

mountain summits.

2. High-relief terrain enhances groundwater circulation to depths where elevated subsurface temperatures may be encountered. Waring, 1965; Souther and Halstead, 1973 invoke this mechanism to explain the presence of thermal springs in mountain valleys where the regional heat flux differs little from the normally accepted median of 60 mW/m^2. Variation in temperature has a strong effect on fluid density and viscosity that, in turn, have an important influence on the rates and patterns of groundwater flow. Thermally-induced differences in fluid density produce a buoyancy-driven component of fluid flow that enhances vertical movement of groundwater. In addition, reduced fluid viscosity in regions of elevated temperature contributes to increased rates of groundwater flow.

Chapter 2 explains how the character of mountainous terrain is incorporated in a conceptual model for fluid flow and heat transfer. The numerical method used here differs from those of previous work because a free-surface approach is used in a non-isothermal formulation to estimate water table elevations within a mountain massif. Important aspects of the conceptual and numerical models are summarized at the conclusion of Chapter 2. In Chapters 3 and 4, the numerical model is used to examine the interaction of groundwater flow and heat transfer in mountainous terrain. Numerical results presented in Chapter 3 illustrate the influence of geology,

climate, surface topography and regional heat flux on water table elevations and the pattern and magnitude of groundwater flow. Numerical results presented in Chapter 4 illustrate the impact of topographically-driven groundwater flow on thermal regimes and the role that advective heat transfer plays in masking the regional heat flux. Conditions leading to the development of free-convection cells within a mountain massif are also considered. Conclusions presented at the end of Chapters 3 and 4 are summarized in Chapter 5.

REFERENCES

Black, G.L., D.D. Blackwell, and J.L. Steele, Heat flow in the Oregon Cascades, in Geology and Geothermal Resources of the Central Oregon Cascades Range, ed. by G.R. Priest and B.F. Vogt, Oregon Dept. of Geol. and Min. Ind., Special Paper 15, 69-76, 1983.

Blackwell, D.D., A transient model of the geothermal system of Long Valley Calder, California, Jour. Geophys. Res., 90, 11229-11242, 1985.

Blackwell, D.D., and J.L. Steele, A summary of heat flow studies in the Cascade Range, Geoth. Resources Council Trans., 7, 233-236, 1983.

Bortolami, G.S., B. Ricci, G.G. Susella, and G.M. Zuppi, Hydrogeochemistry of the Corsaglia Valley, Maritime Alps Piedmont Italy, Jour. of Hydrol., 44, 57-79, 1979.

Cheng, P., Heat transfer in geothermal systems, Adv. in Heat Transfer, Vol. 14, 1-105, 1978.

Domenico,P.A. and V.V. Palciauskas, Theoretical analysis of forced convective heat transfer in regional ground-water flow, Geol. Soc. Amer., Bulletin 84, 3303-3814, 1973.

Elder, J.W., Steady free convection in a porous medium heated from below, J. Fluid Mech., 27, 29-48, 1967.

Faust, C.R., J.W. Mercer, S.D. Thomas, and W.P. Balleau, Quantitative analysis of existing conditions and production strategies for the Baca Geothermal System, New Mexico, Water Resour. Res., 20(5), 601-618, 1984.

Fox, F.M., The Simplon tunnel, Minutes of the Proceedings of the Inst. of Civil Engineers, 168, 61-86, 1907.

Freeze, R.A., and P.A. Witherspoon, Theoretical analysis of regional groundwater flow: 2. Effect of water-table configuration and subsurface permeability variation, Water Resour. Res., 3, 623-634, 1967.

Garven, G. and R.A. Freeze, Theoretical analysis of the role of groundwater flow in the genesis of stratabound ore deposits: 2. Quantitative results, Am. Jour. Sci., 284, 1125-1174, 1984.

Gosnold, W.D., Heat flow and ground water flow in the great plains of the United States, Jour. of Geodynamics, 4, 247-264, 1985.

Halstead, E.C., Groundwater investigation, Mount Kobau, British Columbia, Canada Inland Waters Branch, Dept. of Energy Mines and Resources, Tech. Bull. 17, 1969.

Hennings, F., On the question of long railway tunnels Construction, ventilation and operation, Bull. of the Internl. Railway Congress Assoc., 24(10), 943-983, 1910.

Ingebritsen, S.E., and M.L. Sorey, A quantitative analysis of the Lassen hydrothermal system, North Central California, Water Resour. Res., 21(6), 853-868, 1985.

Jamier, D., Etude de la fissuration, de l'hydrogeologie et de la geochemie des eaux profondes des massifs de l'Arpille et du Mont Blanc, PhD. dissertation, Faculte des Sciences, Universite de Neuchatel, Switzerland (in French), 1975.

Jamieson, G.R., and R.A. Freeze, Determining hydraulic conductivity distributions in a mountainous area using mathematical modeling, Groundwater, 21(2), 168-177, 1983.

Keays, R.N., Construction methods in the Moffat Tunnel, Amer. Soc. Civil Eng., 62, 63-112, 1928.

Lahsen, A., and P. Trujillo, The geothermal field of El Tatio, Chile, Proc. 2nd. U.N. Symp. on Development and Use of Geothermal Resources, San Francisco, Calif., Vol. 1, 157-175, 1975.

Majorowicz, J.A., F.W. Jones, H.L. Lam, and A.M. Jessop, Terrestrial heat flow and geothermal gradients in relation to hydrodynamics in the Alberta Basin, Canada, Jour. Geodynamics, 4, 265-283, 1985.

Martinec, J., H. Oeschager, U. Schotterer, and U. Siegenthaler, Snowmelt and groundwater storage in an alpine basin, in, Hydrological Aspects of Alpine and High Mountainous Terrain, ed. J. W. Glen, IAHS Publ. 138, 169-175, 1982.

Mase, C.W., J.H. Sass, A.H. Lachenbruch, and J.R. Munroe, Preliminary heat-flow investigations of the California Cascades, U.S. Geol. Survey, Open-File Report 82-150. 1982

Mears, F., The eight mile Cascade Tunnel, Great Northern Railway Part II. Surveys, construction methods and a comparison of routes, Amer. Soc. Civil Eng., Trans., 96, 915-1004, 1932.

Prats, M., The effect of horizontal fluid flow on thermally induced convection currents in porous mediums, Jour. Geophys. Res., 71(2), 4835-4837, 1966.

Reader, J.F., and Fairbank, B.D., Heat flow in the vicinity of the Meager Volcanic Complex, Southwestern British Columbia, Geoth. Resour. Council Trans., Vol. 7, 535-539, 1983.

Schadt, M.H., Les resultats scientifiques du percement du tunnel du Simplon, Bulletin Technique de la Suisse Romande, 125-178, 1905.

Sklash, M.G., and R.N. Farvolden, The role of groundwater in storm runoff, Jour. of Hydrol., 43, 45-65, 1979.

Smart, C.C., The hydrology of the Castleguard Karst, Columbia Icefields, Alberta, Canada, Arctic and Alpine Research, 15(4), 471-486, 1985.

Smith, L., and D.S. Chapman,The influence of water table configuration on the near-surface thermal regime, Jour. of Geodynamics, 4, 183-198, 1985.

Smith, L., and D.S. Chapman, On the thermal effects of groundwater flow 1. Regional scale systems, Jour. Geophys. Res., 88(B1), 593-608, 1983.

Sorey, M.L., Evolution and present state of the hydrothermal system in Long Valley Caldera, Jour. Geophys. Res., 90, 11219-11228, 1985a.

Sorey, M.L., Types of hydrothermal convection systems in the Cascade Range of California and Oregon, Proc. Workshop on Geothermal Resources of the Cascade Range, ed. M. Guffanti and L.J.P. Muffler, 63-67, 1985b.

Souther, J.G., and Halstead, E.C., Mineral and thermal waters of Canada, Canada Dept. of Energy, Mines and Resources, Paper 73-18, 1973.

Thompson, W.T., How and why to distinguish between mountains and hills, Prof. Geographer, 16, 6-8, 1964.

Waring, G.A., Thermal springs of the United States and other countries of the world - a summary, U.S. Geol. Survey Prof. Paper 492, 1965.

Woodbury, A.D., and L. Smith, On the thermal effects of three-dimensional groundwater flow, Jour. Geophys. Res., 90, 759-767, 1985.

Zablocki. C.J., R.I. Tilling, D.W. Peterson, R.L. Christiansen, G.V. Keller, and J.C. Murray, A deep research hole at the summit of an active volcano, Kilauea, Hawaii, Geoph. Res. Lett., 1(7), 323-326, 1974.

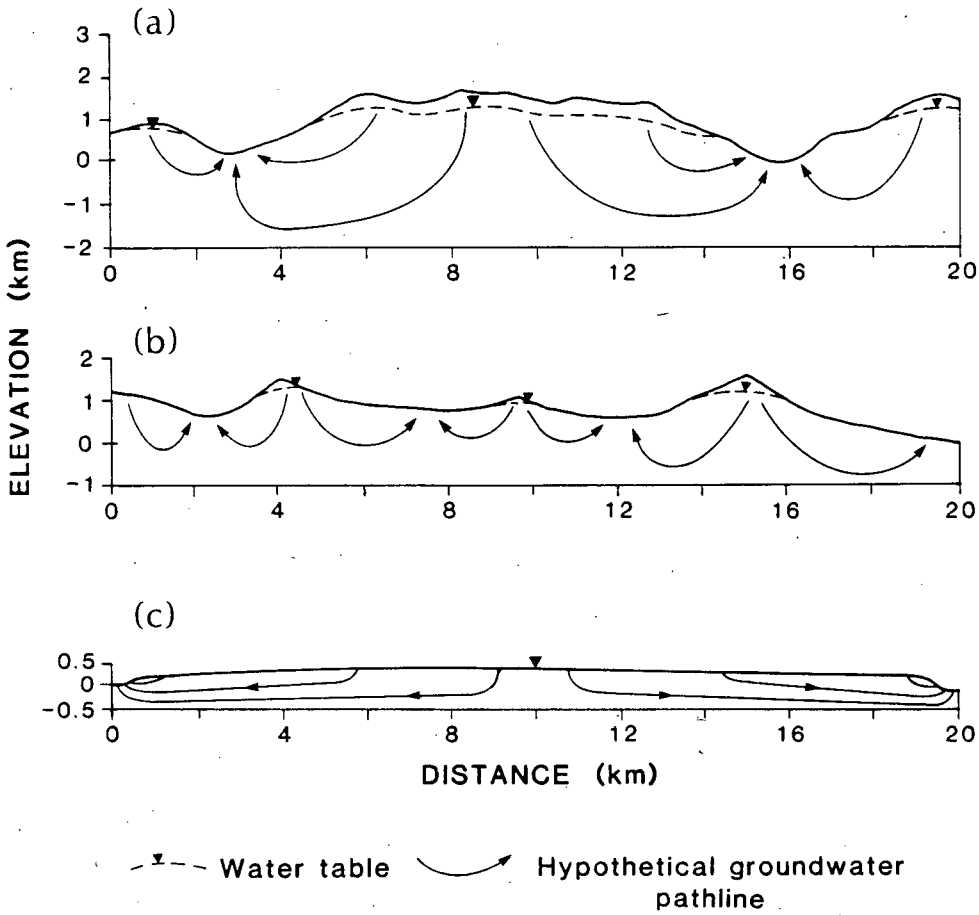

Figure 1.1. Hypothetical groundwater flow systems for homogeneous permeability;
a. Coast Mountains of British Columbia,
b. Rocky Mountains of B.C.-Alberta and
c. conventional low-relief terrain after Freeze and Witherspoon, 1967.

CHAPTER 2

DEVELOPMENT OF THE NUMERICAL METHOD

2.1 INTRODUCTION

This chapter describes the conceptual model, mathematical formulation and numerical method developed to simulate steady groundwater flow and heat transfer in mountainous terrain. The method adopted here differs from those used by previous workers because water table elevations are found as part of a solution process that accounts for fluid flux and heat transfer in the unsaturated zone. This approach is particularly useful when studying regions where limited groundwater recharge causes deep water tables and thick unsaturated zones. In this approach, recharge rates are controlled as an input variable, rather than implicitly calculated in the solution process. As a consequence, recharge rates consistent with the climatic conditions within the region of interest can be ensured. In addition, results of sensitivity analyses performed with this method are unaffected by the changes in recharge rate that would normally result when changing simulation parameters such as permeability.

2.2 CONCEPTUAL MODEL

A schematic of the boundary value problem adopted in this study is shown, without vertical exaggeration, in Figure 2.1. The upper boundary of the domain is the bedrock surface. Erosional processes operating in mountainous terrain often promote development of a thin cover of discontinuous surficial deposits (often less than 10 m thick) over upland areas of mountain slopes. In this conceptual model, these deposits are thought of as a thin skin of variable thickness that is not explicitly included in the model. Subsurface flow within this skin, in addition to overland flow and evapotranspiration, is lumped in a single runoff term. These processes are strongly affected by spatial variations in precipitation, slope angle and soil permeability as well as by temporal variations in precipitation events. Field observations of the complex nature and interaction of these factors are lacking for individual mountain slopes. As a first approximation, therefore, a lumped steady state approach is adopted and an available infiltration rate is defined. Available infiltration (I_z) represents the maximum rate of recharge possible at the bedrock surface for specified climatic, geologic and topographic conditions. In the absence of detailed site data, the available infiltration rate is best thought of as a percentage of the mean annual precipitation

rate. Although the units of I_z are m/sec, this parameter actually expresses the volumetric flux of fluid across a horizontal plane (m^3/sec per m^2).

Recharge to the flow system reflects the magnitude of the available infiltration rate, the capacity for fluid flow through the system and the nature of the thermal regime. In high permeability terrain, groundwater flow systems may accept all the available infiltration and produce a water table that lies below the bedrock surface (Figure 2.1). In lower permeability terrain, where recharge accepted by the flow system is less than available infiltration, the water table will be found close to the bedrock surface.

Conventional approaches to modeling regional groundwater flow (Freeze and Witherspoon, 1967) recognize that a transition from groundwater recharge to groundwater discharge occurs at a specified point on the upper boundary. In this study, this point is termed the hinge point (HP shown in Figure 2.1). Because a simplified representation of the unsaturated zone is included in this conceptual model it is also necessary to identify the point where the water table meets the bedrock surface. This point is defined as a point of detachment (POD shown in Figure 2.1). In developing numerical models to analyze seepage through earth dams, an exit point is commonly defined that has the properties of both the POD and the HP. In high-relief terrain, the usual exit point cannot be identified because the POD and HP no

longer coincide. In the region between the point of detachment and the hinge point, the water table coincides with the bedrock surface and the saturated zone is recharged directly from overlying surficial deposits or by precipitation falling on the bedrock surface. This suprising result implies that recharge can occur on what is usually considered to be the seepage face. This behavior is discussed in more detail in a subsequent section and in Appendix II.

Upslope of the point of detachment, the water table lies below the bedrock surface and infiltration is transferred to the water table by unsaturated flow. Although significant lateral flow in the unsaturated zone may cause patterns of recharge at the water table to differ from patterns of infiltration at the bedrock surface, the nature and magnitude of lateral flow in unsaturated regions of mountain flow systems is poorly understood. In this study, a one-dimensional model of vertical flow from the bedrock surface to the water table is adopted. This approach clearly oversimplifies the complex factors controlling fluid flow in regional-scale unsaturated zones. Before a more realistic approach can be adopted, however, additional research involving both field-based and theoretical studies must be carried out.

Boundaries of the thermal regime coincide with those of the fluid flow system. A basal conductive heat flow supplies

thermal energy to the mountain flow system. The basal heat flow, that represents heat transfer from deeper levels in the earth's crust, is a characteristic of the tectonic environment in which the mountain is located. Chapman and Rybach (1985) report that representative heat flow values range from 30 to 150 mW/m^2 with a median of 61 mW/m^2. Following the example of Birch (1950), it is assumed that temperatures at the ground surface reflect an altitudinal gradient in surface temperature (thermal lapse rate) with mean annual temperatures at the ground surface a few degrees warmer than mean annual air temperature. Smith (1975) and Barry (1981, pg. 74) indicate that the difference between mean annual soil temperature and mean annual air temperature is strongly controlled by microclimate. As a consequence, this temperature difference may range from less than 1 K to in excess of 15 K, on a mean annual basis. In the sensitivity studies performed in this thesis, mean annual ground temperatures are assumed to be controlled only by variations in elevation within the range 0 to 15°C.

In this study, fixed temperatures are not specified where fracture zones outcrop to produce groundwater springs. In such cases, temperature at the ground surface is assumed to reflect the temperature of groundwater flowing in the fracture zone, rather than the air temperature. In developing the fluid flow component of this conceptual model it is assumed that only a thin skin of surficial deposits is likely to be found on mountain slopes. The resistance to

heat transfer through the surficial deposits is assumed to cause only minor changes in temperature, therefore, temperatures at the bedrock surface are presumed to match temperatures at the ground surface.

Heat transfer occurs by conduction and advection both above and below the water table, therefore, the influence of fluid flow on the thermal regime in the unsaturated zone must be considered. In the model presented here, only the thermal effects of moisture movement in the liquid phase are considered here. Thermal effects of condensation, evaporation and heat transfer by vapor movement within the unsaturated zone are neglected. In developing a conceptual model of deep unsaturated zones, Ross (1984) suggests that moisture transport by vapor movement becomes negligible when recharge rates exceed about 10^{-12} m/sec. Unsaturated zones with recharge rates less than this amount are likely found only in the most arid of climates. Because such arid conditions are few in mountainous terrain of the Western Cordillera, the influence of vapor movement on moisture and heat transport in the unsaturated zone is neglected and a minimum infiltration rate of 10^{-12} m/sec is assumed.

Although fractures are assumed to provide the primary pathways for groundwater flow through a mountain massif, an equivalent porous medium approach is adopted. This approach is reasonable where the length and spacing of individual fractures is generally much smaller than the scale of the

mountain massif. An equivalent porous media approximation is often adopted in studies where limited field data preclude a more rigorous approach. In keeping with this lumped approach, groundwater discharge is represented as seepage distributed across the discharge area (downslope of the HP in Figure 2.1) rather than at isolated groundwater springs. Local variations in surface topography, permeability, and thickness of surficial deposits controlling the distribution of springs are assumed to have little effect on the overall pattern and magnitude of groundwater flow. Exceptions to this assumption are major through-going fracture zones represented as discrete permeable fracture zones with a homogeneous permeability k_f and width b (Figure 2.1). An important component of this study involves assessing the impact of through-going fracture zones on groundwater flow systems and springs.

2.3 MATHEMATICAL MODEL

The mathematical model for groundwater flow and heat transfer in mountains is expressed by two coupled partial differential equations describing fluid flow and heat transfer, by equations of state for the fluid properties, and by boundary conditions for both the fluid and thermal problems. Note that in the conceptual model outlined in Figure 2.1, a free-surface exists where the water table lies below the bedrock surface. Appendix I contains a table of nomenclature used in the following discussion.

The steady state equation of fluid mass conservation in the absence of internal sources and sinks is given by:

$$\frac{\partial}{\partial x}[\rho_f \cdot q_x] + \frac{\partial}{\partial z}[\rho_f \cdot q_z] = 0 \qquad (2.1)$$

where ρ_f is fluid density and q_x, q_z are horizontal and vertical components of fluid flux (specific discharge). Fluid flow is driven by gradients in fluid pressure and thermally-induced density contrasts. Fluid potential h is defined in terms of an equivalent freshwater head:

$$h = \frac{p}{\rho_o g} + z \qquad (2.2)$$

where ρ_0 is a reference fluid density at a specified temperature, g is acceleration due to gravity, p is fluid pressure and z is the elevation where the freshwater head is calculated. Frind (1982) advocates the use of an equivalent freshwater head in order to describe potential gradients exclusive of static fluid pressures.

Fluid flux through the saturated porous matrix is given by:

$$q_i = - \frac{k_{ij}}{\mu} [\rho_o g \frac{\partial h}{\partial x_j} + (\rho_f - \rho_o) g \frac{\partial z}{\partial x_j}] \qquad (2.3)$$

where μ is the dynamic viscosity of the fluid and k_{ij} is the permeability tensor for the porous matrix. This equation is simplified by defining a relative density

$$\rho_r = \frac{\rho_f}{\rho_o} - 1 \qquad (2.4)$$

to obtain:

$$q_i = -k_{ij} \frac{\rho_o g}{\mu} \left[\frac{\partial h}{\partial x_j} + \rho_r \frac{\partial z}{\partial x_j} \right] \tag{2.5}$$

In thin fracture zones and discrete fractures, fluid flux in direction s parallel to the fracture-matrix boundary is given:

$$q_s = -k_f \frac{\rho_o g}{\mu} \left[\frac{\partial h}{\partial s} + \rho_r \frac{\partial z}{\partial s} \right] \tag{2.6}$$

where k_f is the permeability of material within a discrete fracture or fracture zone. For open fractures, a parallel plate model is used to define the fracture permeability in terms of an effective aperture b where $k_f = b^2/12$ (Freeze and Cherry, 1979). In this study, only fractures within the saturated region of flow are considered.

The equation describing the distribution of freshwater head in the porous matrix is obtained by substituting equation (2.5) into equation (2.1):

$$\frac{\partial}{\partial x} \left[k_{xx} \rho_f \frac{\rho_o g}{\mu} \frac{\partial h}{\partial x} + k_{xz} \rho_f \frac{\rho_o g}{\mu} \frac{\partial h}{\partial z} \right] + \frac{\partial}{\partial z} \left[k_{zx} \rho_f \frac{\rho_o g}{\mu} \frac{\partial h}{\partial x} + k_{zz} \rho_f \frac{\rho_o g}{\mu} \left(\frac{\partial h}{\partial z} + \rho_r \right) \right] = 0 \tag{2.7}$$

The cross-terms for the permeability tensor (k_{xz}, k_{zx}) are included to preserve the generality of the subsequent numerical formulation. The analagous equation in one-dimensional local coordinates for a fracture zone is

$$\frac{\partial}{\partial s}\left(k_f \rho_f \frac{\rho_o g}{\mu}\left[\frac{\partial h}{\partial s} + \rho_r \frac{\partial z}{\partial s}\right]\right) = 0 \qquad (2.8)$$

Boundary conditions for the fluid flow system shown in Figure 2.1 are as follows:

$$\frac{\partial h}{\partial x} = 0 \qquad \text{for } -4 \text{ km} \le z \le z_x^w \text{ at } x = x_0 \text{ and } x = x_L \qquad (2.9a)$$

$$\frac{\partial h}{\partial z} = 0 \qquad \text{for } x_0 \le x \le x_L \text{ at } z = -4 \text{ km} \qquad (2.9b)$$

$$h = z_x^w \qquad \text{for } x_0 \le x \le x_L \text{ for } z = z_x^w \qquad (2.9c)$$

where x_0 equals 0.0 km, L is the horizontal length of the flow system (6.0 km), and z_x^w is the water table elevation at the specified x-coordinate.

In Figure 2.1, the free-surface is that portion of the water table that lies below the bedrock surface. Equation (2.9c) reflects the fact that freshwater head equals the water table elevation everywhere at the upper boundary of the saturated region of flow (fluid pressure is atmospheric at the water table). On the free-surface segment an

additional constraint is required to limit the infiltration available for recharge to the bedrock flow system. Fluid flux q_{n_i}, directed along the unit normal n_i to the free-surface, is driven by potential gradients and thermal buoyancy where;

$$q_{n_i} = -k_{ij}\frac{\rho_o g}{\mu}\left[\frac{\partial h}{\partial x_j} + \rho_r\frac{\partial z}{\partial x_j}\right]n_i = (I_z\cos\theta)n_i \qquad (2.10)$$

In keeping with the assumption of only vertical flow of fluid through the unsaturated zone, the available infiltration rate I_z is applied directly on the free-surface by computing the flux of fluid normal to a free-surface that slopes at an angle θ from horizontal. This boundary condition differs from that used by Neuman and Witherspoon (1970) in two respects. First, fluid flux and freshwater head conditions are specified on the free-surface segment while only freshwater head is specified on the seepage face (Figure 2.1). This approach allows recharge to occur on the seepage face between the hinge point (HP) and the point of detachment (POD). Below the HP, only discharge occurs. Second, a buoyancy term stated in terms of the relative buoyancy ρ_r is included inside the square brackets of equation (2.10) because thermal effects are incorporated in the formulation. Appendix II contains a discussion of the conditions that promote separation of the POD and HP and outlines use of a hodograph to demonstrate the theoretical basis for such a separation.

The steady state balance of thermal energy in a variably-saturated porous medium with no internal heat sources or sinks is described by:

$$\frac{\partial}{\partial x}[\lambda^e_{xx}\frac{\partial T}{\partial x} + \lambda^e_{xz}\frac{\partial T}{\partial z}] + \frac{\partial}{\partial z}[\lambda^e_{zx}\frac{\partial T}{\partial x} + \lambda^e_{zz}\frac{\partial T}{\partial z}]$$

$$- \rho_f C_f (q_x\frac{\partial T}{\partial x} + q_z\frac{\partial T}{\partial z}) = 0 \qquad (2.11)$$

where

T = temperature

C_f = specific heat capacity of fluid

λ^e_{ij} = thermal conductivity tensor for solid-fluid-vapor composite

The last term on the left side of equation (2.11) describes the advective transfer of heat by fluid flow both above and below the water table. In developing equation (2.11), thermal equilibrium is assumed to exist between fluid, solid and vapor.

Modeling heat transfer in the unsaturated zone ensures a water table temperature and thermal regime consistent with temperature conditions specified at the bedrock surface. By adopting a free-surface method, the rate of vertical fluid flow in the unsaturated zone is implicitly defined to be the available infiltration rate. In solving the equations of energy transport, one-dimensional advective heat transfer above the water table is modeled by setting the horizontal fluid flux q_x to zero and the vertical fluid flux q_z to the

available infiltration rate I_z in equation (2.11).

Heat conduction and thermal dispersion by fluid flow in the solid-liquid-vapor composite is represented by the first two terms of equation (2.11) using a thermal conductivity tensor defined by:

$$\lambda^e_{ij} = SnD_{ij} + (1 - S)n\lambda^v + (1 - n)\lambda^s_{ij} \qquad (2.12)$$

where

n = porosity of the porous matrix

λ^v = thermal conductivity of vapor

D_{ij} = conduction-dispersion tensor for fluid

λ^s_{ij} = thermal conductivity tensor for solid

S = degree of saturation

$S = 1$ below water table

$0 \leq S < 1$ above water table

In this formulation, the degree of saturation is specified only to calculate the thermal conductivity of the solid-fluid-vapor composite found above the water table. Saturation may vary from less than 0.2 to 1.0 within the unsaturated zone and reflects the relative proportion of vapor and fluid within the pore space. Because the thermal conductivity of air (vapor) is about 5 percent that of water, higher levels of saturation S contribute to greater thermal conductivity. Rocks most commonly found in mountainous terrain are likely to have porosity values less than about 15 percent. Therefore, the degree of saturation

has little impact on values calculated for thermal conductivity of the solid-vapor-fluid composite. In the absence of information regarding the variation of saturation in mountainous terrain, the pore space is assumed to be filled only with vapor (S = 0). Although a minimum degree of saturation is required to permit fluid flow in the unsaturated zone, this assumption provides an upper limit for the influence of saturation on mountain flow systems by contributing to a minimum estimate of thermal conductivity above the water table. Note that the thermal conductivity for a composite porous medium is defined using the arithmetic mean to account for the thermal conductivity of each material. This approach is commonly adopted in the hydrogeology literature (Sorey, 1978; Smith and Chapman, 1983) and differs from approaches found in the heat flow literature that reflect different views regarding the influence of porosity on thermal conductivity (Walsh and Decker, 1966; Scharli and Rybach, 1984). Simulation results presented in subsequent sections illustrate the influence of different values of thermal conductivity on advective heat transfer. These results suggest that differences between thermal conductivity values calculated would have little impact on groundwater flow systems and advective disturbance of mountain thermal regimes.

Bear (1972) uses a fluid conduction-dispersion tensor D_{ij} to account for heat conduction in the fluid and thermal dispersion by mechanical mixing. The nature of thermal

dispersion in a porous medium is described by Sauty et al. (1982). Bear (1979) shows that the dispersion terms can be expanded for an isotropic porous medium as follows:

$$nD_{xx} = \rho_f C_f (a_l q_x^2/\bar{q} + a_t q_z^2/\bar{q}) + n\lambda^f \quad (2.13a)$$

$$nD_{zz} = \rho_f C_f (a_t q_x^2/\bar{q} + a_l q_z^2/\bar{q}) + n\lambda^f \quad (2.13b)$$

$$nD_{xz} = nD_{zx} = \rho_f C_f (a_l \; a_t) q_x q_z/\bar{q} \quad (2.13c)$$

Here, a_l and a_t are longitudinal and transverse dispersivities, λ^f is the thermal conductivity of the fluid and $\bar{q}$ is the magnitude of the fluid flux.

The analagous energy balance equation for a fully saturated fracture zone is written using one-dimensional local coordinates as:

$$\frac{\partial}{\partial s}[n_f D_s + (1 - n_f)\lambda^s]\frac{\partial T}{\partial s} - \rho_f C_f q_s \frac{\partial T}{\partial s} = 0 \quad (2.14)$$

where

$$n_f D_s = \rho_f C_f (a_l q_s + n_f \lambda^f) \quad (2.15)$$

In equations (2.14) and (2.15), n_f is the porosity of the fracture where $0 < n_f < 1$ for fracture zones filled with porous material and n_f equals 1 for open fractures. Where n_f is less than 1, an isotropic thermal conductivity λ^s is

assumed for the fracture filling.

Boundary conditions for the heat transfer problem are:

$$\frac{\partial T}{\partial x} = 0 \qquad \begin{array}{l}\text{for } -4 \text{ km} \le z \le z_x^s \\ \text{at } x = x_0 \text{ and } x = x_L\end{array} \tag{2.16a}$$

$$\lambda_{zz}^e \frac{\partial T}{\partial z} = H_b \qquad \begin{array}{l}\text{for } x_0 \le x \le x_L \\ \text{at } z = -4 \text{ km}\end{array} \tag{2.16b}$$

$$T = T_r + G_l z_x^s \qquad \begin{array}{l}\text{for } x_0 \le x \le x_L \\ \text{at } z = z_x^s\end{array} \tag{2.16c}$$

where H_b is the conductive basal heat flow, T_r is a reference surface temperature specified at the valley floor, G_l is a thermal lapse rate applied at the bedrock surface and z_x^s is the surface elevation at the specified x coordinate position. Thermal springs are modeled where fracture zones outcrop at the bedrock surface by assuming that the heat flux from the fracture zone is equal to the advective flux of heat along the fracture zone. With only advective flux presumed to occur at the fracture outcrop, a specified temperature is not required and the bedrock temperature is dictated by the temperature of the fluid discharging from the fracture zone (a third-type boundary condition).

The fluid is assumed to be pure liquid water with density and viscosity a function only of temperature and

pressure. Water properties are evaluated using the relationships of Keenan *et al.* (1978) for density and of Watson *et al.* (1981) for viscosity. Specific heat capacity and thermal conductivity of water is assumed constant, as is the thermal conductivity of vapor in the unsaturated zone. Porosity, permeability and thermal conductivity vary in space but are to be unaffected by changes in temperature and pressure.

2.4 NUMERICAL METHOD

The Galerkin finite element method is used to solve the coupled equations of steady fluid flow and heat transfer. Two-dimensional vertical sections of porous media with planar or radial symmetry are represented by linear triangular elements. Thin, high-permeability fracture zones are included by embedding one-dimensional line elements in the field of triangular elements using the method described by Baca *et al.* (1984).

2.4.1 Free-surface Models

Free-surface methods have been developed to solve unconfined groundwater flow problems in which the position of the water table is initially unknown. Most free-surface methods involve successive estimation and correction of water table positions in an iterative procedure (for example; Neuman and Witherspoon, 1970). The majority of

free-surface codes have been applied to relatively small-scale problems of isothermal flow through porous media in systems with low topographic relief. Although Jamieson and Freeze (1983) applied the steady FREESURF model of Neuman and Witherspoon (1970) to the rugged topography of Meager Mountain, their solutions suggest that the seepage face is poorly represented. Non-isothermal free-surface models are described by Horne and O'Sullivan (1978) and Bodvarsson and Pruess (1983). These authors applied their models to regions of flat topography near producing geothermal fields.

An important difference between the numerical method used in this study and other methods lies in the approach used to solve the free-surface problem in terrain with high topographic relief. Conventional techniques assume that groundwater recharge occurs only above the point of detachment (POD), that is implicitly assumed to coincide with the hinge point (HP). In developing this modeling approach, it was found that the POD need not coincide with the HP in steep terrain with rocks of relatively low permeability (Appendix II). Therefore, recharge is allowed to occur downslope of the POD on the seepage face (Figure 2.1). Although this approach to viewing the nature of seepage faces has been revealed through study of mountainous terrain, it is equally applicable when examining systems in low-relief terrain. Failure to adopt this approach when studying groundwater flow in high-reief terrain may produce

solutions with unrealistic water table configurations.

2.4.2 Solution Procedure

The coupled equations of fluid flow and heat transfer are solved using an iterative procedure. The freshwater head and temperature distributions are calculated using the following steps:

1. Individual finite element meshes are constructed for the fluid flow and thermal problems.

2. Mesh accuracy is tested and meshes are reconstructed as necessary.

3. A temperature field is computed for heat conduction alone to obtain initial values for the temperature-dependent properties of water.

4. Iterations are performed to solve for freshwater head, estimate a new water table configuration, deform the mesh used in solving for freshwater head, reconstruct the mesh for the thermal problem, and solve for an updated temperature field.

5. Iterations terminate when successive water table elevations differ by no more than a specified tolerance. The number of iterations required typically ranges from 7 to 15.

6. Flux of fluid mass and thermal energy across boundaries

of the domain are calculated to evaluate mass and energy balances.

Mesh construction

Finite element meshes that can deform in a vertical direction are constructed for the fluid flow and thermal problems using an internal mesh generator. The fluid flow mesh is generated only within the saturated region of flow. The upper boundary of the initial mesh is defined using a reasonable guess of the water table configuration. In subsequent iterations, the current estimate of the position of the water table is used. An example of a mesh used in the solution for freshwater head, obtained at the final water table configuration, is shown in Figure 2.2a. Throughout the solution procedure, the structure of the mesh is unchanged below the elevation of the valley floor. Although the upper region of the mesh deforms to conform to successive estimates of the water table configuration, the number of nodes (1137) and elements (2139) remains unchanged during the iterative procedure.

Coupling between heat transfer and fluid flow is facilitated by ensuring a one-to-one correspondence between nodes located below the water table in each mesh. Heat transfer above the water table is modeled by extending the mesh used in solving the thermal problem to the bedrock surface (Figure 2.2b). Because the mesh for the fluid flow problem does not extend above the water table, fluid flow in

the unsaturated zone is implicitly defined by the available infiltration rate applied at the bedrock surface. Although the boundaries of the thermal problem remain fixed, the thermal mesh must be deformed internally (or reconstructed) to match changes in the fluid mesh.

A simple deformation of the mesh for the thermal problem is unable to account for lateral pinching out of the unsaturated zone as the length of the seepage face increases and the POD moves upslope on the bedrock surface during the iterative procedure. Therefore, the thermal mesh must be reconstructed in its entirety at each iteration to accomodate upslope or downslope movement of the POD. Each time the mesh is reconstructed, the number of nodes and elements may change depending upon the degree of POD movement. A final thermal mesh, that corresponds to the fluid mesh of Figure 2.2a, is shown in Figure 2.2b and contains 1230 nodes and 2201 elements. Because the numerical formulation does not include a method for maintaining the position of geologic structure within deforming regions of the mesh, fracture zones and heterogeneities must be restricted to non-deforming regions of the mesh.

The accuracy of each initial mesh is evaluated by solving the isothermal fluid flow problem and computing a total balance of fluid mass crossing all system boundaries and a fluid mass balance across the top surface. Because vertical grid lines in the deforming mesh are rarely

orthogonal to the sloping top boundary, computing fluid flux normal to the surface using freshwater heads can be inaccurate if the mesh is too coarse.

Flux inaccuracies are minimized in a two-step process. First, the free-surface method is used in an isothermal mode to solve for freshwater head and to obtain the water table configuration. Fluid fluxes are calculated at each boundary using the freshwater head solution. Second, the problem is reformulated using stream functions, with the previously-defined water table configuration forming the upper boundary of flow. This stream function solution provides an alternative method for calculating fluid fluxes normal to the water table.

Large differences between boundary fluxes obtained using the two solution methods often indicate regions where the water table configuration may be poorly estimated and the finite element mesh must be refined. Acceptable grids are defined when mass flux balances for flow across the water table differ by less than 1 percent and total mass balances differ by less than 5 percent. In addition to obtaining a good match in mass flux balance, it is also important to ensure that patterns of fluid flux on the upper boundary are the same for the two different formulations. Therefore, an acceptable grid must also provide hinge point positions that match for each solution method. Contour plots of the isothermal stream function solutions are particularly

useful for visualizing patterns of groundwater flow and for providing insight into the nature of mountain flow systems.

Iterative procedure

A coupled solution is obtained by solving equations (2.7) and (2.11) in an iterative procedure controlled by the free-surface method. At the upper boundary of the fluid flow problem a mixed boundary condition is defined. An available infiltration rate is applied where the water table lies below the bedrock surface (that is, on the free-surface) and freshwater head is specified where the water table coincides with the bedrock surface. Prior to initiating the iterations, equation (2.11) is solved for the conductive case to obtain the initial temperature field. These initial temperatures are used to compute fluid properties required in the first free-surface iteration. The numerical solution proceeds by updating the fluid properties using the latest estimate of the temperature field, solving equation (2.7) for freshwater head, obtaining a new estimate of the water table configuration to calculate specific discharge, and updating the temperature field by solving equation (2.11).

The solution begins by solving equation (2.7) for freshwater head and extrapolating a new water table position using the method described by Neuman and Witherspoon (1970). The finite element mesh is then deformed to conform to the shape of the new upper boundary. At each iteration, the POD is moved along the top surface to maintain a balance between

recharge and discharge. As the position of the POD changes, the length of the free-surface changes and the region where the available infiltration rate is applied varies.

In this modified free-surface method, it is assumed that the point of detachment (POD) marks the uppermost point where freshwater heads are known to equal the elevation of the bedrock surface, rather than the uppermost point of groundwater discharge. Although recharge rates are not initially known for the region between the POD and the hinge point (HP), they can be computed from the freshwater head solution. After each iteration, recharge rates computed using freshwater heads in the vicinity of the water table are compared to available infiltration rates. If recharge exceeds available infiltration near the POD, additional iterations are performed to refine further the water table configuration. This approach differs from that of Neuman and Witherspoon (1970) in two respects. First, fluid fluxes calculated at the seepage face are not explicitly used in solving equation (2.7). Rather, freshwater head is specified where the water table coincides with the bedrock surface and fluid flux is specified only on the free-surface. This minimizes the dependence of the solution on calculated fluid fluxes and allows the system of equations to be solved only once for each iteration, rather than the two-step process used by Neuman and Witherspoon (1970). Second, because only vertical mesh deformation is allowed, near-vertical topographic slopes are poorly represented in this modified

formulation.

In developing this approach, it is assumed that available infiltration is controlled by processes acting at the bedrock surface (evapotranspiration, subsurface stormflow, surface runoff) rather than by the position of the water table or by processes acting in the unsaturated zone. Therefore, when varying parameters such as permeability in a numerical sensitivity analysis, the available infiltration rate is assumed to be unaffected by varying depth to water table. Where the flow system accepts the entire available infiltration, the water table will be predicted to lie below the bedrock surface and recharge to the saturated region of flow is exactly equal to the available infiltration rate. Where only a portion of the available infiltration rate is accepted, the predicted water table will coincide with the bedrock surface and recharge to the flow system will be less than the available infiltration rate.

Solutions to the thermal transport equation (equation 2.11) may be poorly approximated by conventional finite element techniques when advective heat transfer dominates conduction. Such conditions are defined on the basis of a grid Peclet number that describes, on a local scale, the ratio of heat transfer by advection to that by conduction:

$$Pe = \frac{C_f \rho_f \bar{q} L_c}{\lambda^s} \tag{2.17}$$

where L_c is a characteristic length for an individual element. Patankar (1980) and Huyakorn and Pinder (1983) report that reliable solutions to both one-dimensional and two-dimensional transport problems are possible when $Pe \leq 2$. Although adequate mesh discretization can ensure reliable solutions, a large number of nodes may be required. In some cases however, upstream weighting procedures may reduce the number of nodes that are required.

An acceptable triangular element mesh is constructed by ensuring that the grid Peclet numbers are less than 2 for each element. In representing fracture zones as line elements within the triangular mesh, the fracture permeability must exceed that of the adjacent rock mass by at least four orders of magnitude (Baca *et al.*, 1984). Such large permeability contrasts imply that large fluid flux contrasts are possible. In such cases, solutions with triangular element *Pe*'s less than 2 may also have line element *Pe*'s much greater than 2. This problem is handled by defining an exponential basis function, the form of which depends upon *Pe* at the previous iteration, for incorporation in the finite element equations and for calculating average fluid properties within each line element. The method adopted is similar to that described for finite difference grids by Spalding (1972), Raithby and Torrance (1974) and

Patankar (1980). Patankar (1980) states that this approach provides good comparisons to one-dimensional analytical solutions for any value of Pe and any number of grid points.

The iterative procedure is terminated when water table elevations are resolved within a tolerance of 1 m and calculated recharge is less than available infiltration near the POD. In flow systems with topographic relief of 2 km, this tolerance of 1 m is 0.05 percent of the maximum possible water table relief. Once the solution is terminated, a final check is performed to ensure that nodal temperatures obtained at final and penultimate iterations differ by no more than 0.1 °C.

2.5 SUMMARY OF ASSUMPTIONS

In developing the numerical method described in the previous section, a number of assumptions are invoked. Those of deemed to be of greatest importance are summarized below:

1. Two-dimensional coupled fluid flow and heat transfer in rigid vertical sections with planar or axisymmetric symmetry.

2. Steady fluid flow and heat transfer. Diurnal and seasonal transients are neglected and a "dynamic" steady state is assumed. The impact of long-term climate change or ongoing igneous activity are not considered.

3. An equivalent porous medium is assumed except where major through-going fracture zones are represented as discrete entities with permeability at least 10^4 times that of the surrounding rock mass. Permeability and thermal conductivity may be heterogeneous and anisotropic.

4. Thermal equilibrium between fluid, solid and vapor.

5. Vertical boundaries for fluid flow and heat transfer are symmetry boundaries (impermeable and insulated).

6. The basal boundary is horizontal and impermeable with a conductive heat flux applied along the boundary.

7. The upper boundary of the domain is the bedrock surface where temperatures are specified using a thermal lapse rate.

8. One-dimensional vertical flow of fluid through the unsaturated zone causes one-dimensional advective heat transfer (combined with two-dimensional heat conduction) above the water table. Vertical fluid flux above the water table equals the available infiltration rate. Heat and moisture transport by vapor movement in the unsaturated zone are assumed negligible.

9. Fluid density and viscosity vary as a function of temperature and pressure while thermal conductivity and

specific heat capacity of the fluid are assumed constant.

2.6 IMPLEMENTATION OF THE MODEL

The numerical model described in the preceding section is used in Chapter 3 to examine the factors controlling groundwater flow through a mountain massif. To demonstrate the basic form of the results, an example is presented here that characterizes the thermal regime in mountainous terrain. Simulations are performed by assigning a set of fluid flow and thermal parameters (Table 2.1) within a geometry similar to that of Figure 2.1. The importance of surface topography is examined by considering two extremes in slope profile; one convex and one concave (Figure 2.3). Convex profiles are typical of glaciated crystalline terrain while concave profiles are often found in folded mountain belts and at volcanic cones.

A basal zone of low permeability occupies the lower 2 km of the system to provide a region of conduction-dominated heat transfer. The remainder of the system is occupied by a higher permeability unit where advective heat transfer may dominate. This configuration allows advective thermal disturbances in the upper unit to propagate into the basal conductive regime ensuring a reasonable transition between advection-dominated and conduction-dominated thermal regimes. This region is sufficiently thick that the majority of simulation results show isotherms near the basal boundary

to be sub-parallel to the boundary. As a consequence, the vertical conductive heat flux applied at the basal boundary is transferred in a consistent manner to the thermal regime. Both upper and lower zones have homogeneous and isotropic permeability (k_u, k_b) and uniform porosity (n_u, n_b). Rock thermal conductivity (λ^s) is uniform throughout the system, however, varying porosity and saturation produce contrasts in thermal conductivity for the solid-fluid composite (λ^e). Because we consider the steady state problem, porosity only has an indirect influence on the flow system through its impact on thermal conductivity of the solid-fluid composite. Porosity can be expected to play an important role in the transient flow of groundwater in mountainous terrain, especially in fractured crystalline rock. A uniform heat flow (H_b) is applied at the base of the flow system and surface temperature conditions are defined in terms of a reference surface temperature (T_r) and a thermal lapse rate (G_l). Longitudinal and transverse thermal dispersivities (a_l, a_t) are uniform throughout the system and held constant for all simulations.

Temperature fields, reflecting the interaction between advective and conductive heat transfer, are influenced by both fluid flow and thermal parameters. Figure 2.3 shows temperature fields obtained using the values of thermal parameters specified in Table 2.1 and values of I_z required to maintain the same water table configurations within each system as k_u varies from 10^{-18} to 10^{-15} m^2 (Table 2.2). By

maintaining the same water table position, the distribution of thermal conductivity is unchanged and temperature fields shown in Figure 2.3 differ only in the way that advective heat transfer, as influenced by fluid flow parameters alone, affects the thermal regime.

Pathlines represent the track of a particle entering the flow system at a specified point on the bedrock surface. Pathline spacing is inversely proportional to the flux of fluid (specific discharge) through flowtubes bounded by each pair of pathlines. Maintaining the same water table position produces patterns of fluid flow that are virtually identical for a given slope profile, despite a wide variation in the temperature fields. Despite their obvious similiarity, pathlines should not be confused with the streamlines generated from contour plots of a suitably defined stream function or velocity potential. These approaches differ because fluid flow through each streamtube (bounded by each pair of streamlines) is fixed throughout the domain while fluid flow through flowtubes defined on the basis of pathlines may differ from flowtube to flowtube. Flowtubes carry the same fluid flow only where they intersect the uniform fluid flux boundary (the free-surface) with equal spacing.

Water table configurations are maintained by increasing I_z by the same increment that k_u is increased. Maintaining the water table position as permeability is increased

implies that increasingly humid climates support the increased infiltration rates. The relationship between infiltration rate, permeability and water table elevation is examined in detail in Chapter 3.

Figures 2.3a to 2.3c show the transition from conduction-dominated to advection-dominated thermal regimes as a function of increasing permeability. Upper zone permeabilities (k_u) less than 10^{-18} m^2 produce a purely conductive thermal regime with isotherms sub-parallel to the surface topography (Runs C1 and C3 in Figure 2.3). An increase of two orders of magnitude in k_u to 10^{-16} m^2 produces a weak advective disturbance as evidenced by the warping of isotherms (Runs C2 and C4 in Figure 2.3). An additional one order of magnitude increase in k_u, to 10^{-15} m^2, creates a strongly disturbed thermal regime (Runs B2 and B7 in Figure 2.3). Smith and Chapman (1983) found that groundwater flux is sufficiently large to cause a transition from conduction-dominated heat transfer to a weakly disturbed thermal regime when permeability is about 10^{-17} m^2 in low-relief (1 km over 40 km) sedimentary basins. In regions of high-relief mountainous topography, fluid flux is sufficiently enhanced by the greater hydraulic gradients to cause this transition to occur at a lower permeability of about 10^{-18} m^2.

The maximum temperature attained along the base of each flow system (T_{max}) is tabulated in Table 2.2 for each run

shown in Figure 2.3. As k_u increases, T_{max} decreases from about 130 °C to about 85 °C. Higher permeabilities enhance groundwater flow, cool the subsurface and reduce conductive thermal gradients in regions of strong downward fluid flow. Reduced thermal gradients reflect the ability of groundwater to absorb and redistribute heat that would otherwise cause increased rock temperatures. The temperature fields shown in Figure 2.3 illustrate the range of thermal conditions that are encountered in the sensitivity analyses carried out in Chapter 3. A more detailed examination of the nature of thermal regimes in mountainous terrain is presented in Chapter 4.

2.7 SUMMARY

1. Groundwater flow systems in mountainous terrain differ from those in low-relief terrain in two key respects: (1) for a given set of hydrogeologic conditions, a greater range in water table elevation and form is possible; (2) high-relief terrain enhances groundwater circulation to depths where significant heating can occur, implying that thermal effects influence the patterns and rates of groundwater flow.

2. A conceptual model has been outlined to describe groundwater flow systems and thermal regimes in mountainous terrain. The problem is viewed as an overlay of two boundary value problems, one for fluid flow and one for heat

transfer. The uppermost boundary of the domain is the bedrock surface where temperatures are assumed to be a few degrees warmer than mean annual air temperature. Where the water table coincides with the bedrock surface, freshwater head equals the bedrock elevation. Where the water table lies below the bedrock surface, a uniform available infiltration rate is applied that represents one-dimensional fluid flow through the to the water table by one-dimensional flow through the unsaturated zone. Heat supplied by a regional heat flux is transferred through the system by advection and conduction in both saturated and unsaturated regions of flow. Fluid flow and heat transfer through a thin cover of discontinuous surficial deposits on upland areas of mountain slopes is not included in the model. Fluid moving within these deposits is lumped with overland flow as a runoff term. The remaining fluid available for recharge is termed an available infiltration rate which, in the absence of detailed field data, is best thought of as a percentage of the mean annual precipitation rate.

3. Traditional free-surface approaches incorrectly assume that recharge cannot occur downslope of the point where the water table meets the bedrock surface (commonly defined as the exit point marking the upper limit of the seepage face). In developing the approach used in this study, it was necessary to identify two separate points on the upper boundary; the point where the water table meets the bedrock surface (point of detachment or POD) and the point that

marks the transition between recharge and discharge (hinge point or HP). Between these points the water table coincides with the bedrock surface. In this region, the boundary condition is specified by setting hydraulic head equal to the elevation of the upper boundary and allowing recharge to occur at a rate defined by the nature of the groundwater flow system. In steep terrain, with rocks of low permeability, recharge can occur downslope of the POD in a region that might normally be considered part of the seepage face. In regions of reduced topographic relief, the separation between HP and POD becomes smaller and these points merge at the more commonly defined exit point.

4. The fluid and thermal regimes are modeled using a Galerkin finite element technique in conjunction with a free-surface approach to estimate the position of the water table. Two finite element grids are required in solving this problem. The mesh for fluid flow is generated only within the saturated zone. The mesh for heat transfer extends from the basal boundary to the bedrock surface, incorporating both saturated and unsaturated regions of flow. Coupling between heat transfer and fluid flow is facilitated by ensuring a one-to-one correspondence between nodes located below the water table.

5. Inaccuracies inherent in calculating boundary fluxes while solving the free-surface problem are minimized in a two-step procedure. The isothermal problem is first solved

for freshwater head and to obtain the water table configuration. The problem is then reformulated using stream functions. Large differences between boundary fluxes computed using the two solution methods often indicate regions where the water table configuration is poorly represented and the grid needs refinement. A further check on grid accuracy is supplied by establishing that matching hinge point positions are computed using each solution method.

6. The numerical method developed in this chapter provides the means to examine the factors that control groundwater flow and heat transfer in mountainous terrain; geology, surface topography, climate and regional heat flow. Simulation results indicate that each factor influences both advective heat transfer and the position of the water table. Adopting the free-surface approach is advantageous in performing sensitivity analyses because recharge to the flow system is controlled as an input variable rather than implicitly calculated in the solution procedure.

REFERENCES

Baca, R.G., R.C. Arnett, and D.W. Langford, Modelling fluid flow in fractured-porous rock masses by finite element techniques, International Journal for Numerical Methods in Fluids, 4, 337-348, 1984.

Barry, R.G., Mountain weather and climate, Methuen, 1981.

Bear, J., Dynamics of fluids in porous media, American Elsevier, 1972.

Bear, J., Hydraulics of Groundwater, McGraw-Hill, 1979.

Birch, F., Flow of heat in the Front Range, Colorado, Bull. Geol. Soc. Amer., 61, 567-630, 1950.

Bodvarsson, G.S., and K. Pruess, Modeling studies of geothermal systems with a free water surface, Stanford Ninth Annual Workshop on Geothermal Resources Engineering, 1983.

Chapman, D.S., and L. Rybach, Heatflow anomalies and their interpretation, Jour. of Geodynamics, 4, 3-37, 1985.

Freeze, R.A., and J.A. Cherry, Groundwater, Prentice-Hall Inc., 1979.

Freeze, R.A., and P.A. Witherspoon, Theoretical analysis of regional groundwater flow: 2. Effect of water-table configuration and subsurface permeability variation, Water Resour. Res., 3, 623-634, 1967.

Frind, E.O., Simulations of long-term transient density-dependant transport in groundwater, Adv. Water Resourc., 5, 73-88, 1982.

Horne, R.N., and M.J. O'Sullivan, Numerical modeling of a desaturating geothermal reservoir, Numerical Heat Transfer, 1, 203-216, 1978.

Huyakorn, P.S., and G.F. Pinder, Computational methods in subsurface flow, Academic Press, 1983.

Jamieson, G.R., and R.A. Freeze, Determining hydraulic conductivity distributions in a mountainous area using mathematical modeling, Groundwater, 21(2), 168-177, 1983.

Keenan, J.H., F.G. Keyes, P.G. Hill, and J.G. Moore, Steam Tables, 162 pp., John Wiley, 1978.

Neuman, S.P., and P.A. Witherspoon, Finite element method of analyzing steady seepage with a free-surface, Water Resour. Res., 6(3), 889-897, 1970.

Patankar, S.V., Numerical heat transfer and fluid flow, McGraw Hill, 1980.

Raithby, G.D., and K.E. Torrance, Upstream weighting differencing schemes and their application to elliptic problems involving fluid flow, Comput. Fluids, 2, 191-206, 1974.

Ross, B., A conceptual model of deep unsaturated zones with negligible recharge, Water Resour. Res., 20(11), 1627-1629, 1984.

Sauty, J.P., A.C. Gringarten, H. Fabris, D. Thiery, A. Menjoz, and P.A. Landel, Sensible energy storage in aquifers, 2, Field experiments and comparisons with theoretical results, Water Resour. Res., 18(2), 245-252, 1982.

Scharli, U., and L. Rybach, On the thermal conductivity of low-porosity crystalline rocks, Tectonophysics, 103, 307-313, 1984.

Smith, L., and D.S. Chapman, On the thermal effects of groundwater flow 1. Regional scale systems, Jour. Geop. Res., 88(B1), 593-608, 1983.

Smith, M.W., Microclimatic influences on ground temperatures and permafrost distribution, Mackenzie Delta, Northwest Territories, Canadian Journal of Earth Science, 12, 1421-1438, 1975.

Sorey, M.L. Numerical modeling of liquid geothermal systems, U.S. Geol. Surv. Prof. Paper 1044-D, 1978.

Spalding, D.B., A novel finite difference formulation for differential equations involving both first and second derivatives Int. J. Numer. Methods Eng., 4, 551-559, 1972.

Verruijt, A., Theory of Groundwater Flow, Macmillan Press, 1970.

Walsh, J.B., and E.R., Decker, Effect of pressure and saturating fluid on the thermal conductivity of compact rock, Jour. Geoph. Res., 71, 3053-3061, 1966.

Watson, J.T.R, R.J. Basu, and J.V. Sengers, An improved representative equation for the dynamic viscosity of water substance, Jour. Phys. Chem. Ref. Data, 9(3), 1255-1279, 1981.

TABLE 2.1

TYPICAL SIMULATION PARAMETERS - CHAPTER 2

Fluid Flow Parameters

k_b	permeability of basal unit	1.0×10^{-22} m^2
k_u	permeability of upper unit	1.0×10^{-15} m^2
I_z	vertical infiltration rate	2.0×10^{-9} m/s

Thermal Parameters

H_b	basal heat flow	60.0 mW/m^2
G_l	thermal lapse rate	5 K/km
T_r	reference surface temperature	10 °C
n_b	porosity of basal unit	0.01
n_u	porosity of upper unit	0.10
λ^s	solid thermal conductivity	2.50 W/mK
λ^f	fluid thermal conductivity	0.58 W/mK
λ^v	vapor thermal conductivity	0.024 W/mK
C_f	specific heat capacity of water	4186.0 J/kgK
S	saturation above water table	0.0
a_l	longitudinal thermal dispersivity	100.0 m
a_t	transverse thermal dispersivity	10.0 m

TABLE 2.2

INFLUENCE OF PERMEABILITY k_u AND INFILTRATION I_z ON MAXIMUM TEMPERATURES IN FLOW SYSTEM T_{max}

RUN	PROFILE	k_u (m^2)	I_z (m/sec)	T_{max} (°C)
C1	X	10^{-18}	$2x10^{-12}$	138
C2	X	10^{-16}	$2x10^{-10}$	130
B2	X	10^{-15}	$2x10^{-9}$	81
C3	V	10^{-18}	$5x10^{-12}$	122
C4	V	10^{-16}	$5x10^{-10}$	117
B7	V	10^{-15}	$5x10^{-9}$	87

Notes:

1) Slope Profile; X = convex, V = concave
2) Rock thermal conductivity λ^S = 2.5 W/mK
3) Basal heat flow H_b = 60.0 mW/m^2

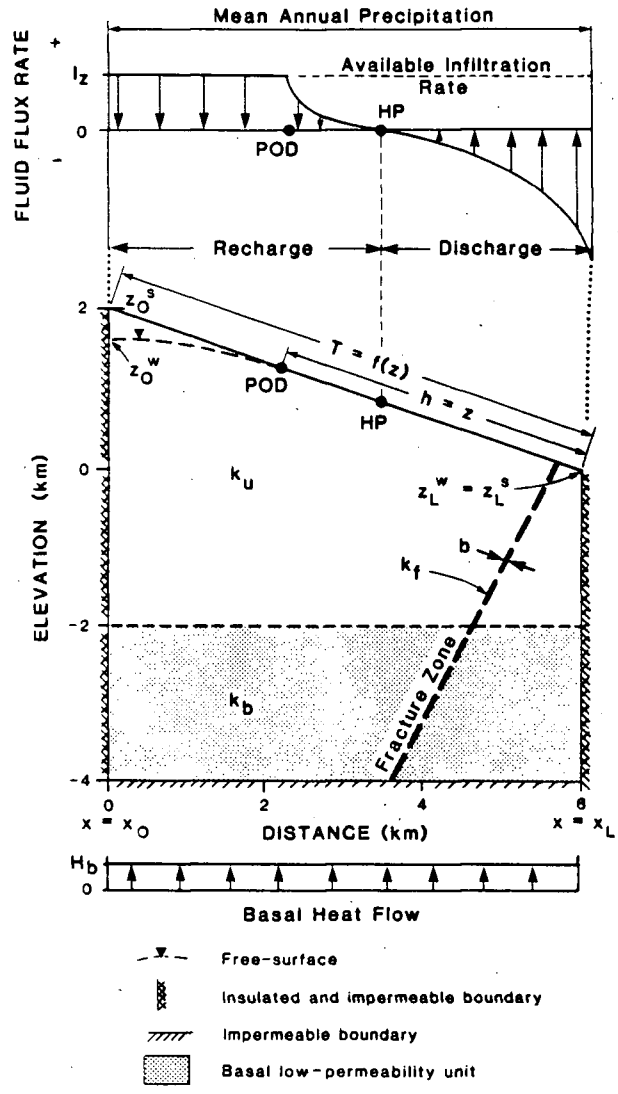

Figure 2.1. Conceptual model for groundwater flow in mountainous terrain.

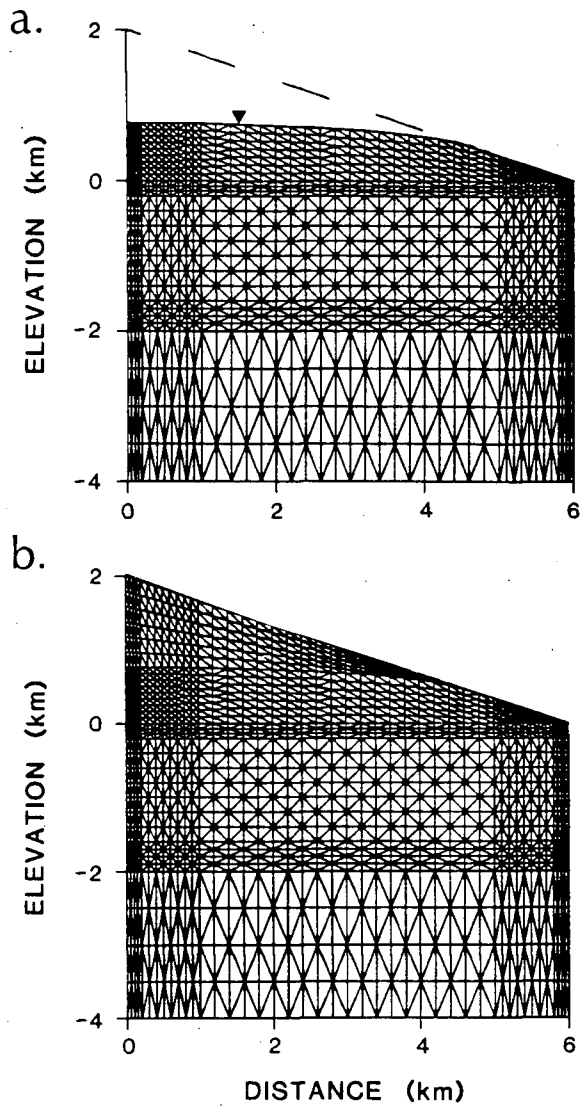

Figure 2.2. Typical finite element meshes;
a. fluid flow problem (1137 nodes, 2139 elements), and
b. heat transfer problem (1230 nodes, 2201 elements).

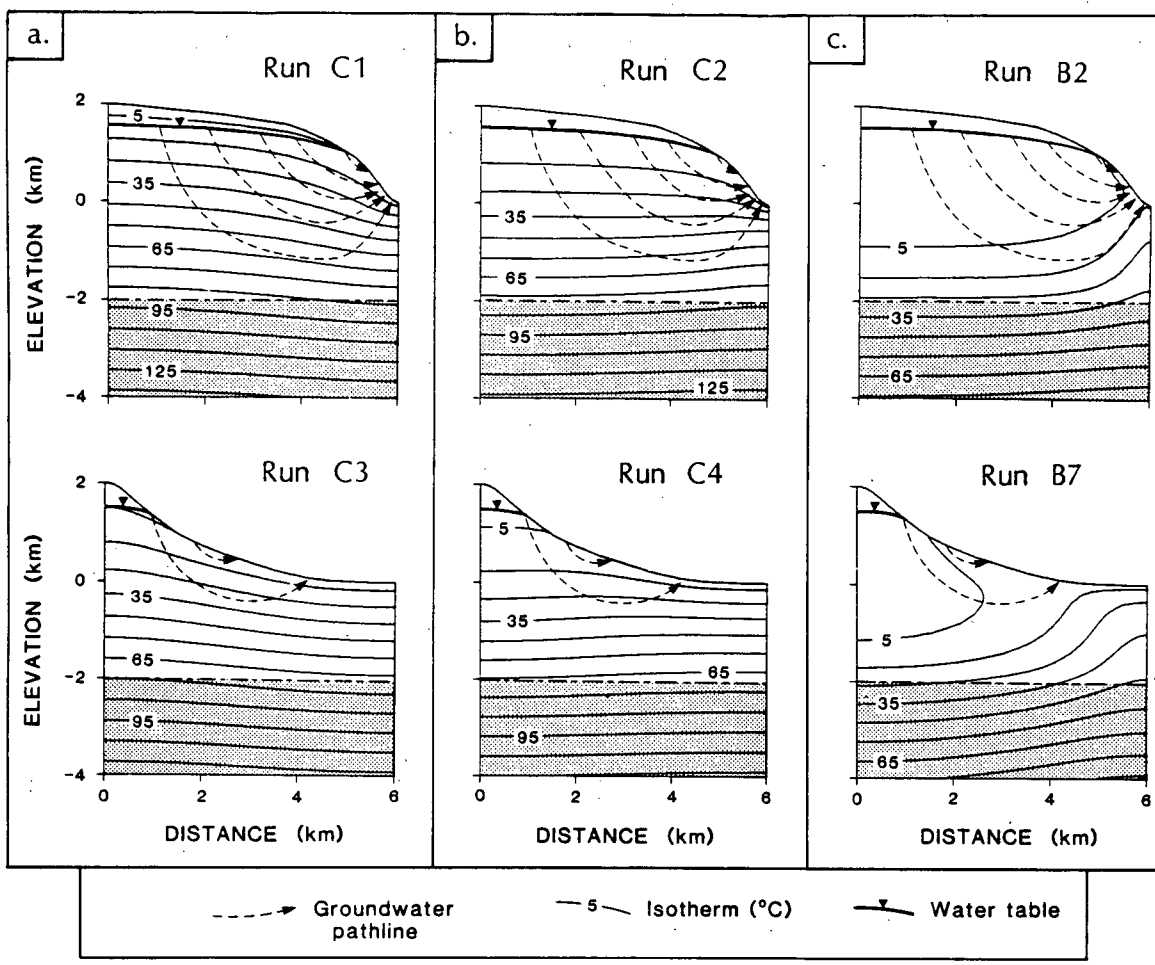

Figure 2.3. Temperature fields and groundwater flow patterns as a function of upper zone permeability k_u for fixed water table configurations in concave and convex slope profiles;

a. k_u = 10^{-18} m^2 (I_z = 2×10^{-12} m/sec for convex Run C1 and 5×10^{-12} m/sec for concave Run C3),

b. k_u = 10^{-16} m^2 (I_z = 2×10^{-10} m/sec for convex Run C2 and 5×10^{-10} m/sec for concave Run C4) and,

c. k_u = 10^{-15} m^2 (I_z = 2×10^{-9} m/sec for convex Run B2 and 5×10^{-9} m/sec for concave Run B7).

CHAPTER 3

GROUNDWATER FLOW SYSTEMS IN MOUNTAINOUS TERRAIN

3.1 INTRODUCTION

Conceptual and numerical models describing fluid flow and heat transfer in mountainous terrain are presented in Chapter 2. This approach differs in two respects from those used previously to simulate regional groundwater flow systems. First, a non-isothermal formulation provides the means to account for heating of groundwater deep within the mountain massif. Secondly, the free-surface approach avoids making *a priori* assumptions on the location of the water table. This approach is advantageous because, with sparse field data, it is most appropriate to estimate water table configurations within constraints imposed by infiltration rates, surface topography, rock permeabilty, and regional heat flux. Accounting for both conductive and advective heat transfer in the unsaturated zone allows the interaction of fluid flow and heat transfer to be examined, at a regional-scale, throughout both saturated and unsaturated regions of flow.

In this chapter, the factors controlling patterns and magnitudes of groundwater flow in mountainous terrain are examined in detail. Using the numerical method described in

Chapter 2, idealized mountain flow systems are modeled for a range of conditions representative of the Western Cordillera in North America. Factors to be considered are surface topography, geology, climate, and regional heat flow. Elements of surface topography include slope profile, relief and three-dimensional form. The implications of the three-dimensional topography of mountainous terrain are explored by modeling simple planar and axisymmetric mountain forms with the two-dimensional method. Two extremes in slope profile are examined; one convex and one concave. Convex profiles are typical of glaciated crystalline terrain while concave profiles can be found in folded mountain belts and at volcanic cones. The geologic environment controls spatial variability of permeability, porosity, and thermal conductivity. Climatic factors influence available infiltration, the presence and extent of alpine glaciers, and surface temperature conditions. Regional heat flow is a characteristic of the tectonic environment within which the mountain is located. Table 3.1 summarizes the simulations carried out to develop a quantitative understanding of the importance of each factor and provides a guide to the figures that illustrate each effect.

In this chapter we focus primarily on the hydrogeologic regime. Readers are referred to Figure 2.3 in Chapter 2 for examples of temperature distributions typical of the systems to be described in this chapter. The primary feature to recall from this diagram is the transition from a

conduction-dominated to an advectively-disturbed thermal regime. Higher permeabilities enhance groundwater flow which, in turn, cools the subsurface and reduces conductive thermal gradients in regions of downward flow. In the example presented, maximum temperatures were reduced by as much as 45 °C from those found in a low-permeability, conductive regime. The nature of mountain thermal regimes will be considered in greater detail in Chapter 4.

3.2 METHOD OF PRESENTATION

Before discussing the sensitivity analyses, the method of presenting the simulation results is outlined. A typical set of results is shown in Figure 3.1 for both convex and concave topographic profiles. A basal zone of low permeability occupies the lower 2 km of the domain to provide a region of conduction-dominated heat transfer. This region is sufficiently thick that the majority of simulation results show isotherms near the basal boundary to be sub-parallel to the boundary. As a consequence, the vertical conductive heat flux applied at the basal boundary is transferred in a consistent manner to the thermal regime. The remainder of the system is occupied by a higher permeability unit where advective heat transfer may dominate. In most simulations, both upper and lower zones have homogeneous and isotropic permeability (k_u, k_b) and uniform porosity (n_u, n_b). Although the thermal conductivity of the solid matrix (λ^s) is uniform throughout the system,

spatial variation in porosity and saturation produce contrasts in thermal conductivity of the solid-vapor-fluid composite (λ^e). Because we consider the steady state problem, porosity only has an indirect influence on the flow system through its impact on thermal conductivity. Porosity can be expected to play an important role in transient mountain flow systems, especially in fractured crystalline rock. A uniform heat flow (H_b) is applied at the base of the flow system and surface temperature conditions are defined in terms of a reference surface temperature (T_r) and a thermal lapse rate (G_l). Longitudinal and transverse thermal dispersivities (a_l, a_t) are uniform throughout the system and held constant for all simulations. Fluid and thermal properties held constant in the simulations are listed in Table 3.2.

Recharge-discharge profiles shown in Figure 3.1 depict the mass flux of fluid m_n in kg/m^{2}sec, normal to the water table, projected on a horizontal surface. In high-relief systems with variable water table slope, the areas under recharge and discharge portions of the profile do not provide a direct estimate of net recharge and discharge for the flow system. The total flow through each planar flow system (Q) is calculated within the numerical formulation by summing the recharge normal to a unit width of the upper boundary in units of kg/sec. Total flow (Q) for axisymmetric systems is calculated by summing the recharge to the upper circular boundary of the radial system, also with units of

kg/sec.

The vertical sections in Figure 3.1 illustrate water table configurations and patterns of groundwater flow. Pathlines represent the track of a particle entering the flow system at a specified point on the bedrock surface. Pathline spacing is inversely proportional to the flux of fluid (specific discharge) through flowtubes bounded by each pair of pathlines. Despite their obvious similiarity, pathlines should not be confused with the streamlines generated from contour plots of a suitably defined stream function or velocity potential. These approaches differ because flow of fluid through each streamtube (bounded by each pair of streamlines) is fixed throughout the domain while fluid flow through flowtubes defined on the basis of pathlines may differ from flowtube to flowtube. Flowtubes carry the same fluid flow only where they intersect the uniform fluid flux boundary (the free-surface) with equal spacing. Because a uniform available infiltration rate is applied in each case, the magnitude of I_z provides a convenient reference for comparing the variation of fluid flux. For example, pathline spacing in Figures 3.1a and 3.1b varies in response to the fact that fluid flux in the convex domain increases approximately fivefold from a value of 2×10^{-6} kg/sec at the free-surface to about 10^{-5} kg/sec (on average) at the discharge area. Fluid flux is more uniform in the concave domain (Figure 3.1b), decreasing from 2×10^{-6} kg/sec at the free-surface to about 1.6×10^{-6} kg/sec.

The relatively narrow range of fluid flux within each domain shown in Figure 3.1 suggests that the available infiltration rate can be viewed as a characteristic specific discharge for the domain under consideration, when the water table lies below the bedrock surface. As a consequence, characteristic transit times can be calculated for each flow system where $t_c = n_u/I_z L_p$. Here, L_p is the length of a specified pathline and n_u is the porosity of the upper permeable zone. Transit times for the lowermost pathlines shown in Figure 3.1 are about 8×10^5 years for domains with bulk permeability of 10^{-15} m^2.

Simulation results are quantified by defining the following parameters:

WT_{max} (m) maximum elevation of water table, usually located below the mountain summit.

ΔWT_{max} (m) absolute difference between the value of WT_{max} obtained in a previous simulation and that obtained in the simulation run of interest.

ΔQ (%) percentage change in total flow between a designated reference Q and that obtained in the run.

ΔWT_{max} and ΔQ provide a convenient measure of the sensitivity of mountain flow systems to differences in

permeability, infiltration rate, surface topography and thermal regime. For a specified set of thermal parameters, an infiltration ratio $I^* = I_z/K_o$ can be defined where K_o is a reference hydraulic conductivity:

$$K_o = \frac{k_u \rho_o g}{\mu_o} \tag{3.1}$$

with fluid density ρ_o and viscosity μ_o specified at the reference surface temperature T_r. A wide range in permeability and infiltration rates can be explored with a relatively small number of simulations by recognizing the applicability of the dimensionless infiltration ratio I^*.

Results are presented in Table 3.3 for sixteen simulation series designated A through P. Each series illustrates the influence of a specified controlling factor such as slope profile, infiltration rate or permeability. Data tabulated in Table 3.3 (convex Runs C1, C2, B2 and concave Runs C3, C4, B7) indicate that maintaining a constant I^* yields differences in water table elevations that do not exceed 20 m as k_u varies over three orders of magnitude, despite a significant variation in temperature fields (see Figure 2.3 in Chapter 2). Moreover, the patterns of fluid flow are essentially unchanged as k_u varies. This result reflects an approximate linear relationship between I_z and k_u for a given set of thermal parameters.

Results shown in Table 3.3 indicate that increasing permeability and infiltration by a specified increment

causes total flow Q to increase by the same increment (convex Runs C1, C2, B2 and concave Runs C3, C4, B7). This suggests that a dimensionless total flow Q^* can be defined in a manner similar to that used to define I^*; where I_z is normalized with respect to K_o (equation 3.1). Dimensionless total flow Q^* is defined as follows:

$$Q^* = \frac{Q}{L\rho_o K_o W} \tag{3.2}$$

where L is the length of the section and W is a unit width. Simulation results indicate that unique values of Q^* and I^* are found for each water table position within a specified system geometry. For example, a maximum water table elevation of about 1550 m is found in the convex domain when I^* equals 0.26 (Runs C1, C2 and B2 in Table 3) and Q^* equals 0.22 although both permeability and infiltration vary over three orders of magnitude in the simulation series. Although dimensionless total flow Q^* lacks an obvious physical meaning, it is a useful parameter for viewing the relative changes in total flow calculated in subsequent numerical simulations.

In developing dimensionless parameters to characterize the simulation results a dimensionless water table elevation was considered but not implemented. Such a parameter might be useful in assessing the influence of topographic relief. Examining the absolute magnitude of changes in water table elevation, however, yields greater insight into the influence of factors controlling groundwater flow in

mountainous terrain.

3.3 FACTORS CONTROLLING GROUNDWATER FLOW IN MOUNTAINS

3.3.1 Slope Profile

Examining simulation results obtained for simple topographic slope profiles provides insight into flow systems found in complex mountain topographies. Simulation results for a system with convex topographic profile (Run A1) and a concave profile (Run A2) are shown in Figure 3.1 and tabulated in Table 3.3. The recharge-discharge profiles of Figure 3.1 indicate the strong influence of slope profile on the pattern and magnitude of fluid flux across the bedrock surface. In convex topography, the recharge area is more extensive than the discharge area and discharge fluxes can greatly exceed recharge fluxes (Figure 3.1a). In the concave topography recharge and discharge areas are approximately equal and discharge fluxes are similar to recharge fluxes (Figure 3.1b).

A key factor in determining the influence of slope profile is the volume of rock within the mountain massif that acts to resist fluid flow. For example, convex profiles contain a greater volume of porous rock above the valley floor than concave profiles (Figure 3.1). Therefore greater mechanical energy, reflected by higher water table elevations, is required to drive groundwater flow through

convex slopes. The higher water table elevations found in the convex slope, in turn, contribute to a more extensive region of recharge. As a consequence, applying the same available infiltration rate in each case causes a total flow through the convex system twice that of the concave system (Table 3.3). Differences between water table elevations calculated for each slope profile highlight the advantage of using a free-surface approach to estimate water table configurations that are consistent with assumed available infiltration rates, thermo-hydrologic properties of the region and surface topography.

3.3.2 Infiltration Ratio

Available infiltration rate (I_z) and the permeability of the mountain massif (k_u) influence water table elevations and rates of fluid flow through the infiltration ratio (I^*). Prior to describing the influence of the infiltration ratio on flow systems, reasonable limits are defined for infiltration rates and permeability in mountainous terrain.

Mean annual precipitation is the basic determinant of available infiltration rates. Review of climate summaries (Bryson and Hare, 1974; Ruffner and Blair, 1975) indicates that precipitation rates at mountain summits of western North America are unlikely to exceed 6 m/year, except perhaps in southwest Alaska. In the low permeability terrain and humid climate of the Alaska Panhandle, recharge to mountain flow systems is unlikely to exceed approximately 10

percent of this summit precipitation rate. Therefore, it seems reasonable to assume an upper limit for available infiltration rates of about 0.6 m/yr (2.0×10^{-8} m/sec). In more arid climates, with terrain of higher permeability, infiltration rates are unlikely to exceed this upper limit although a greater percentage of the precipitation rate may be available for infiltration. Recall that, in developing this conceptual model (Chapter 2), a minimum infiltration rate of 10^{-12} m/sec is assumed. The reference I_z of 2×10^{-9} m/sec shown in Table 3.2 is selected to represent the maximum rate of infiltration that might be available in a climate transitional between semi-arid and humid. Values of I_z used in this study vary from 2×10^{-12} m/sec to 2×10^{-8} m/sec (Table 3.3) to provide a realistic range of infiltration rate.

Freeze and Cherry (1979) note that rock permeabilities can range from less than 10^{-20} m^2 to in excess of 10^{-9} m^2. The bulk permeability of mountainous terrain considered in this study is assumed to be less than 10^{-14} m^2. Freeze and Cherry (1979) and Neuzil (1986) suggest this is a reasonable upper limit for moderately fractured crystalline and argillaceous rocks.

Simulation results show that a sevenfold increase in the infiltration ratio I^*, from 0.13 to 0.92, causes an increase in water table elevation in excess of 1000 m (concave Runs A2, B5 through B8 and convex Runs A1, B1

through B4 in Table 3.3) as I_z increases from 1.0×10^{-9} to 7.0×10^{-9} m/s (0.032 to 0.224 m/yr). If this difference in I^* were to reflect only differences in mean annual precipitation, a sevenfold change in I_z indicates that a substantial variation in climate is required to effect a large change in water table elevation. A sevenfold increase in infiltration ratio could equally well correspond to an equivalent decrease in permeability k_u. This variation is only a small portion of the possible range of permeability or infiltration rates that might be encountered in mountainous terrain. Therefore, it is important to obtain reasonable estimates of each factor if reliable predictions of water table elevations are desired.

Water table configurations and recharge-discharge profiles are shown in Figure 3.2 for three infiltration rates that span the sevenfold range in I^* discussed in the previous paragraph (convex Runs A1, B1, B4 and concave Runs A2, B5 and B8 in Table 3.3). Pathlines are shown for two sets of paired runs (A1 and B1, A2 and B5) in Figures 3.2a and 3.2b with the dashed lines indicating the runs with lower infiltration rate (B1 and B5). These paired runs reflect a threefold difference in I^* from 0.13 to 0.40 that produces differences in water table elevations in excess of 500 m. Flow patterns within each profile can be compared by recognizing that individual pathlines drawn for each pair originate at the same point on the bedrock surface. Although a large difference in water table elevation is found for the

paired runs in each system, the overall patterns of flow are relatively unaffected. Note the assumed vertical flow above the water table contributes to the deeper pathlines in systems with lower water table elevations. If lateral fluid flow in the unsaturated zone were to be considered, the resulting pathlines might resemble those shown for the cases with higher water table elevation (Figure 3.2).

Recharge-discharge profiles shown in Figure 3.2 indicate that the pattern and magnitude of mass flux in both recharge and discharge areas is strongly influenced by varying the infiltration ratio. In each case shown in Figure 3.2, increasing I_z causes the HP (hinge point marking transition between groundwater recharge and discharge) to move upslope on the bedrock surface, a shorter free-surface segment and an increase in rates of groundwater discharge. Furthermore, the difference in the form of recharge-discharge profiles obtained for convex and concave cases provides further evidence for the way that the influence of slope profile on flow systems is amplified in mountainous terrain.

A plot of WT_{max} versus I^* (Figure 3.3a) demonstrates the variation in water table elevation as a function of available infiltration rate (or permeability) for both slope profiles. The solid circles (Curve 1) represent results obtained for the concave profile while the open circles (Curve 2) represent results obtained for the convex profile.

For a specified set of thermal parameters and system geometry, a threshold infiltration ratio can be defined that represents the maximum recharge rate accepted by the flow system. When the threshold ratio is applied, the water table is everywhere at the bedrock surface and the maximum flow through the system is attained. In Figure 3.3a, threshold infiltration ratios are the values of I^* required to raise the water table to its maximum possible elevation of 2000 m. The threshold I^* is about 1.0 for the concave topography and about 0.50 for the convex topography. If I^* is increased above the threshold, the flow system is unaffected as greater runoff must occur. Run B4, with I^* = 0.92, greatly exceeds the threshold rate for the convex profile while Run A1 with I^* = 0.40 is slighlty less than the threshold. Despite the large difference in applied infiltration rate (and hence in I^*) the water table configurations and recharge-discharge profiles found for Runs B4 and A1 are indistinguishable in Figure 3.2a because I^* for Run A1 approaches the threshold value. In the companion plot of WT_{max} versus dimensionless total flow Q^* (Figure 3.3b), maximum dimensionless flows of about 0.14 and 0.26 occur for concave and convex profiles when the threshold infiltration ratio is exceeded.

Figure 3.3a indicates that water table elevations vary as a function of I^* in a non-linear fashion. The overall slope of the I^* against WT_{max} plot differs for the concave (Curve 1) and convex (Curve 2) cases. The steeper slope of

the convex case indicates that water table elevations in convex topography are more sensitive to rock permeability or infiltration rate than water table elevations in concave topography. Note that, regardless of slope profile, large differences in water table elevation may correspond to relatively small variations in infiltration ratio. For example, a 100 m increase in water table elevation from 1600 to 1700 m corresponds to an increase of less than 20 percent in I^* for each slope profile (Figure 3a). This result suggests that measured water table elevations could aid in constraining estimates of infiltration rates and bulk permeability for the mountain massif. Unfortunately, as will be shown in a later section, water table configurations are strongly influenced by the thermal regime. Therefore, a knowledge of the thermal conditions is also required if hydraulic properties of mountain flow systems are to be constrained using measured water table elevations.

Total flow Q and dimensionless Q^* for each run are tabulated in Table 3.3 and Q^* is plotted versus WT_{max} in Figure 3.3b. In a concave slope profile with high water table elevations, the total flow through the flow system (represented by Q^*), is virtually independent of water table elevation and infiltration ratio. Therefore, modeling studies designed to obtain estimates of total flow through the bedrock flow system of concave slope profiles need not make accurate estimates of water table configurations if the water table is located high in the mountain massif. As water

table elevation decreases, total flow is increasingly sensitive to changes in WT_{max} and hence to I^*. A similar relationship exists for the convex profile, however, Q^* for high water elevations is more sensitive to the position of the water table in the mountain massif (Figure 3.3b).

3.3.3 Topographic Relief and Basin Depth

The influence of reduced topographic relief can be assessed by truncating the slope profiles described previously at an elevation of 1000 m (Figure 3.4). In this manner topographic relief is reduced by a factor of one-half, while the profile of the bedrock surface on the lower slope is maintained.

The results of two runs, one for each truncated profile (Runs 02 and 03), are shown in the plots of WT_{max} versus I^* and WT_{max} versus Q^* (Figures 3.3a and 3.3b). The square symbols represent the truncated concave case (Curve 3) and the truncated convex case (Curve 4). These curves indicate that lower relief causes an increase in water table elevation and a small decrease in total flow under conditions that differ only in topographic relief from those used to obtain Curves 1 and 2. Performing this numerical exercise under isothermal conditions would show that the response of the truncated topography replicates the response of the original slope profiles. The differences between Curves 1 and 3 and between Curves 2 and 4 shown in Figures 3.3a and 3.3b result from the advective transfer of heat in

the unsaturated zone. This contrast in results indicates the importance of accounting for advective heat transfer in thick unsaturated zones when attempting to predict water table elevations in mountainous flow systems.

Modifying the geometry of the lower slope has a significant impact on water table configurations and total flow rates. Curves with triangular symbols (labelled Curve 5 in Figures 3.3a and 3.3b) represent the influence of modifying the truncated concave profile to provide a fully concave profile from ridge to valley. The resulting slope profile is sketched in Figure 3.4b and simulation results for Run O3 are tabulated in Table 3.3. Results plotted for the modified concave topography (Curve 5 in Figures 3a and 3b) differ significantly from those found for the low-relief system with a flat upland area (Curve 3) because the length of the free-surface segment is reduced in the modified concave topography. As a consequence, total flow is significantly reduced in the low-relief fully concave case and water table elevations are less sensitive to changes in infiltration ratio. This result highlights the way that high-relief terrain amplifies the impact of factors controlling groundwater flow. In this case, the factors are permeability and available infiltration rate.

A decrease in basin depth is simulated by increasing the thickness of the basal low-permeability zone from 2 km to 3 km while maintaining the external geometry used in the

previous concave runs. The corresponding decrease in the thickness of the upper permeable zone reduces the total flow by 21 percent (Run P1, Table 3.3) from that of Run B7. Despite this significant reduction in Q, the water table elevation increases by only 94 m as basin depth is reduced by 1 km.

3.3.4 Topographic Symmetry

Axisymmetric Topography

Simple three-dimensional mountain forms amenable to two-dimensional characterization are axisymmetric conical features and linear ridges. Axisymmetric topography is representative of isolated mountain massifs elevated above a more uniform low-relief topography. The influence of topographic symmetry is examined by modeling a specified slope profile twice; assuming planar symmetry in the first case (Run I1 and I3) and radial symmetry in the second case (Run I2 and I4).

An isolated concave mountain located on a flat plain is shown in Figure 3.5 with flow patterns for planar Run I3 and axisymmetric Run I4. The axis of symmetry is located at the lefthand boundary beneath the ridgetop. Because the surface area available for discharge increases with increasing radial distance, rates and patterns of fluid flow (shown by differences in pathline patterns) within the radial system differ from those of the equivalent planar system. If

axisymmetric mountain topography is represented using planar symmetry, water table elevations are overestimated to a significant degree, vertical components of fluid flux are underestimated throughout the region of flow, and pathlines are displaced to shallower depths in the flow system (Figure 3.5). Although significant differences in recharge rates occur on the mountain flank, only minor differences in discharge rates occur over much of the flat plain. Similar results are obtained, but not shown, for a convex mountain adjacent to a flat plain (Runs I1 and I2 in Table 3.3).

Ridge and Valley Asymmetry

If a groundwater flow divide is assumed to correspond to the crest of an asymmetric ridge, errors in estimating the magnitude of groundwater flow to each valley can result. Results obtained for an asymmetric ridge (Run J1 shown in Figure 3.6) exhibit a divide displacement of 1.9 km. The corresponding flow pattern and recharge-discharge profile indicate that about one-third of the infiltration applied on the free-surface is applied to the right of the ridgecrest yet transmitted to the lefthand valley. This represents a significant redistribution of infiltration from the righthand to the lefthand watershed. Without using the free-surface approach, it would be difficult to predict, *a priori*, the position of the flow divide and the appropriate distribution of infiltration to each watershed.

If a groundwater divide is assumed to correspond to the floor of an asymmetric valley, the inferred source of thermal or chemical properties of groundwater samples obtained in springs and boreholes may be incorrectly located beneath the wrong slope. Run K1, shown in Figure 3.7a, depicts an asymmetric mountain valley with mirrored vertical boundaries at the ridgecrests. Opposing ridges have the same relief, but different slope profiles. In the valley discharge area, the groundwater divide is displaced about 0.5 km to the right and deviates slightly from the vertical. Reducing the relief of the righthand slope to one-half that of the lefthand slope and reducing the angle of the linear slope causes an additional shift of 1 km to the right (Run K2 shown in Figure 3.7b).

The direction of divide displacement reflects the relative magnitude of flow through each slope profile with displacement occurring away from the slope with maximum flow. It was pointed out earlier that, for a specified relief, the total flow through a convex profile exceeds that of the corresponding linear or concave profile. Therefore, in Runs K1 and K2, the divide is shifted away from the convex ridge towards the linear ridge. Flow patterns shown in Figure 3.7 suggest that groundwater samples collected above the valley floor at springs issuing from the linear slope could reflect chemical conditions beneath the opposing convex slope.

3.3.5 Permeable Horizons and Fracture Zones

Concave slope profiles similar to that shown in Figure 3.8 are common in volcanic terrain and regions with folded sedimentary units. In such regions, thin permeable horizons may be encountered below the valley floor. Figure 3.8 demonstrates how flow patterns are modified by a 100 m thick horizon, with a permeability 10 times that of the surrounding rock, at a depth of 100 m below the valley floor. Total flow through the system increases by 19 percent while the water table elevation declines by 93 m (Run D4 in Table 3.3). The recharge-discharge profile is relatively unaffected because the influence of the permeable zone is distributed evenly across the section. As permeability or thickness of the horizon is increased, its influence is greater. Simulating a permeable horizon within a convex slope profile produces a similar impact on the flow system (Run D4 in Table 3.3). Sub-vertical and dipping fracture zones, however, are more common than permeable horizons in the glaciated crystalline terrain associated with convex topographic profiles.

The response of water table elevation and total flow to a vertical fault zone outcropping at the valley floor in a convex topography is summarized in Table 3.3 (Runs E1 and E2). A 100 m wide fault zone is modeled in Run E1 with a permeability 10 times that of the rock mass k_u. In Run E2, a 0.1 m wide fault zone is simulated with a permeability 10^4

times that of the surrounding rock mass. In both cases, the fault zone is modeled with the transmissivity of the fracture $k_f \cdot b$ equal to $10^3 \cdot k_u$ in units of $m^2 \cdot m$. Note that this definition of transmissivity differs from the product of hydraulic conductivity times thickness usually adopted in isothermal approaches. Run E1 was carried out using triangular elements to represent the fracture zone, while line elements were used in run E2. The resulting influence on water table configurations and total flow is similar for both runs, causing water table declines of about 270 m and changes in total flow of about 10 percent, relative to a reference case without a vertical fracture zone.

Figure 3.9 demonstrates the influence of a steeply dipping fracture zone which outcrops at the floor of an asymmetric valley (Run E4). Simulation results for the case without the fracture zone are shown in Figure 3.7a (Run K1). The fracture zone is modeled with a value of $k_f \cdot b$ equal to $10^3 \cdot k_u$ ($m^2 \cdot m$). The presence of the permeable zone causes a 27 percent increase in total flow. The recharge-discharge profile shown in Figure 3.9 indicates a significant reduction in discharge from the surrounding rock mass because the fracture zone captures about 50 percent of the groundwater flowing through the domain. It is of interest to note that the permeable fracture zone also influences the position of the valley groundwater divide and compensates for the divide displacement caused by the asymmetric topography (Figure 3.7a). A tenfold increase in fracture

zone transmissivity to $10^4 \cdot k_u$ ($m^2 \cdot m$) causes additional displacement of the divide with the result that the divide is found at the location of the fracture zone. Furthermore, this increased permeability causes a 75 percent increase in total flow above that of the unfractured case (Run K1 in Table 3.3) and enables the fracture zone to capture a greater portion of flow through the domain (about 85 percent). This yields a significant impact on both the patterns and magnitudes of groundwater flow. Further increasing the transmissivity of the fracture to $10^5 \cdot k_u$ ($m^2 \cdot m$), however, has little additional influence on the groundwater flow system. As a consequence, below a threshold value of $k_f \cdot b$ equal to about 10^4 ($m^2 \cdot m$) the fracture zone restricts fluid flow in the surrounding rock mass. At values of $k_f \cdot b$ in excess of this value, fluid flux in the system is restricted only by the permeability of the surrounding rock mass. Thermal aspects of spring discharges from through-going fracture zones are discussed in Chapter 4.

Permeable horizons and fault zones influence mountain flow systems by transmitting a reduced fluid potential deep within the mountain massif. This reduced potential causes a redistribution of fluid flow allowing the permeable zone to capture a portion of flow. The maximum influence of permeable zones occurs in convex slope profiles where a greater portion of the flow system lies above the valley floor and is more susceptible to the impact of permeable

horizons. Sub-horizontal features outcropping at the valley floor have the greatest impact on mountain flow systems while increasing angle of dip and increasing distance between the valley floor and the outcrop of the permeable zone reduces the influence of the zone on the flow system. The influence of a permeable horizon on the flow system is also reduced as depth to the horizon increases (Runs D1 and D3 in Table 3.3).

In situations where fracture density is large relative to the scale of a given flow system, an equivalent anisotropic porous medium may be representative of the fracture network. Run F1 (Table 3.3) models a sub-vertical fracture network using an equivalent anisotropic permeability with the vertical permeability enhanced by a ratio of 5:1 above the horizontal permeability. This relatively small increase in vertical permeability causes a significant decline in water table elevation (444 m) and a small increase in total flow (10 percent). Although anisotropic permeability is more likely the rule rather than the exception, it is difficult to measure vertical permeability in field settings.

3.3.6 Glaciers

Glaciers occupying upper mountain slopes will modify infiltration rates and thus, groundwater flow systems. In temperate mid-latitude climates, many glaciers can be assumed to have basal temperatures at the melting point of

water (Paterson 1981), thus, permafrost conditions are absent and groundwater flow can occur at the base of the glacier.

The influence of a glacier on infiltration rates is simulated by computing sub-glacial recharge during the solution procedure. In this procedure, recharge is assumed to result only from ice melted at the bedrock surface by conductive heat flow. Using the latent heat of fusion for ice and the computed magnitude of conductive heat flux at the base of the glacier, infiltration rates are calculated as the volume of ice melted per unit time. Figure 3.10 compares the recharge-discharge profile and water table configuration obtained with a glacier located between an elevation of 1500 and 2000 m on a concave slope (Run G2 in Table 3.3) and the results obtained for an equivalent system without the influence of the glacier (Run M6 in Table 3.3). The flow pattern for Run M6 is similar to those shown for the concave profiles of Figure 2.3. In each case, a uniform I_z of 5.0×10^{-9} m/s is applied downslope of the glacier. In Run M6 this uniform rate is also applied in the region where the glacier is shown. In Run G2 a reduced I_z beneath the glacier is computed with a minimum value of 7.0×10^{-11} m/sec. This reduced infiltration rate distorts the flow system, modifies the recharge-discharge profile (Figure 3.10) and reduces the total flow (Run G2 in Table 3.3). The humped form of the water table reflects the fact that recharge is negligible beneath the glacier, therefore, a portion of the

recharge applied downslope of the glacier margin moves beneath the glacier before circulating at depth to exit at the valley floor. In the corresponding convex case, a glacier located at the same elevation covers a greater portion of the recharge area, and thus there is a greater impact on total flow and water table elevation (Run G1 in Table 3.3). It should be noted that similar results would be obtained if groundwater recharge is restricted by extensive units of low-permeability rock found in upper regions of the domain.

Runs G1 and G2 have an upper zone permeability k_u equal to 10^{-15} m^2. At lower rock mass permeabilities, slightly greater infiltration rates are calculated because reduced fluid flux allows higher rock temperatures and enhanced melting of glacial ice. The combination of higher infiltration rate and lower permeability cause an increase in infiltration ratio I^*. Therefore, at lower rock permeabilities, water table elevations approach the bedrock surface and flow systems are less affected by the glacier. The calculated infiltration rate yields an I^* at the threshold ratio (and a water table configuration everywhere at the bedrock surface) when k_u is less than about 10^{-17} m^2. Simulation results suggest that infiltration rates and total flow may be significantly influenced by glaciers covering recharge areas of mountain flow systems.

In more northerly and inland regions of the Western Cordillera (above a latitude of 50 degrees), the likelihood of finding temperate glaciers is reduced and permafrost conditions may be found beneath glaciers and on slopes that are normally snow- or ice-free in winter. Under such conditions, recharge to groundwater flow systems may be further reduced because the permafrost acts as an impermeable blanket that may produce little fluid by melting.

3.3.7 Non-uniform Infiltration

Infiltration patterns are controlled by a number of factors including slope angle, precipitation patterns, evapotranspiration and soil permeability. The interaction of these factors is complex and few data are available for representative mountain slopes (Barry, 1981). Two factors can be evaluated using simple techniques; slope angle and orographically-controlled precipitation.

Steep slopes reduce available infiltration rates by enhancing surface runoff. An arbitrary non-uniform infiltration rate is incorporated in Runs L1 and L2 (Table 3.3) by multiplying I_z times the cosine of the angle of the bedrock surface θ from horizontal. Modifying I_z using this approach causes a subtle increase in water table slope that modifies patterns of fluid flow to a minor degree near the water table and produces less than 3 percent change in total flow Q (Runs L1 and L2 in Table 3.3).

Barry (1981) summarizes the results of Lauscher (1976) who shows that orography causes precipitation in mountainous terrain to vary with altitude in a manner that depends upon climate. Precipitation in tropical climates increases with elevation to a maximum at about 1 to 1.5 km above the valley floor, and decreases with increasing elevation. In polar climates, precipitation rates tend to decrease slightly with increasing elevation. In this study, mid-latitude climates are of interest and, following the example of Lauscher, precipitation is assumed to increase with increasing altitude.

Few data are available to describe precipitation gradients on mountain slopes. Moreover, correlation between precipitation and available infiltration rates is lacking at the mountain scale. Review of climate data (Bryson and Hare, 1974; Ruffner and Blair, 1975) and reported altitudinal gradients in precipitation (Schermerhorn, 1967; Storr and Ferguson, 1972; Slaymaker and Zeman, 1975) suggest that a threefold increase in precipitation rate for 2000 m of elevation gain is not unusual. In this study, a linear infiltration gradient is assumed to reflect a threefold increase in precipitation rate. The infiltration gradient is applied to both convex and concave profiles using the maximum I_z of 2×10^{-8} m/s at the ridgecrest and k_u of 1×10^{-14} m^2. Results for Runs L3 through L6, tabulated in Table 3.3, indicate that these conditions cause definite differences in predicted water table elevations and a minor difference in

total flow.

Slope effects and orographic effects are defined with reference to variation in surface topography, therefore, their maximum influence is felt when water table elevations are low and there is a substantial variation in surface topography upslope of the point of detachment (POD). Therefore, as k_u is increased or I_z is reduced (more arid climate with relatively high permeability rock), water table elevations are reduced and the influence of these effects increases.

3.3.8 Basal Heat Flow

Increased basal heat flow causes a warming of conduction-dominated and fluid upflow regions, an increase in total flow and a decline in water table elevation (Figure 3.11). Patterns of fluid flow, however, are affected only to a minor degree. Simulation results for H_b equal to 30, 60 and 120 mW/m^2 are tabulated in Table 3.3 for the convex profile (Runs H1, B2 and H2) and for the concave profile (Runs H3, B7 and H4). Flow patterns and temperature fields for basal heat flows of 60 and 120 mW/m^2 are shown for convex Runs B2 and H2 in Figure 11. Fluid flow patterns are similar despite changes in water table elevation and H_b. A small downward shift in pathline position is found in the greater heat flow case because fluid flux is enhanced in regions of warming (Figure 3.11).

3.3.9 Thermal Conductivity

Changes in thermal conductivity of the solid matrix λ^s influence water table elevations and flow rates in a manner similar to that described for variations in basal heat flow, but to a lesser degree. Reduced conductive heat transfer occurs at lower λ^s to cause heating of the thermal regime in regions of fluid upflow and conduction dominated heat transfer. For example, Runs N3 and N4 (Table 3.3) indicate that increasing λ^s from 2.5 to 3.5 W/mK causes increased water table elevations and a minor increase in total flow. Therefore, changes in thermal conductivity have a definite, but relatively small, impact on mountain flow systems.

3.3.10 Surface Temperature

Review of climate data summaries indicates a range in mean annual valley temperatures from about 5 °C to 15 °C in western North America. Incorporating this range of valley temperatures in a series of simulations yields significant differences in water table elevations and minor differences in total flow. As T_r is increased, upper regions of flow are warmed (Runs M5 through M8; Table 3.3) causing lower water table elevations and increased fluid flow. Barry (1981) suggests that atmospheric thermal lapse rates may vary from less than 2 K/km to greater than 8 °/km. In heat flow studies, a linear thermal lapse rate G_l of 5 K/km is often assumed. In this study, non-linear thermal lapse rates are

used in cases where linear thermal lapse rates predict sub-zero temperatures. Two extremes in thermal lapse rate G_l are simulated; 2 K/km and 8 K/km. The greater lapse rate yields lower temperatures at higher elevations. This, in turn, causes higher water table elevations and slightly reduced total flow. (Runs M1 through M4; Table 3.3).

3.4 DISCUSSION

Numerical results described in the preceding section provide insight into the influence of topography, geology, climate and regional heat flow on the patterns and magnitude of groundwater flow in mountainous terrain. These results are summarized in Figure 3.12 by bar graphs of simulated response of water table elevation ΔWT_{max} and total flow ΔQ to each factor that has been considered. This information provides a means for assessing the relative importance of each factor.

Bar graphs shown in Figure 3.12 indicate that bulk permeability has the greatest impact on water table elevations and fluid flow while infiltration rate, glaciers, slope profile and basal heat flow play important, but lesser, roles. In most cases, each factor is varied over a large portion of the possible range of uncertainty associated with estimates of parameter values. Results shown in Figure 3.12 suggest upper bounds for errors in predicting water table elevations and total flow given an inherent

uncertainty in the parameter considered. Exceptions to this generalization include the influence of bulk permeability, permeable fault zones and permeable horizons where only a small portion of the possible range of variation is tested. For example, only a five-fold variation in bulk permeability is shown in Figure 3.12 while uncertainties in permeability estimates are likely to exceed one or two orders of magnitude. Such large variations contribute to uncertainties in estimated water table elevations that might easily exceed 1000 m. Furthermore, characteristics for permeable fault zones and horizons are selected to indicate the minimum thickness and permeability contrast required to influence mountain flow systems. Clearly, thicker zones with higher permeability that intersect other permeable zones will have a much greater influence than that shown in Figure 3.12. Results shown in Figure 3.12 indicate the possible error associated with each individual factor, the total error associated with a particular simulation would reflect the combined influence of each individual error.

Geology influences steady state mountain flow systems through the spatial variability of rock permeability and, to a lesser degree, thermal conductivity. Permeability has a greater impact, in part, because thermal conductivity has a much narrower range of variability (bulk permeability may range from less than 10^{-20} m^2 to about 10^{-14} m^2 while thermal conductivity may range from about 0.5 to 5 W/mK). In addition, numerical results indicate a smaller flow system

response occurs when thermal conductivity is varied by the same factor as bulk permeability. The strong influence of rock permeablility is also noted in the influence of thin permeable horizons (100 m) and fracture zones (0.1 m). Because sparsely distributed features contribute little to the bulk permeability of a mountain massif, estimates of total flow through the mountain massif are only slightly influenced by the absence of information on thin permeable zones. Water table configurations and patterns of groundwater flow, however, may be strongly influenced by unidentified permeable horizons and fracture zones.

Numerical results indicate that surface topography has a pervasive influence on underlying mountain flow systems. Variations in slope profile, topographic relief and three-dimensional form control the overall patterns of groundwater flow in addition to influencing water table elevations and total flow. Of particular importance is the ability of asymmetric topography to displace groundwater flow divides from the corresponding topographic divides. In using model studies to assess the source of chemical signatures in water samples from springs or in estimating inter-basin groundwater flow, the region modeled should extend sufficient distance to include ridge and valley topography adjacent to the mountain slope of interest. Although surface topography can easily be resolved using readily available topographic information, incorporating complex three-dimensional topography into an analysis of

mountain flow systems is less easily accomplished.

Thermal energy introduced into mountain flow systems by regional heat flow plays an important role in defining subsurface temperatures that, in turn, influence the nature of groundwater flow in mountains. Thermal regimes computed for flow systems with homogeneous isotropic permeability and normal regional heat flow (60 mW/m^2) suggest that temperatures 2 km below the valley floor may range from 90°C to 40°C as the bulk permeability of the mountain massif is varied from less than 10^{-18} m^2 to 10^{-15} m^2. Doubling the basal heat flow causes a doubling of temperatures in conduction-dominated and fluid-upflow zones while temperatures in other regions of the flow system are essentially unaffected. Because fluid density and viscosity depend upon temperature, increased basal heat flow leads to higher subsurface temperatures, increased rates of groundwater flow and reduced water table elevations. Although basal heat flow is normally assumed to range from about 30 to 120 mW/m^2, advective heat transfer by groundwater flow in mountainous terrain often inhibits accurate estimates of heat flow. This uncertainty in basal heat flow, therefore, contributes to uncertainty in estimating water table elevation and total flow. This dependence of the groundwater flow system on regional heat flow suggests that isothermal approaches to modeling groundwater flow in mountainous terrain may be inappropriate.

Climate influences the nature of mountain flow systems through variations in available infiltration rates, variations in surface temperature and the presence or absence of alpine glaciers. Numerical results indicate that large variations in mean annual surface temperature (5 to 15 °C) and thermal lapse rate (2 to 8 K/km) exert only a minor influence on mountain flow systems. Therefore, although surface temperature measurements can be made with reasonable accuracy, only rough estimates may be needed when assessing water table configurations and groundwater flow rates in mountainous terrain.

Although available infiltration rates are expected to vary over a much narrower range than rock permeability, each parameter can exert a similar influence on water table elevations in mountain flow systems. Unfortunately, it is difficult to make measurements of available infiltration rates that are meaningful at a mountain scale. Numerical results indicate that, if a reasonable estimate of infiltration rate can be made (perhaps as a percentage of mean annual precipitation), the spatial variation of infiltration on the upper surface contributes little to variations in the overall nature of the mountain flow system. Therefore, in most cases a uniform infiltration rate can be assumed.

Climatic conditions that contribute to development of alpine glaciers can have an important impact on flow systems

in permeable mountainous terrain where glaciers act as barriers to groundwater recharge. The character and spatial distribution of alpine glaciers is relatively easily defined by field mapping, however, the details of sub-glacial groundwater recharge are difficult to assess without a complete water budget analysis within the basin of interest.

Calculated total flow through each hypothetical flow system represents a deep subsurface component of baseflow that is often neglected in water budget computations. The magnitude of the total flow is dominated by bulk permeability (represented here by the upper zone permeability k_u) and infiltration rate I_z. In this study, an upper limit for infiltration to deep flow systems is estimated to be 2×10^{-8} m/sec (0.6 m/yr). This large infiltration can only be transmitted through high permeability terrain (in excess of 10^{-15} m^2) in a mountain slope with relief of 2 km over 6 km and a normal regional heat flow (60 mW/m^2). As bulk permeability is reduced, the maximum infiltration that can be transmitted by the flow system is reduced. Consider an infiltration rate of 2×10^{-10} m/sec (0.006 m/yr). This infiltration rate is a small portion of typical precipitation rates (in excess of 1.0 m/yr in humid coastal climates and as low as 0.4 m/yr in semi-arid climates) yet can only be transmitted through terrain with permeability in excess of 10^{-16} m^2. Therefore, in terrain with permeability less than 10^{-16} m^2 and with a humid climate, only a small portion of the mean annual

precipitation is transmitted through deep flow systems.

Recharge to deep flow systems may be approximated by measuring vertical hydraulic gradients and permeability below the bedrock surface. Such measurements are costly and usually represent conditions only in the immediate vicinity of the measurement point. Furthermore, extrapolating measured values to other parts of the flow region is fraught with uncertainty. In many instances, thin surficial deposits and open fractures near the bedrock surface may transmit a substantial portion of groundwater that appears as baseflow in water budget calculations yet is not transmitted through deep flow systems. Therefore, estimates of recharge to deep flow systems may be poorly approximated by a water balance approach that assumes all baseflow travels through the deep flow system.

The water table elevation is a sensitive indicator of the influence of factors controlling groundwater flow systems. This high degree of sensitivity suggests that predicting water table configurations in mountainous terrain will be difficult due to uncertainties inherent in resolving the magnitude of many of the controlling factors. Mapping water table elevations high in the mountain massif through drilling or geophysical surveys, however, may assist in constraining parameters such as rock permeability and available infiltration rate. It seems reasonable to assume that water table elevations obtained from such activities

will reflect an averaging of permeability and infiltration rate that would be difficult to obtain from a series of point measurements of each parameter. Unfortunately, uncertainties in basal heat flow (in addition to difficulties inherent in defining the character and distribution of thin permeable horizons and fault zones) inhibit defining a unique set of characteristics that might cause the observed water table configuration.

Throughout this Chapter, steady state hydrologic and thermal conditions have been assumed. Diurnal and seasonal variations in climate cause periodic fluctuations in surface temperature and infiltration rates. Buntebarth (1984) shows that seasonal changes in surface temperature are less than 10^{-3} °C at depths in the order of 30 m in conduction-dominated thermal regimes. In mountain-scale systems, such shallow penetration of seasonal temperature changes will not induce significant variations to overall patterns and magnitudes of groundwater flow. Seasonal changes in infiltration rate are reported to cause seasonal fluctuations in mountaintop water table elevations of about 10 to 20 m (Halstead, 1969 and Province of British Columbia, 1974). Numerical results described in the previous section indicate that minimal changes in flow patterns and total flow rates are associated with such small changes in water table elevation. Therefore, periodic diurnal and seasonal transients (both thermal and hydraulic) can be neglected when studying deep groundwater flow in mountainous terrain.

Longer-term variations in thermal and hydrologic conditions may result from ongoing processes of igneous activity, orogeny, erosion and climate change. In assessing the geochemical history and transit times of groundwater samples, the influence of these processes may become important. Recall that a characteristic transit time along the lowermost pathlines in Figure 3.1 can be estimated by assuming the available infiltration rate I_z is a reasonable estimate of volumetric specific discharge within the domain (Section 3.2). For a system with permeability 10^{-15} m^2, transit times are about 8×10^5 years. Glacial events and plutonic activity (Norton and Knight, 1977) can cause significant perturbations to the hydrologic and thermal regimes during this time period. Major glacial advances and retreats have also occurred over the same time period. Fluid transit times in the order of 10^5 years, and longer, suggest that fluid entering the system as recharge at a particular point in time may bear the imprint of hydrologic, thermal and chemical conditions that no longer exist.

3.5 CONCLUSIONS

1. Simulation results indicate that slope profile, rock permeability, infiltration rate, glaciers and basal heat flow exercise a strong influence on water table configurations and the rates of groundwater flow. For example, a three-fold increase in permeability (or a three-fold decrease in available infiltration rate) can

cause at least 500 m decline in water table elevation and a 45 percent change in total flow through a system with relief of 2 km over 6 km. Variations of similar magnitude are found to result when; a) two extremes of slope profile are compared (concave and convex), b) alpine glaciers act to restrict groundwater recharge, c) thin permeable fracture zones and horizons are incorporated in the flow system and d) two extremes of basal heat flow are compared (30 to 120 mW/m^2). It should be noted that the dependence of water table elevation and fluid flux on regional heat flow suggests that model studies conducted using an isothermal approach may be inappropriate, even in regions with normal basal heat flow (60 mW/m^2).

2. The high topographic relief of mountainous terrain amplifies the impact of slope profile and thin permeable zones on patterns of groundwater flow. For example, asymmetry in ridge topography alone can cause significant displacement of upland groundwater divides that, in turn, may enhance inter-basin groundwater flow. Furthermore, lowland groundwater divides displaced by asymmetry in valley topography can lead to uncertainties in defining the source of chemical signatures found in groundwater samples obtained from springs and shallow boreholes. Thin permeable fault zones and horizons (thickness of 0.1 m and permeability 10^4 times the surrounding rock or thickness of 100 m and permeability 10 times the surrounding rock) exert a strong influence on groundwater flow patterns. This influence

further enhances the possibility of inter-basin groundwater flow and complicates accurate interpretation of chemical sampling results.

3. In modeling groundwater flow in mountainous terrain, it is useful to first simulate a fully saturated system and compare computed recharge rates with an estimated minimum value for the threshold infiltration ratio. If computed recharge rates in the saturated case approach or exceed the threshold a free-surface approach should be considered.

4. Simulation results suggest that water table positions are likely to be found at relatively high elevations in most mountainous terrain. Exceptions to this generalization should be expected in terrain with relatively high permeability (bulk permeability in excess of 10^{-15} m^2) and arid climate (infiltration less than 10^{-11} m/sec), or where alpine glaciers restrict groundwater recharge. In lower-permeability terrain, less than one percent of typical mean annual precipitation rates may be transmitted through deep regions of groundwater flow.

REFERENCES

Barry, R.G., Mountain weather and climate, Methuen, 1981.

Bryson, R.A., and F.K. Hare, Climates of North America, Elsevier, 1974.

Buntebarth, B., Geothermics, Springer-Verlag, 1984.

Freeze, R.A., and J.A. Cherry, Groundwater, Prentice-Hall Inc., 1979.

Halstead, E.C., Groundwater investigation, Mount Kobau, British Columbia, Canada Inland Waters Branch, Dept. of Energy Mines and Resources, Tech. Bull. 17, 1969.

Lauscher, F., Wettweite typen der hohenabgangigkeit des Niederschlags, Wetter U. Leben., 28, 80-90, 1976.

Neuzil, C.E., Groundwater flow in low-permeability environments, Water Resour. Res., 22(8), 1163-1196, 1986.

Norton, D., and J. Knight, Transport phenomena in hydrothermal systems: Cooling plutons, Amer. Jour. of Sci., 277, 937-981, 1977.

Paterson, W.S.B., The physics of glaciers, Pergamon, 1981.

Province of British Columbia, Groundwater observation wells of British Columbia, British Columbia Water Resources Service, Water Investigations Branch, 1974.

Ruffner, J.A., and F.E. Blair, Climates of the States with current tables of normals 1941-1970 and means and extremes to 1975, National Ocean and Atmospheric Adimin., Vols. I and II, 1975.

Schermerhorn, V.P., Relations bewteen topography and annual precipitation in Western Oregon and Washington, Water Resour. Res., 3(3), 707-711, 1967.

Slaymaker, H.O., and L.J. Zeman, Influence of altitude and continentality on watershed hydrology in the Coast Mountains of British columbia, Proc. Canadian Hydrology Symposium, National Research Council, 1975.

Storr, D., and H.L. Ferguson, The distribution of precipitation in some mountainous Canadian watersheds, in, Distribution of Precipitation in Mountainous Areas, Geilo Symposium, Norway, Proc. World Meteor. Assoc., WMO/OMM No. 326, Vol. II, 243-263, 1972.

TABLE 3.1

SIMULATION SUMMARY AND GUIDE TO ILLUSTRATIONS - CHAPTER 3

FACTOR	SIMULATION SERIES *	FIGURE
TOPOGRAPHY		
Slope Profile	A	3.1
Radial Symmetry	I	3.5
Ridge Asymmetry	J	3.6
Valley Asymmetry	K	3.7
Topographic Relief	O	NS
GEOLOGY		
Bulk Permeability	C	3.2
Permeable Horizons	D	3.8
Permeable Fracture Zones	E	3.9
Basin Depth	P	NS
Thermal Conductivity	N	NS
Anisotropic Permeability	F	NS
CLIMATE		
Available Infiltration	B	3.2
Alpine Glaciers	G	3.10
Non-Uniform Infiltration	L	NS
Surface Temperature	M	NS
THERMAL REGIME		
Basal Heat Flow	H	3.11

Notes:

* Simulation results are presented in Table 3.3

NS Not Shown

TABLE 3.2

TYPICAL SIMULATION PARAMETERS - CHAPTER 3

Fluid Flow Parameters

k_b		permeability of basal unit	1.0×10^{-22} m^2
k_u	*	permeability of upper unit	1.0×10^{-15} m^2
I_z	*	vertical infiltration rate	2.0×10^{-9} m/sec

Thermal Parameters

H_b	*	basal heat flow	60.0 mW/m^2
G_l	*	thermal lapse rate	5 K/km
T_r	*	reference surface temperature	10 °C
n_b		porosity of basal unit	0.01
n_u	*	porosity of upper unit	0.10
λ^s	*	solid thermal conductivity	2.50 W/mK
λ^f		fluid thermal conductivity	0.58 W/mK
λ^v		vapor thermal conductivity	0.024 W/mK
C_f		specific heat capacity of water	4186.0 J/kgK
S		saturation above water table	0.0
a_l		longitudinal thermal dispersivity	100.0 m
a_t		transverse thermal dispersivity	10.0 m

Note: * Denotes parameters changed in simulation series.

TABLE 3.3
SIMULATION RESULTS

RUN #	PROFILE TYPE	k_u (m^2)	I_z (m/sec)	I^*	Q (kg/sec)	Q^*	WT_{max} (m)	REF. RUN	ΔWT (m)	ΔQ (%)	COMMENTS
A. SLOPE PROFILE											
A1	X	10^{-15}	3×10^{-9}	0.40	1.2×10^{-2}	0.26	1950	.	.	.	
A2	V	10^{-15}	3×10^{-9}	0.40	5.6×10^{-3}	0.12	1053	A1	-897	-53	
A3	L	10^{-15}	2×10^{-9}	0.26	6.4×10^{-3}	0.14	1270	.	.	.	
A4	L	10^{-15}	5×10^{-9}	0.66	7.5×10^{-3}	0.17	1977	.	.	.	
B. INFILTRATION RATE											
B1	X	10^{-15}	1×10^{-9}	0.13	5.4×10^{-3}	0.12	924	A1	-1026	-55	
B2	X	10^{-15}	2×10^{-9}	0.26	1.0×10^{-2}	0.22	1543	A1	-407	-17	
B3	X	10^{-15}	5×10^{-9}	0.66	1.2×10^{-2}	0.26	2000	A1	+50	0	> Threshold
B4	X	10^{-15}	7×10^{-9}	0.92	1.2×10^{-2}	0.26	2000	A1	+50	0	> Threshold
B5	V	10^{-15}	1×10^{-9}	0.13	3.3×10^{-3}	0.07	490	A2	-563	-41	
B6	V	10^{-15}	2×10^{-9}	0.26	4.9×10^{-3}	0.11	805	A2	-248	-13	
B7	V	10^{-15}	5×10^{-9}	0.66	6.3×10^{-3}	0.14	1486	A2	+433	+13	
B8	V	10^{-15}	7×10^{-9}	0.92	6.4×10^{-3}	0.14	1896	A2	+843	+14	

TABLE 3.3 (Cont'd)
SIMULATION RESULTS

RUN #	PROFILE TYPE	k_u (m^2)	I_z (m/sec)	I^*	Q (kg/sec)	Q^*	WT_{max} (m)	REF. RUN	ΔWT (m)	ΔQ (%)	COMMENTS
C. UPPER ZONE PERMEABILITY											
C1	X	10^{-18}	2×10^{-12}	0.26	1.0×10^{-5}	0.22	1560	B2	+17	-100	
C2	X	10^{-16}	2×10^{-10}	0.26	1.0×10^{-3}	0.22	1550	B2	+7	-90	
C3	V	10^{-18}	5×10^{-12}	0.66	6.2×10^{-6}	0.14	1491	B7	+5	-100	
C4	V	10^{-16}	5×10^{-10}	0.66	6.2×10^{-4}	0.14	1488	B7	+2	-90	
D. PERMEABLE HORIZONS (100 m thick, $k = 10k_u$)											
D1	X	10^{-16}	2×10^{-10}	0.22	1.0×10^{-3}	0.22	1472	C2	-78	-1	Elev.=-1800m
D2	X	10^{-16}	2×10^{-10}	0.22	1.0×10^{-3}	0.23	1316	C2	-234	+4	Elev.=-100m
D3	V	10^{-16}	5×10^{-10}	0.66	6.8×10^{-4}	0.15	1442	C4	-46	-10	Elev.=-1800m
D4	V	10^{-16}	5×10^{-10}	0.66	7.4×10^{-4}	0.16	1395	C4	-93	+19	Elev.=-100m
E. PERMEABLE FRACTURE ZONES											
E1	X	10^{-16}	2×10^{-10}	0.22	1.1×10^{-3}	0.24	1292	C2	-258	+10	!,100m,$10k_u$
E2	X	10^{-16}	2×10^{-10}	0.22	1.1×10^{-3}	0.24	1263	C2	-287	+10	!,0.1m,10^4k_u
E3	X	10^{-16}	2×10^{-10}	0.22	1.1×10^{-3}	0.24	1245	C2	-305	+10	/,0.1m,10^4k_u
E4	X	10^{-15}	2×10^{-9}	0.22	1.1×10^{-2}	0.24	954	B2	-589	+10	/,1.0m,10^4k_u
	L				7.5×10^{-3}	0.17	1067	A3	-203	+17	Asymm.

TABLE 3.3 (Cont'd)
SIMULATION RESULTS

RUN #	PROFILE TYPE	k_u (m^2)	I_z (m/sec)	I^*	Q (kg/sec)	Q^*	WT_{max} (m)	REF. RUN	ΔWT (m)	ΔQ (%)	COMMENTS
F. ANISOTROPIC PERMEABILITY											
F1	X	10^{-16}	2×10^{-10}	0.22	1.1×10^{-3}	0.24	1106	C2	-444	+10	$k_z=5k_u$, $k_x=k_u$
G. GLACIER BETWEEN ELEVATION 1500 m and 2000 m											
G1	X	10^{-15}	2×10^{-9}	0.26	3.7×10^{-3}	0.08	517	M5	-1099	-62	
G2	V	10^{-15}	5×10^{-9}	0.66	4.7×10^{-3}	0.10	752	M7	-829	-18	
H. BASAL HEAT FLOW											
H1	X	10^{-15}	2×10^{-9}	0.26	1.1×10^{-2}	0.20	1911	B2	+368	-10	H_b=30 mW/m²
H2	X	10^{-15}	2×10^{-9}	0.26	9.1×10^{-3}	0.23	1137	B2	-406	+9	H_b=120 mW/m²
H3	V	10^{-15}	5×10^{-9}	0.66	5.1×10^{-3}	0.11	1697	B7	+211	-19	H_b=30 mW/m²
H4	V	10^{-15}	5×10^{-9}	0.66	8.3×10^{-3}	0.18	1152	B7	-334	+32	H_b=120 mW/m²

TABLE 3.3 (Cont'd)
SIMULATION RESULTS

RUN #	PROFILE TYPE	k_u (m^2)	I_z (m/sec)	I^*	Q (kg/sec)	Q^*	WT_{max} (m)	REF. RUN	ΔWT (m)	ΔQ (%)	COMMENTS
I. RADIAL SYMMETRY											
I1	X	10^{-15}	$2x10^{-9}$	0.26	$1.1x10^{-2}$	0.24	1272	B2	-271	+1	Planar
I2	X	10^{-15}	$2x10^{-9}$	0.26	$2.0x10^{2}$	•	786	I1	-486	•	Radial
I3	V	10^{-15}	$5x10^{-9}$	0.66	$6.4x10^{-3}$	0.14	1484	B7	-2	+2	Planar
I4	V	10^{-15}	$5x10^{-9}$	0.66	$8.0x10^{1}$	•	1233	I3	-251	•	Radial
J. ASYMMETRIC RIDGE											
J1	VX	10^{-15}	$3x10^{-9}$	0.40	$1.8x10^{-2}$	•	1488	•	•	•	
K. ASYMMETRIC VALLEY											
K1	X	10^{-15}	$2x10^{-9}$	0.26	$1.0x10^{-2}$	0.22	1438	B2	-105	0	Relief=2 km
	L				$6.0x10^{-3}$	0.13	1208	A3	+62	+5	Relief=2 km
K2	X	10^{-15}	$2x10^{-9}$	0.26	$1.0x10^{-2}$	0.22	1366	B2	-177	0	Relief=2 km
	L				$3.3x10^{-3}$	0.07	869	•	•	•	Relief=1 km
K3	V	10^{-15}	$5x10^{-9}$	0.66	$6.0x10^{-3}$	0.13	1494	B7	+8	0	Relief=2 km
	L				$8.5x10^{-2}$	0.19	1758	A4	-219	+13	Relief=2 km

TABLE 3.3 (Cont'd)
SIMULATION RESULTS

RUN #	PROFILE TYPE	k_u (m^2)	I_z (m/sec)	I^*	Q (kg/sec)	Q^*	WT_{max} (m)	REF. RUN	ΔWT (m)	ΔQ (%)	COMMENTS
L. NON-UNIFORM INFILTRATION PATTERNS											
L1	X	10^{-15}	2×10^{-9}	0.26	9.8×10^{-3}	0.15	1528	B2	-15	-2	Slope Eff.
L2	V	10^{-15}	5×10^{-9}	0.66	6.1×10^{-3}	0.13	1350	B7	-136	-3	Slope Eff.
L3	X	10^{-14}	2×10^{-8}	0.26	1.2×10^{-1}	0.22	1543	·	·	·	Uniform
L4	X	10^{-14}	2×10^{-8}	·	9.1×10^{-2}	0.20	1477	L3	-66	-24	Orogr. Eff.
L5	V	10^{-14}	2×10^{-8}	0.26	4.9×10^{-2}	0.11	805	·	·	·	Uniform
L6	X	10^{-14}	2×10^{-8}	·	4.1×10^{-2}	0.09	705	L5	-100	-16	Orogr. Eff.
M. SURFACE TEMPERATURE CONDITIONS											
M1	X	10^{-15}	2×10^{-9}	0.26	1.0×10^{-2}	0.22	1478	B2	-65	0	G_l=2°C/km
M2	X	10^{-15}	2×10^{-9}	0.26	9.8×10^{-3}	0.22	1569	B2	+26	-2	G_l=8°C/km
M3	V	10^{-15}	5×10^{-9}	0.66	6.5×10^{-3}	0.14	1415	B7	-71	+3	G_l=2°C/km
M4	V	10^{-15}	5×10^{-9}	0.66	6.1×10^{-3}	0.13	1536	B7	+50	-3	G_l=8°C/km
M5	X	10^{-15}	2×10^{-9}	0.26	9.6×10^{-3}	0.21	1616	B2	+73	-3	T_r=5°C
M6	X	10^{-15}	2×10^{-9}	0.26	1.0×10^{-2}	0.23	1436	B2	-107	0	T_r=15°C
M7	V	10^{-15}	5×10^{-9}	0.66	5.7×10^{-3}	0.13	1581	B7	+95	-10	T_r=5°C
M8	V	10^{-15}	5×10^{-9}	0.66	6.9×10^{-3}	0.15	1375	B7	-111	+10	T_r=15°C

TABLE 3.3 (Cont'd)
SIMULATION RESULTS

RUN #	PROFILE TYPE	k_u (m^2)	I_z (m/sec)	I^*	Q (kg/sec)	Q^*	WT_{max} (m)	REF. RUN	ΔWT (m)	ΔQ (%)	COMMENTS
N. THERMAL CONDUCTIVITY OF ROCK-FLUID COMPOSITE											
N1	X	10^{-15}	2×10^{-9}	0.26	1.0×10^{-2}	0.22	1478	B2	-65	0	n_u=0.01
N2	V	10^{-15}	7×10^{-10}	0.92	6.2×10^{-3}	0.14	1931	B8	+35	-3	n_u=0.01
N3	X	10^{-15}	2×10^{-9}	0.26	9.6×10^{-3}	0.21	1731	B2	+188	-4	λ^S=3.5W/m°C
N4	V	10^{-15}	5×10^{-9}	0.66	5.6×10^{-3}	0.12	1601	B7	+115	-11	λ^S=3.5W/m°C
O. TOPOGRAPHIC RELIEF (1 km relief)											
O1	V	10^{-15}	2×10^{-9}	0.26	2.9×10^{-3}	0.07	483	B6	-322	-41	
O2	V	10^{-15}	2×10^{-9}	0.26	4.8×10^{-3}	0.10	836	B6	+31	-2	Trunc.
O3	X	10^{-15}	9×10^{-10}	0.12	5.0×10^{-3}	0.11	936	•	•	•	Trunc.
P. BASIN DEPTH											
P1	V	10^{-15}	5×10^{-9}	0.26	5.0×10^{-3}	0.11	1590	B7	+94	-21	1km deep

TABLE 3.3 (Cont'd)
SIMULATION RESULTS

Notes:

1) Slope Profile; X = convex, V = concave, L = linear.

2) !,100m,10k_u; Vertical fracture zone at extreme right of system, thickness is 100 m, permeability is 10 times k_u.

3) /,0.1m,$10^4 k_u$; Steeply dipping fracture zone outcropping at valley floor, thickness is 0.1 m, permeability is 10^4 times k_u.

4) k_z, k_x; vertical and horizontal components of anisotropic permeability.

5) H_b = basal heat flow.

6) G_l = thermal lapse rate.

7) T_r = valley reference temperature.

8) n_u = upper zone porosity.

9) λ^s = rock thermal conductivity.

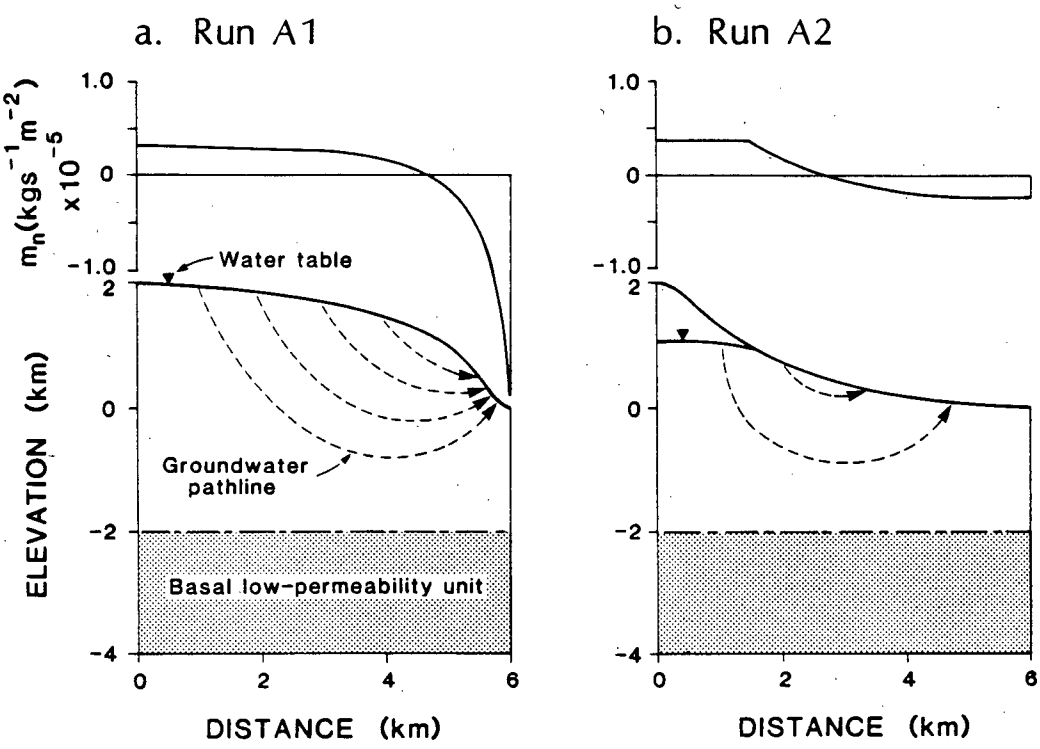

Figure 3.1. Groundwater flow patterns, water table configurations and recharge-discharge profiles as a function of slope profile;
a) convex Run A1,
b) concave Run A2.

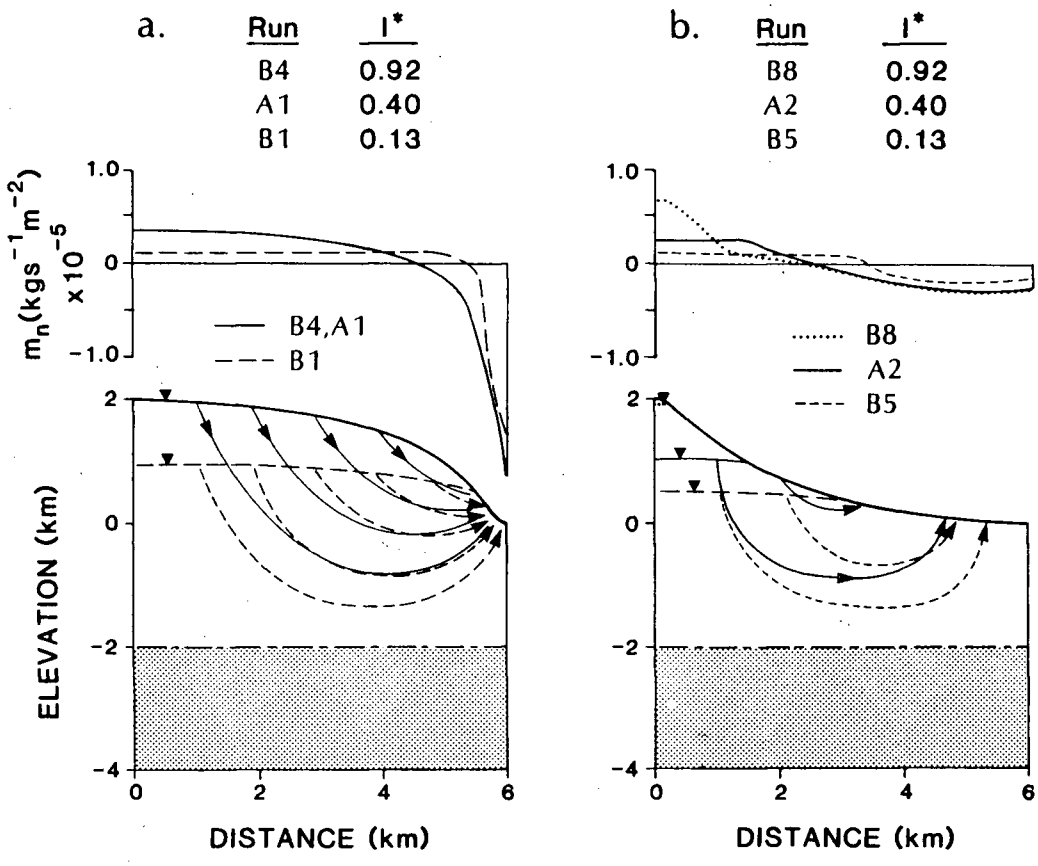

Figure 3.2. Influence of infiltration ratio I^* on water table configuration, flow patterns and recharge-discharge profiles;
a. convex (Runs B4, A1, B1),
b. concave (Runs B8, A2, B5).

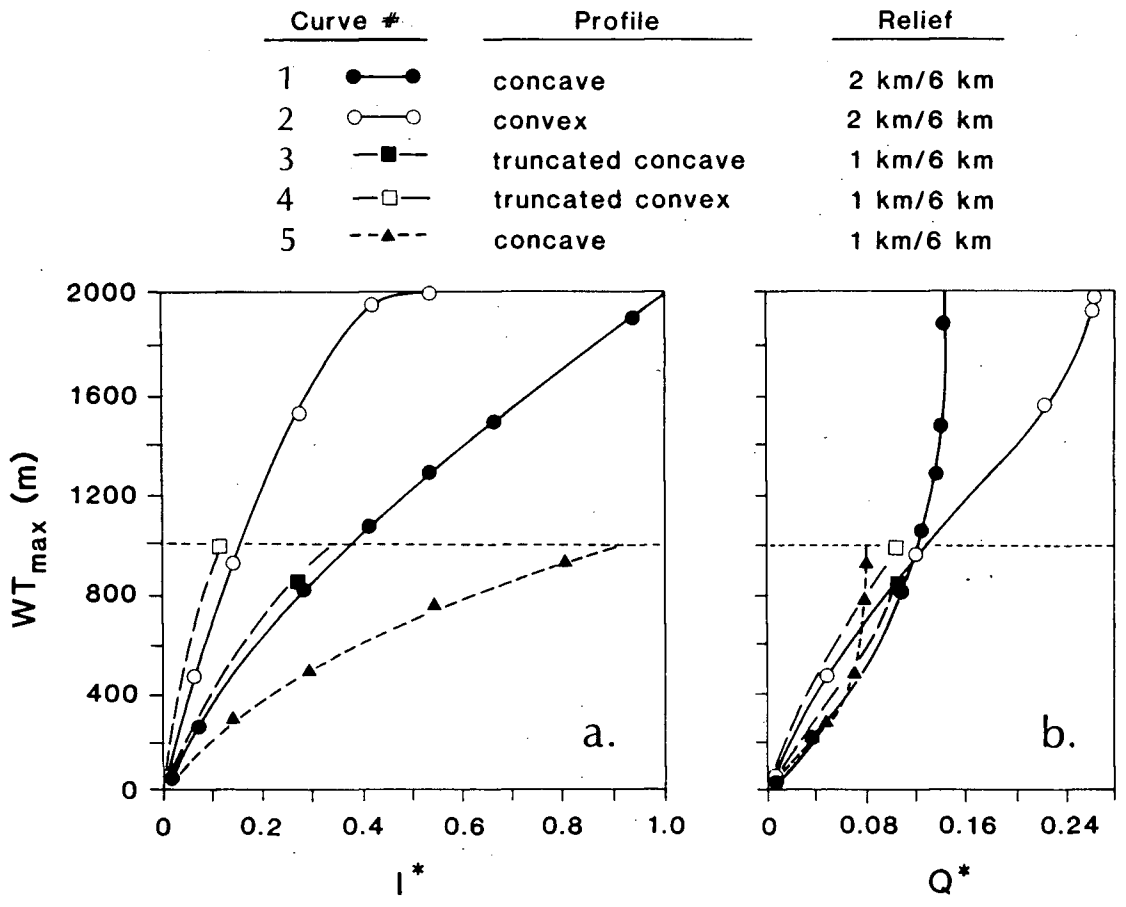

Figure 3.3. Water table elevation WT_{max} as a function of;
a. infiltration ratio I^*, and
b. dimensionless total flow Q^*.

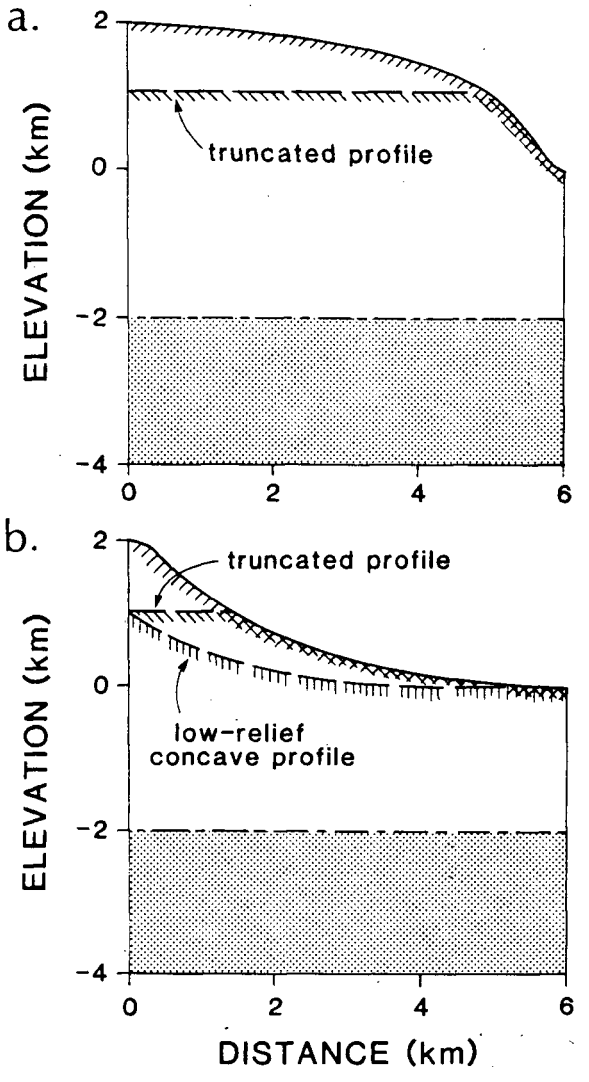

Figure 3.4. Modified surface topographies;
a. convex profiles,
b. concave profiles.

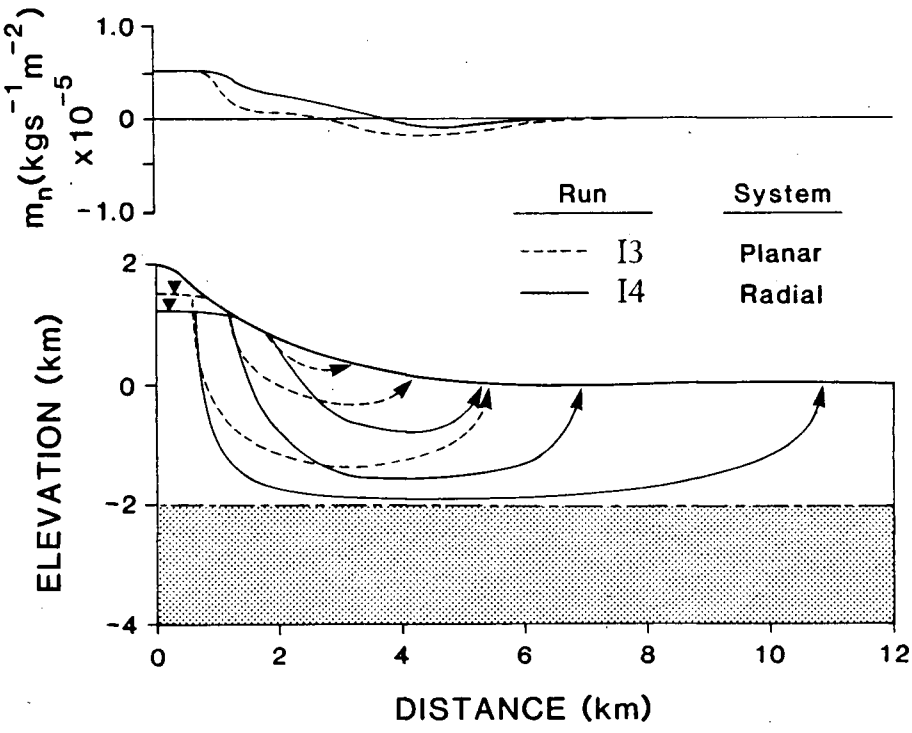

Figure 3.5. Influence of radial symmetry on water table configurations, flow patterns and recharge-discharge profiles (Runs I3 and I4).

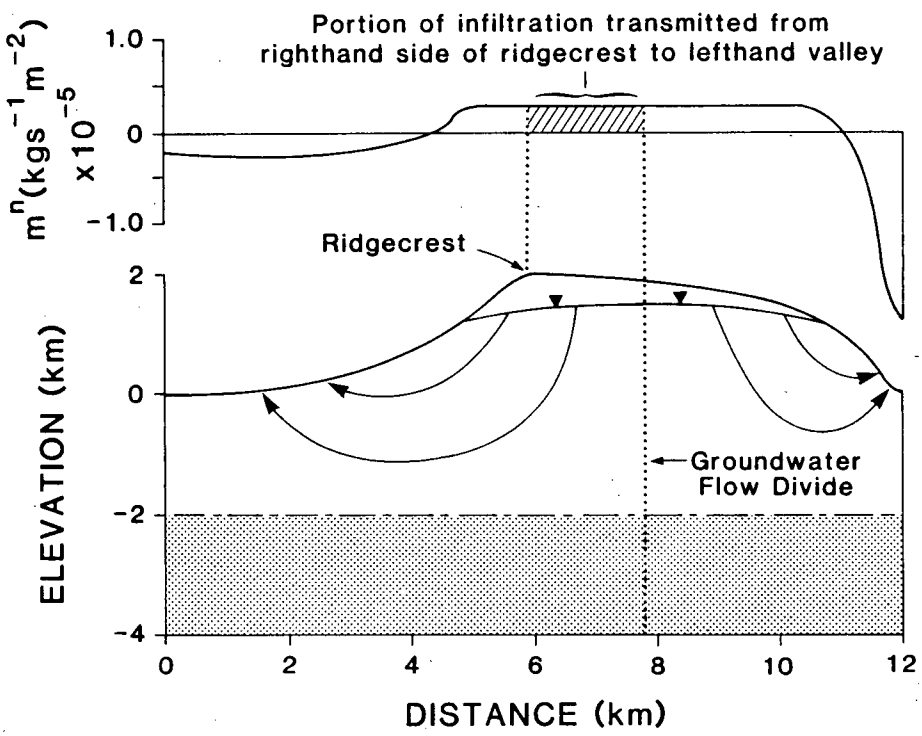

Figure 3.6. Influence of ridge asymmetry on water table configuration, flow patterns and recharge-discharge profile (Run J1).

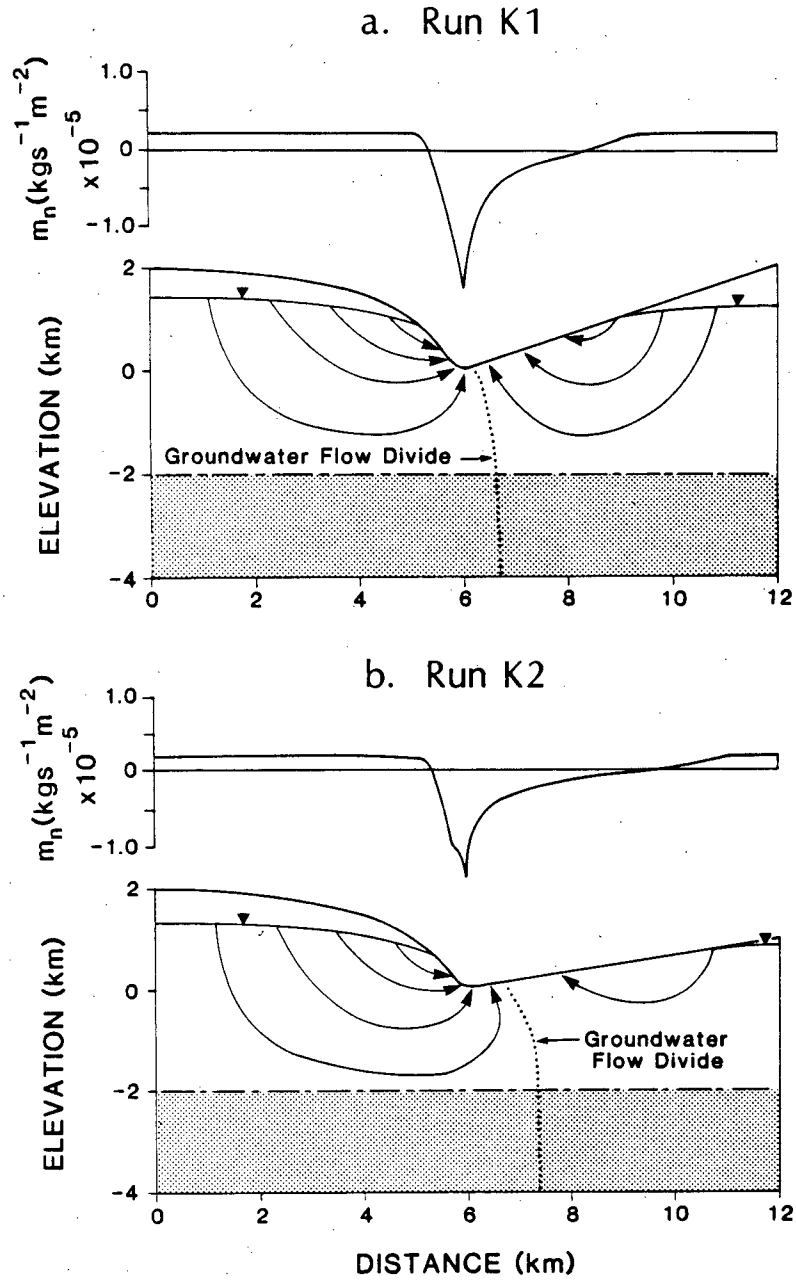

Figure 3.7. Influence of valley asymmetry on water table configuration, flow patterns and recharge-discharge profiles;
a. relief of opposing ridges are equal (Run K1), and
b. relief of opposing ridges are unequal (Run K2).

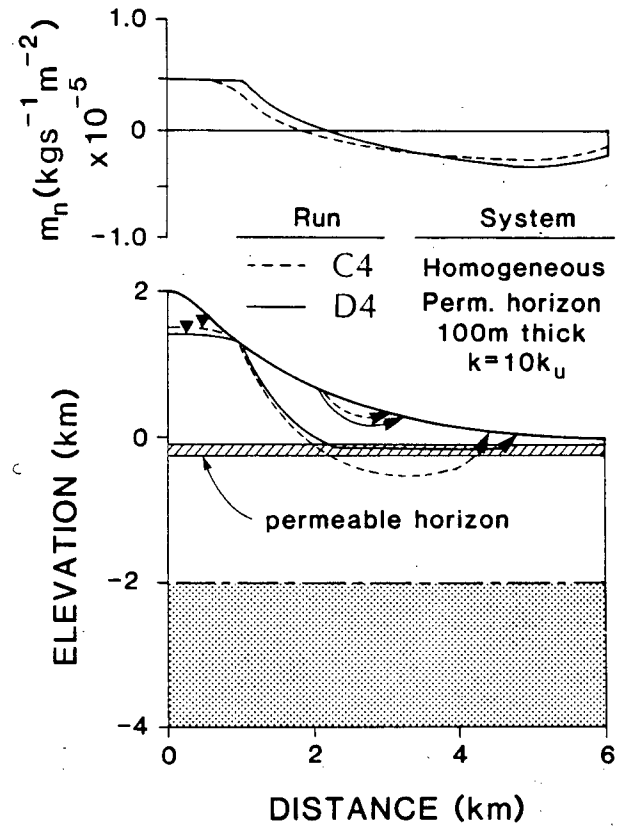

Figure 3.8. Influence of a permeable horizon 100 m thick with permeability 10 times k_u located 100 m below the valley floor (Run D4).

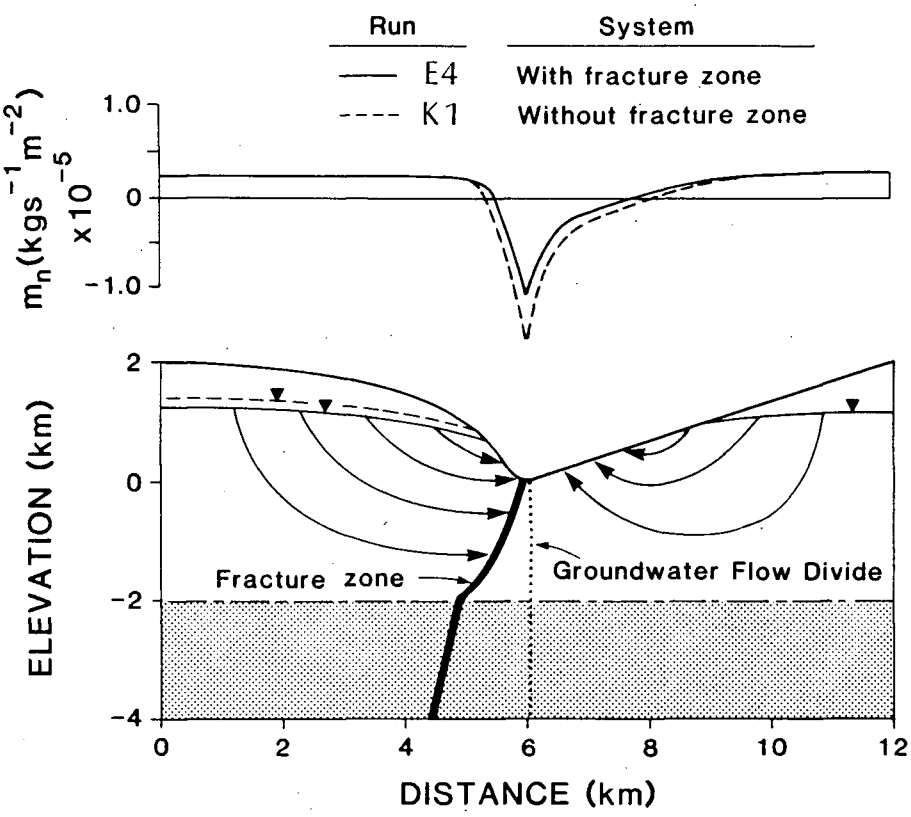

Figure 3.9. Influence of a steeply dipping fracture zone that outcrops at the valley floor (Run E4). The zone is 0.1 m thick with permeability 10^4 times k_u.

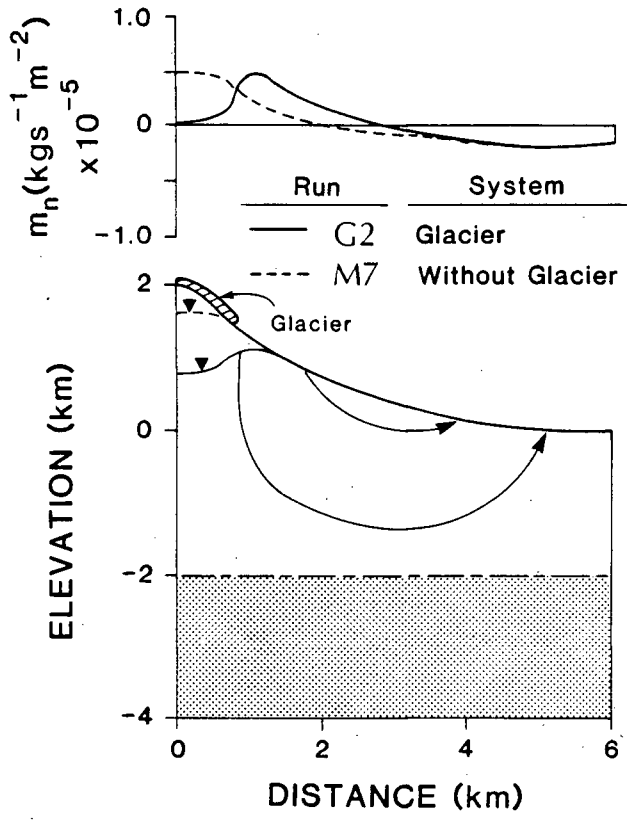

Figure 3.10. Influence of a glacier extending from an elevation of 2000 m to 1500 m above the valley floor on water table configuration, flow pattern and recharge-discharge profile (Run G2).

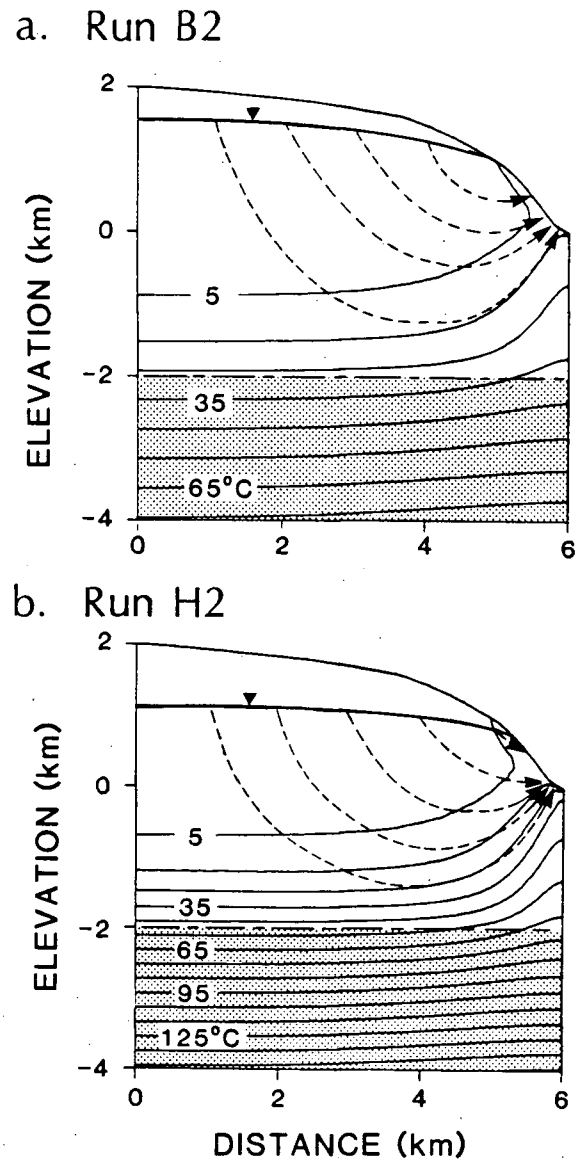

Figure 3.11. Influence of basal heat flow on water table configuration, flow pattern and thermal regime;
a. H_b = 60 mW/m² (Run B2), and
b. H_b = 120 mW/m² (Run H2).

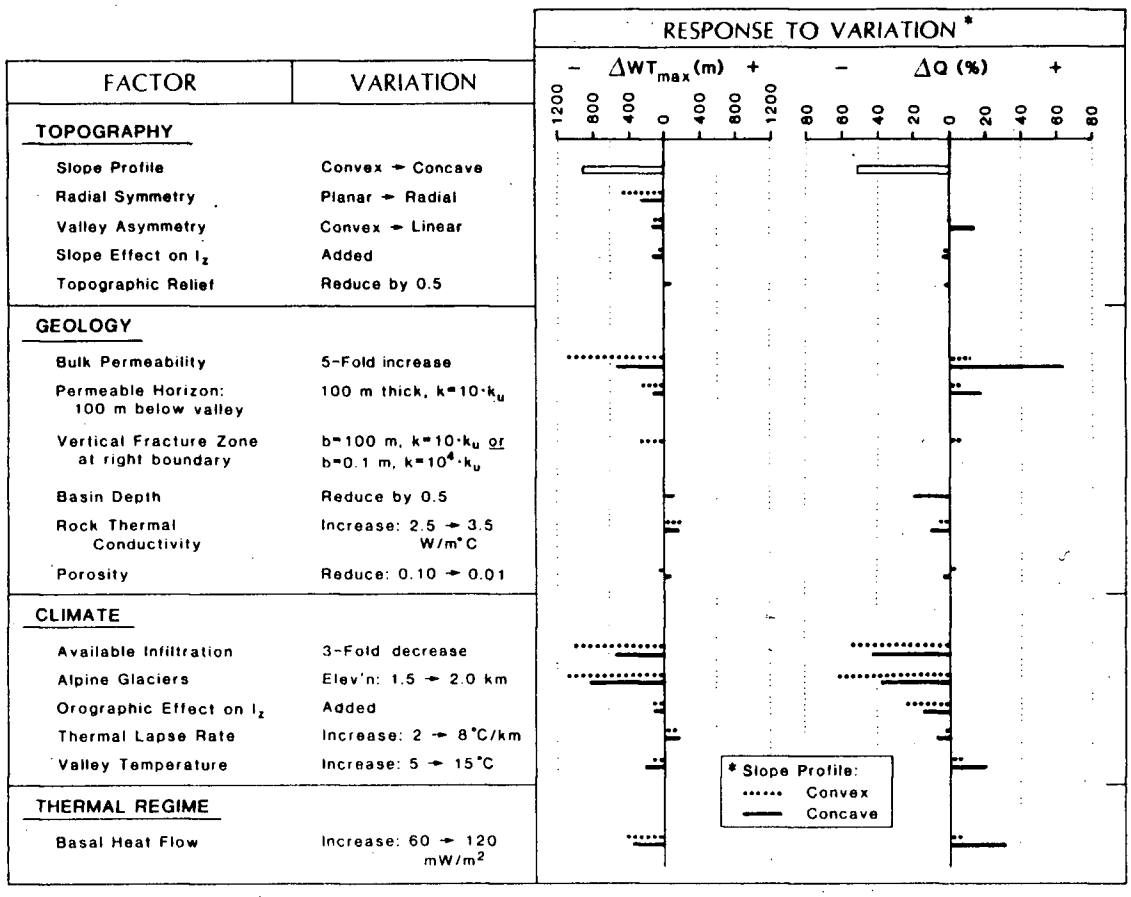

Figure 3.12. Summary of the influence of factors controlling water table elevation (WT_{max}) and total flow (Q).

CHAPTER 4

THERMAL REGIMES IN MOUNTAINOUS TERRAIN

4.1 INTRODUCTION

It is widely recognized that topographically-driven groundwater flow can perturb conductive thermal regimes (Sass *et al.*, 1971; Brott *et al.*, 1981; Mase *et al.*, 1982). Numerical results described in Chapter 3 illustrate how high-relief topography amplifies the influence of factors controlling the rates and patterns of groundwater flow in mountainous terrain. As a consequence, these factors also amplify the influence of groundwater flow on thermal regimes in mountains. In this chapter, the influence of these factors is examined using the numerical method outlined in Chapter 2. This method differs from those used by previous workers (Smith and Chapman, 1983, 1985; Garven and Freeze, 1984) in the way that the upper boundary condition for fluid flow is described. Previous workers assume that the upper boundary of the flow domain coincides with the water table, even in cases where the water table lies below the bedrock surface. As a consequence, hydraulic head is specified everywhere on the upper boundary and the processes of fluid flow and heat transfer acting in the unsaturated zone are ignored. The free-surface approach used in this study avoids

making assumptions regarding the water table configuration and includes a simplified representation of fluid flow and heat transfer in the unsaturated zone. In this way, temperatures at the water table are not specified but rather, they are calculated in the solution procedure.

In this chapter, idealized mountain thermal regimes are modeled for a range of conditions representative of the Western Cordillera in North America. Factors to be considered are surface topography, geology, climate, and regional heat flow. Elements of surface topography include slope profile, relief and three-dimensional form. Both planar and axisymmetric mountain forms are considered. The geologic environment controls spatial variability of permeability, porosity, and thermal conductivity. Climatic factors influence available infiltration, the presence and extent of alpine glaciers, and surface temperature conditions. Regional heat flow is a characteristic of the tectonic environment within which the mountain is located. It is of particular interest to examine the influence of these factors on: (1) the nature and magnitude of advective disturbance of conductive thermal regimes, (2) the interaction of free- and forced-convection within the mountain massif, (3) heat transfer within fracture zones, and (4) the nature of thermal springs. Table 4.1 summarizes the simulations carried out to assess the influence of each factor and provides a guide to the figures that illustrate each effect.

4.2 SIMULATION PARAMETERS

Simulations are performed by assigning a set of fluid flow and thermal parameters (Table 4.2) within a geometry similar to that of Figure 2.1. The importance of surface topography is illustrated by considering two extremes in slope profile; one convex and one concave (Figure 4.1). Convex profiles are typical of glaciated crystalline terrain while concave profiles are often found in folded mountain belts and at volcanic cones. Parameter values given in Table 4.2, and the range of values tested in the numerical experiments, are chosen to reflect conditions typical of mountainous terrain.

Mean annual precipitation is the basic determinant of available infiltration rates. In Chapter 3, it is shown that 2×10^{-8} m/sec defines a reasonable upper limit for available infiltration rates while a minimum I_z of 10^{-12} m/sec is assumed to occur in all but the most arid of climates. Although rock permeabilities can range from less than 10^{-19} m^2 to in excess of 10^{-9} m^2, the bulk permeability of mountainous terrain considered in this study is assumed to be less than 10^{-14} m^2. Freeze and Cherry (1979) and Neuzil (1986) suggest that this is a reasonable upper limit for moderately fractured crystalline and argillaceous rocks. In all simulations, a basal low-permeability unit ($k_b = 10^{-22}$ m^2) occupies the lower 2 km of the domain to provide a region of conduction-dominated heat transfer

(Figure 4.1). This region is sufficiently thick that the majority of simulation results show isotherms near the basal boundary to be sub-parallel to the boundary. As a consequence, the vertical conductive heat flux applied at the basal boundary is transferred in a consistent manner to the thermal regime. The remainder of the domain contains a higher-permeability unit where advective heat transfer may dominate.

In most simulations, both upper and lower zones have homogeneous and isotropic permeability (k_u, k_b) and uniform porosity (n_u, n_b). Although thermal conductivity of the solid matrix (λ^s) is uniform throughout the system, varying porosity and saturation produce contrasts in thermal conductivity of the solid-fluid composite (λ^e). Because we consider the steady state problem, porosity only has an indirect influence on the flow system through its impact on thermal conductivity of the solid-fluid composite. A basal heat flux (H_b) is applied on the horizontal base of the system while surface temperature conditions are defined in terms of a reference surface temperature (T_r) and a thermal lapse rate (G_l). Longitudinal and transverse thermal dispersivities (a_l, a_t) are uniform throughout the system and are held constant for all simulations.

In the following sections, frequent reference is made to an advectively-disturbed reference case simulated using the parameters listed in Table 4.2. Results for the

reference case, shown in Figure 4.1c, are used as a standard for comparison with subsequent simulation results. The reference I_z of 2×10^{-9} m/sec (Table 4.2) is selected to represent the maximum rate of infiltration that might be available in a climate transitional between semi-arid and humid. The reference upper unit permeability (k_u) of 10^{-15} m^2 represents relatively permeable conditions that might reasonably be expected in mountainous terrain. The reference heat flux (H_b) of 60 mW/m^2 is representative of a normal conductive regional heat flux. Thermal conductivity (λ^s) is fixed at 2.5 mW/m^2, a value that approaches the lower limit for rocks found in mountainous terrain. Barry (1981) suggests that atmospheric thermal lapse rates may vary from less than 2 K/km to greater than 8 K/km. In this study, temperatures at the bedrock surface are defined using a median lapse rate (G_l) of 5 K/km (Table 4.2) and a valley reference temperature (T_r) of 10 °C.

4.3 RESULTS OF NUMERICAL SIMULATIONS

4.2.1 Patterns of Advective Thermal Disturbance

It is recognized that the patterns and magnitude of groundwater flow dictate the character of an advective thermal disturbance. Numerical results described in Chapter 3 indicate that high-relief mountainous terrain amplifies the impact of factors that exert dominant control over groundwater flow systems; geology, climate and surface

topography. In this section, the influence of these factors on the character of advective thermal disturbance is illustrated by examining the patterns of groundwater flow and heat transfer in idealized mountainous terrain.

Patterns of groundwater flow are depicted in Figure 4.1 by pathlines (dotted lines) representing the track of a fluid particle entering the flow system at a specified point on the bedrock surface. Pathline spacing is inversely proportional to the flux of fluid (specific discharge) through flowtubes bounded by each pair of pathlines. Recall that pathlines should not be confused with the streamlines generated from contour plots of a suitably defined stream function or velocity potential. The magnitude of I_z provides a convenient reference for comparing the variation of fluid flux. For example, pathline spacing in Figures 4.1c and 4.1e varies in response to the fact that fluid flux in the convex domain increases approximately fivefold from a value of 2×10^{-9} m/sec at the free-surface to about 10^{-8} m/sec at the discharge area. Fluid flux is more uniform in the concave domain (Figure 4.1g), decreasing from 2×10^{-9} m/sec at the free-surface to about 1.6×10^{-9} m/sec.

Patterns of heat transfer are shown in Figure 4.1 by heatlines (thick dashed lines) while subsurface temperatures are represented by isotherms (solid lines). Kimura and Bejan (1983) suggest the use of heatlines as a means of mapping the transfer of thermal energy from the basal boundary by

conduction and advection. As a consequence, each heatline shown in Figure 4.1 is locally parallel to the direction of net energy flow. In addition, the net energy flow across each heatline is zero. Note that this yields heatlines normal to the isotherms only in regions where advective heat transfer by groundwater flow is negligible, or where the direction of fluid flow is normal to the isotherms. Heatlines are everywhere normal to isotherms in the conduction-dominated thermal regimes shown in Figures 4.1a, 4.1d and 4.1f.

Heatlines and isotherms shown in Figure 4.1 illustrate the increasing influence of advective heat transfer on conductive thermal regimes as rock permeability is increased three orders of magnitude. In each case, the available infiltration rate is fixed at the reference value (I_z = 2×10^{-9} m/sec). Three series of simulation results are shown; the convex domain with normal heat flow (Figures 4.1a to 4.1c), the convex domain with doubled heat flow (Figures 4.1d and 4.1e) and the concave domain with normal heat flow (Figures 4.1f and 4.1g). Conductive temperature fields, obtained for k_u equal to 10^{-18} m^2, are shown in the lefthand panel of each series (Figures 4.1a, 4.1d and 4.1f). A weak advective disturbance, characterized by heatlines at an oblique angle to the isotherms, is found when k_u is 10^{-16} m^2 (Figure 4.1b). A strong disturbance, shown in the righthand panel of each series, is found when k_u exceeds about 10^{-15} m^2 (Figures 4.1c, 4.1e and 4.1g). In each case, the strong

disturbance is characterized by heatlines subparallel to isotherms in the upper permeable unit.

Shaded areas shown in Figures 4.1c, 4.1e and 4.1g indicate areas little affected by thermal energy originating at the basal boundary. Temperatures within these regions reflect the temperature of groundwater recharge defined at the upper boundary using a thermal lapse rate. Elsewhere, heatline patterns indicate that the entire basal heat flow is absorbed by the circulating groundwater and deflected to exit in the discharge area. The basal heat flow is effectively masked by downward flowing groundwater within the shaded regions.

The transition from conduction-dominated to advection-dominated thermal regimes is accompanied by little change in patterns of groundwater flow within each simulation series. Patterns of fluid flow differ somewhat between the high- and low-permeability cases in each series because lower water table elevations increase the thickness of the unsaturated zone where only vertical fluid flow is assumed. Patterns of fluid flow are also little affected by changes in basal heat flow. Doubling the basal heat flow applied to the convex domain, from 60 to 120 mW/m^2, causes an approximate doubling of temperatures in conduction-dominated and fluid-upflow regions of each domain (compare Figures 4.1a and 4.1c to 4.1d and 4.1e). Warmer temperatures cause reduced fluid viscosity and fluid

density, a small increase in fluid flux (about 10 percent, on average), and reduced water table elevation. These changes have little effect on patterns of fluid flow and heat transfer. The pattern of the thermal disturbance found for the concave slope profile (Figure 4.1g) differs from that of the equivalent convex case (Figure 4.1c) because surface topography has a pervasive influence on the pattern of groundwater flow.

4.3.2 Magnitude of Advective Thermal Disturbance

The magnitude of an advective thermal disturbance is characterized by the degree that conductive thermal regimes are cooled, or heated, by groundwater circulation. Contour plots of temperature residuals quantify the magnitude and spatial variation of cooling and heating. Temperature residuals are calculated by subtracting temperatures obtained for a given simulation from those of the corresponding conductive case, at each node in the finite element mesh. For example, Figure 4.2a is derived by subtracting results shown in Figures 4.1b from those shown in Figure 4.1a while Figure 4.2c is derived using results shown in Figures 4.1d and 4.1e. Values of temperature residual equal zero along the upper boundary because the same boundary conditions are applied in each case. Temperature fields are affected only slightly by a transition in thermal conductivity at the water table. This effect is included in the computation of temperature

residual by using the same water table configuration in each pair of simulations. Figures 4.2a through 4.2d illustrate the contour plots of temperature residual obtained for the advectively disturbed thermal regimes shown in Figures 4.1b, 4.1c, 4.1e and 4.1g, respectively. In each case, advective heat transfer cools most of the thermal regime and heats only small regions near the valley floor. Maximum cooling is found beneath the mountain summit within, or near, the basal low-permeability unit. The degree of advective cooling is controlled by upper zone permeability, infiltration rate, slope profile and basal heat flow.

In this study, a steady uniform heat flux (rather than a fixed temperature) is specified at the basal boundary. This allows cooling, caused by advective heat transfer in the upper permeable zone, to propagate to the base of each system by conduction within the basal low-permeability unit. If temperatures were specified on the basal boundary, temperature residuals on the boundary would equal zero and maximum cooling would be found in central regions of the domain. Modeling realistic systems using this approach would require a knowledge of temperatures at depths of several kilometers. In cases where deep temperature data are unavailable, it seems more appropriate to adopt the approach used here in defining the basal boundary condition using estimates of regional heat flow.

Figures 4.2a and 4.2b illustrate the increased cooling that occurs when k_u is increased tenfold from 10^{-16} m^2 to 10^{-15} m^2. Increased groundwater flux absorbs thermal energy supplied at the basal boundary with less heating of the domain. As a consequence, reduced values of temperature residual are found within a smaller region of heating in the higher-permeability case. Similar results are obtained, but not shown, when groundwater flux is reduced by decreasing I_z one order of magnitude to 2×10^{-10} m/sec. In this latter case, the maximum elevation of the water table is only 40 meters above the valley floor.

Temperature residuals shown in Figure 4.2c for the doubled heat flow case (H_b = 120 mW/m^2, shown in Figure 4.1e) are calculated with respect to a conductive temperature field with doubled heat flow, similar to that of Figure 4.1d. Temperatures in both doubled and normal heat flow cases are similar in regions of fluid downflow (shaded regions of Figures 4.1c and 4.1e). This similarity evolves because circulating groundwater has the capacity to absorb all the thermal energy applied at the base of the system, even in the doubled heat flow case, with little change in temperature within upper regions of the domain. Comparing Figures 4.2b and 4.2c illustrates the increased cooling present in the doubled heat flow case. Given these results, it appears impossible to identify the magnitude of the basal heat flow using temperature data collected in shallow boreholes located at elevations above the valley floor when

k_u exceeds about 10^{-15} m^2.

Comparing temperature residuals in Figure 4.2d with those of Figure 4.2b highlight the greater cooling that occurs in the domain with convex slope profile. Although fluid flux is similar in both convex and concave domains (the same I_z is applied at the free-surface), the longer free-surface segment of the convex domain yields a total flow of groundwater about twice that of the concave domain. This provides a greater volume of fluid to absorb the basal heat flux, leads to greater cooling throughout the convex domain, and produces a smaller region of heating.

At first glance, the large disparity in the size of regions of heating and cooling shown in Figure 4.2 might be attributed to the elevation-dependent decrease in temperature imposed on the upper boundary through the thermal lapse rate. The influence of the thermal lapse rate is examined by simulating a convex domain with the reference conditions modified to maintain a constant surface temperature of 10 °C. Warmer groundwater recharge reduces the degree of advective cooling by about 10 °C but has only a small influence on the patterns of temperature residual and the size of regions of cooling and heating. Regions of cooling predominate in the maps of temperature residual because the basal heat flow is readily absorbed, with little heating, by the relatively large flux of fluid through each system. Temperature residuals calculated for a number of

simulations indicate that maximum heating is found, for a specified H_b and topographic relief of 2 km over 6 km, in systems with a bulk permeability of about 10^{-16} m^2 (Figure 4.2a). Reducing groundwater flux by reducing topographic relief, or permeability, produces larger regions of heating and reduced values of temperature residual. Regions of heating and cooling are approximately equal when a weak thermal disturbance is predicted (k_u between 10^{-18} m^2 and 10^{-17} m^2). Regions of heating extend over at least 50 percent of the lower-relief domains considered by Smith and Chapman (1983, 1985) and Garven and Freeze (1984) when a weak disturbance is predicted.

4.3.3 Influence of Water Table Configuration

The previous discussion indicates that water table configurations have little influence on the pattern and magnitude of advective thermal disturbance. Results shown in Figure 4.3 highlight the strong contrast in thermal regimes that can develop under conditions where matching water table configurations are predicted. Matching water table configurations and patterns of groundwater flow are obtained when the ratio I_z/k_u is constant. In Figure 4.3 I_z/k_u equals $4\text{x}10^5$ sec^{-1}m^{-1}. The significance of this ratio is discussed in detail in Chapter 3. Figure 4.3a is obtained by setting k_u equal to $5\text{x}10^{-15}$ m^2 and I_z to $2\text{x}10^{-9}$ m/sec. Reducing the value of I_z by a factor of five to $4\text{x}10^{-10}$ m/sec (k_u is also reduced by a factor of five to 10^{-15} m^2), causes a fivefold

decrease in groundwater flux. This reduced fluid flux creates a weaker thermal disturbance and a warmer thermal regime than that found for the higher-infiltration case of Figure 4.3a. Unique values of fluid flux cannot be associated with a particular water table configuration, therefore, the position of the water table provides little direct insight into the magnitude of an advective thermal disturbance.

Although water table configurations have little direct influence on advective thermal disturbance, they provide insight into the parameters that do exert dominant control over groundwater flux and advective heat transfer; permeability and infiltration rate. Simulation results described in Chapter 3 indicate that groundwater flux increases almost linearly with increasing k_u, in cases with matching water table configurations. When the water table lies below the bedrock surface, fluid flux at the free-surface equals the available infiltration rate and an approximate linear relationship can be assumed between I_z and k_u. The minimum value of I_z/k_u required for the water table to coincide with the bedrock surface of the convex domain defines the solid diagonal line shown in Figure 4.4. This line is termed the water table threshold and is a characteristic of a specified domain geometry. Points plotting below the water table threshold shown in Figure 4.4 indicate infiltration and permeability conditions that yield predicted water table elevations below the bedrock surface.

Under such conditions, groundwater flux within the domain can be characterized by I_z. Values of I_z and k_u plotting above the water table threshold indicate when the water table coincides with the bedrock surface. Under these conditions, groundwater flux for the specified domain can be characterized by k_u because I_z is unlikely to bear a direct relationship to groundwater flux within the domain. Triangles shown in Figure 4.4 are labelled to indicate the combinations of I_z and k_u used to obtain the results illustrated in Figures 4.1 and 4.3. The dashed line joining points labelled 4.3a and 4.3b in Figure 4.4 indicates that the approximate linear relationship between I_z and k_u also produces matching water table configurations that need not coincide with the bedrock surface. In this case, the maximum water table elevation is 460 m (Figures 4.3a and 4.3b).

Increasing the basal heat flow, or simulating a concave slope profile, produces water table elevations lower than those predicted by the reference convex case (compare Figures 4.1e and 4.1g to Figure 4.1c). Therefore, greater infiltration rates are required to maintain water table elevations everywhere at the bedrock surface. As a consequence, water table thresholds for the concave and doubled heat flow cases, are shifted to the left of that found for the reference convex case (Figure 4.4). The hydrologic implications of Figure 4.4 provide the basis for deriving insights into the onset of advective thermal disturbance discussed in the following section.

4.3.4 Onset of Advective Thermal Disturbance

Previous workers have defined the advective threshold in a variety of ways; Norton and Knight (1977) use a threshold fluid mass flux, Smith and Chapman (1983) use a threshold permeability, while Domenico and Palciauskas (1973) and van der Kamp (1982) use a threshold value of a Peclet number that expresses the ratio between heat transfer by advection and conduction. In this study, advective thresholds are defined on the basis of permeability and fluid flux.

Simulation results presented by Norton and Knight (1977), by Smith and Chapman (1983), and in this study indicate that conductive thermal regimes develop when fluid flux is less than a threshold of about 10^{-11} m/sec. When the water table lies below the bedrock surface, this threshold fluid flux can be characterized by I_z because applying values of available infiltration rate in excess of 10^{-11} m/sec causes a significant disturbance of conduction-dominated thermal regimes (shaded region in Figure 4.4). When the water table coincides with the bedrock surface, the threshold fluid flux must be defined on the basis of a threshold k_u. This value is estimated from Figure 4.4 as the value of k_u required to produce a water table coincident with the bedrock surface when I_z equals about 10^{-11} m/sec. A k_u of 4×10^{-18} m^2 provides the threshold fluid flux for the convex case with normal heat flow and marks the

upper limit of conduction-dominated heat transfer (shaded region in Figure 4.4). Results obtained by Smith and Chapman (1983) indicate a greater advective threshold for their low-relief terrain of 1 km over 40 km. The dotted line shown in Figure 4.4 represents the water table threshold estimated from their unpublished results and indicates a permeability-controlled threshold of about 3×10^{-17} m^2. Because lower hydraulic gradients develop in regions with reduced topographic relief, greater permeability is required to provide the minimum groundwater flux for significant advective heat transfer. This dependence on topographic relief means that estimated permeability-controlled thresholds are only valid for a specified domain geometry. The close proximity of the water table thresholds shown on Figure 4.4 suggest that water table thresholds for the mountain-scale relief considered here are little affected by changes in basal heat flow and slope profile. As a consequence, the threshold permeability used to define the onset of an advective disturbance varies less than half an order of magnitude in response to variations in slope profile or basal heat flow (Figure 4.4).

The numerical results described above suggest that a knowledge of available infiltration rate, or permeability, cannot be used in isolation to determine the onset and magnitude of advective thermal disturbance. Knowing the approximate position of the water table will aid in establishing the parameter that provides greatest insight

into the magnitude of groundwater flux and the magnitude of the thermal disturbance. Consider the plot of I_z against k_u shown in Figure 4.4. If the threshold I_z is applied in high-permeability terrain, groundwater recharge is minimal and the water table lies deep below the bedrock surface. Because the corresponding groundwater flux is small, the advective thermal disturbance is negligible. Thermal disturbance is also negligible in low-permeability terrain, despite a higher water table elevation. As I_z is increased above its advective threshold, the water table is found at higher elevations within the system and groundwater flux increases to cause greater thermal disturbance. An upper limit for the magnitude of the disturbance is obtained, for a specified value of k_u, when I_z plots at or above the appropriate water table threshold (Figure 4.4). This limit occurs because the water table coincides with the bedrock surface and further increase in I_z has no effect on the groundwater flow system. In such cases, the magnitude of the advective disturbance is characterized by the bulk permeability of the mountain massif.

Figure 4.4 provides insight into the conditions where advective thermal disturbance is unlikely. Maximum groundwater flux can be expected in high-relief terrain of high permeability with elevated regional heat flow and humid climate. Values chosen in this study approach the upper limit for topographic relief (2 km over 6 km) and basal heat flow (120 mW/m^2). These conditions promote maximum rates of

groundwater flow and suggest that a minimum permeability, below which advective disturbance of regional-scale thermal regimes is unlikely, is about 10^{-18} m^2. This lower limit is little affected by variations in slope profile and basal heat flow. As topographic relief is reduced, however, the lower limit for advective disturbance is found at greater values of permeability.

4.3.5 Free-Convection in Mountainous Terrain

Elder (1967) describes a numerical experiment designed to examine the influence of external fluid flow on patterns of free-convection within a permeable rectangular slab heated from below. In modeling this system, he showed that external fluid flows imposed on the upper and vertical boundaries of the slab could obliterate the free-convection cells that would otherwise develop. Figure 4.5 illustrates the results of a similar experiment, performed as part of this study, where the nature of the external fluid flow is explicitly defined by the character of the regional groundwater flow system.

Figure 4.5a illustrates the thermal regime and patterns of fluid flow associated with development of free-convection cells in mountainous terrain, given the geologic conditions shown in Figure 4.5d. A thin low-permeability horizon (100 m thick with permeability k_l) separates two permeable units; an upper unit with k_u equal to 10^{-15} m^2 and a lower unit (equivalent to Elder's permeable slab) with

k_l equal to 5×10^{-15} m^2. Pathlines shown in the righthand panel of Figure 4.5a depict two free-convection cells that develop in the lower permeable unit when a basal heat flow of 120 mW/m^2 is applied and the upper and lower units are isolated by setting k_l to 10^{-19} m^2. Upwarped isotherms and convergent heatlines shown in Figure 4.5a highlight the region of upwelling fluid in the free-convection cells. Heatlines pass through the low-permeability horizon to be swept in the direction of topographically-driven flow in the upper permeable zone. Therefore, the basal heat flux has little influence on temperatures directly beneath the mountain summit (shaded region of Figure 4.5a).

The rectangular geometry of the lower permeable layer allows calculation of a Rayleigh number Ra to confirm that free-convection should be expected under the conditions stipulated. Ra for the system shown in Figure 4.5a is calculated using the definition of Cheng (1978) and the parameter values shown below;

$$Ra = \frac{\rho^2 g \beta C_f k_l H \Delta T}{\mu \lambda^e} \qquad (4.1)$$

where

g = gravitational constant = 9.8 m/sec^2

μ = dynamic viscosity of water (70°C) = 4×10^{-4} Pa·s

ρ = density of water (70°C) = 978 kg/m^3

C_f = specific heat capacity of water = 4186 J/kgK

H = thickness of lower permeable unit = 1800 m

ΔT = vertical temperature difference = 90 K

k_l = permeability = 5×10^{-15} m^2

β = thermal expansivity of water = 5×10^{-4} K^{-1}

λ^e = thermal conductivity of solid-fluid composite = 2.3 W/mK

The resulting value of Ra is 173. Because this value exceeds the generally accepted threshold of 40 (Cheng, 1978), it is reasonable that the numerical model should predict the weak cellular free-convection indicated within the lower permeable unit (Figure 4.5a).

Increasing the permeability of the intervening unit k_i to 10^{-17} m^2 increases groundwater flux between the upper and lower permeable units and increases the total flow through the system. Increased lateral flow in the lower permeable unit displaces the region of upwelling to the right, increases cooling beneath the mountain summit and causes warmer temperatures beneath the valley floor (Figure 4.5b). Further increasing k_i to 10^{-16} m^2 completely obliterates the free-convection cells to produce a strongly disturbed thermal regime and patterns of groundwater flow similar to those of Figure 4.1g. Under the conditions simulated here, free-convection cells are easily disturbed by topographically-driven fluid flow because groundwater flux in the permeable upper unit is about 150 times greater than the buoyancy-driven fluid flux of the lower permeable unit.

Clearly, free-convection cells are less likely to be disturbed as the permeability of the upper unit is reduced or as topographic relief is reduced.

Increasing k_l by one order of magnitude to 5×10^{-14} m^2 causes more vigorous free-convection within the lower permeable layer (Figure 4.5c) and produces fluid flux similar in magnitude to that of the upper permeable layer (approximately 10^{-9} m/sec). Using equation (4.1) and the updated parameters shown below, Ra for this system is 524.

μ = dynamic viscosity of water (45°C) = 6×10^{-4} Pa·s

ρ = density of water (45°C) = 990 kg/m^3

ΔT = vertical temperature difference = 40 K

k_l = permeability = 5×10^{-14} m^2

Total flow of fluid through the system and the pattern of fluid flow is little changed from that of Figure 4.5a. Increased buoyancy-driven fluid flux in the lower permeable layer decreases the likelihood that free-convection cells will be displaced, or obliterated, as the permeability of the intervening horizon is increased. Enhanced rates of buoyancy-driven fluid flow focus transfer of the basal heat flow within the region of fluid upwelling. This yields significant cooling throughout the lower permeable layer, except at the top of the region of upwelling (Figure 4.5c). Here, temperatures are similar to those of the weakly convecting case (Figure 4.5a). Temperatures in the upper

permeable unit differ little from those found in the weakly convecting case, except in the vicinity of the valley floor. As a consequence, the character of the thermal regime within the lower permeable unit is unlikely to be detected using thermal data collected in shallow boreholes. Additional work is underway to examine the interplay of free-convection cells and topographically-driven fluid flow within more complex regional flow systems where igneous intrusions and permeable fracture zones may be encountered. This work is expected to yield useful insights regarding thermal regimes at active volcanic centers and the origin of epithermal ore deposits.

4.3.6 Influence of Mountain Topography

Surface topography has a pervasive influence on the pattern and magnitude of groundwater flow in mountainous terrain, hence on the pattern of advective heat transfer. The influence of slope profile on groundwater flow systems and thermal regimes has been described in previous sections. In the following paragraphs, the implications of topographic symmetry and three-dimensional form are addressed.

Asymmetry in surface topography produces an advective thermal disturbance that reflects the influence of asymmetry in patterns of groundwater flow. Three mountain valleys are shown in Figure 4.6, each with a convex slope profile on the left and a linear slope profile on the right. Mirror symmetry is assumed at the vertical boundaries in each case.

Figure 4.6a shows an asymmetric valley with opposing summits of equal elevation. Figure 4.6b shows an asymmetric valley with the elevation of the righthand summit reduced to one-half that of the lefthand summit. Figure 4.6c represents a symmetric system with a convex ridge adjacent to a wide valley with flat topography. The strongly disturbed thermal regimes shown in Figure 4.6 are obtained by assigning the reference conditions given in Table 4.2.

Asymmetry in surface topography can cause a strong warping of isotherms near the valley floor (Figures 4.6a and 4.6b) that might be mistaken for the thermal signature of a free-convection cell or a permeable fracture zone; both features can cause upflow of heated fluid. The pronounced warping of isotherms is centered on groundwater flow divides located within regions of closely spaced sub-vertical heatlines. Groundwater flow divides represent imaginary boundaries separating the distinct regions of groundwater upflow associated with each slope profile. The position of the divide reflects a balance between the total flow of groundwater beneath each slope profile. In an ideal symmetric case, the divide is vertical and located at the valley floor. This is the case in Figure 4.6c and the previous Figures 4.1 and 4.4. Total flow through the linear slope profile is about 60 percent of that of the convex profile, therefore, both the groundwater divide and the region of upwarped isotherms are displaced to the right in Figure 4.6a. As relief of the linear slope is reduced, fluid

flow through the linear slope is reduced. Both the divide and the upwarping of isotherms are displaced further to the right in Figure 4.6b.

Figures 4.6a and 4.6b indicate that the groundwater flow divide may intersect the bedrock surface upslope of the valley floor in regions of asymmetric surface topography. As a consequence, chemical and thermal signatures of a subsurface heat source located beneath the lefthand convex slope may be expressed in springs discharging upslope from the valley floor on the opposing linear slope. In addition, samples collected at the valley floor may provide little information regarding conditions beneath the linear slope profile. As permeability is reduced, the warping of isotherms becomes less pronounced. The position of the groundwater flow divide, however, is unchanged.

In the preceding discussion, each domain represents a vertical section through a linear ridge of infinite extent. Although fully three-dimensional systems cannot be simulated with the current model, insights into the influence of other topographic forms can be gained by simulating axisymmetric conical features. The radial equivalent of the planar domain shown in Figure 4.6c is an isolated mountain massif with convex slope profile and axis of symmetry beneath the ridgetop. Because the horizontal component of fluid flux decreases with increasing radial distance, fluid flux in the radial case decreases from the reference value of I_z with

increasing radial distance. This transition is reflected in the plot of fluid mass flux normal to the upper boundary of each system shown in Figure 4.7a. I_z is the same in each case, therefore, fluid mass flux is the same along each free-surface. Elsewhere, fluid discharge in the radial case is less than that of the planar case. This difference is most readily seen near the break-in-slope, where most discharge occurs. The fluid flux profile shown in Figure 4.7a indicates that only a small percentage of the total flow discharges near the righthand boundary. This suggests that, a flat valley floor with a width in excess of about two times the horizontal distance covered by the adjacent mountain slope will effectively isolate groundwater flow systems and thermal regimes on opposing sides of the valley. For example, Figure 4.7 shows a valley half-width of 6 km (for a total width of 12 km) and a horizontal slope length of 6 km.

Despite the contrast in topographic symmetry, temperatures in the radial case are only slightly warmer than those of the planar case. The difference in temperature obtained in each case is shown in the contour plot of Figure 4.7b. The greatest temperature difference occurs in central regions of the system, beneath the break-in-slope, where greatest contrast in groundwater flux is encountered (Figure 4.7a). In this region, temperatures in the radial system are elevated about 8 °C above those of the planar system. Little difference between the planar and radial cases is indicated

near the right and left boundaries of the system because the contrast between the patterns and magnitude of groundwater flow in each case is minimal.

4.3.7 Permeable Fracture Zones and Thermal Springs

The numerical method used in this study allows permeable fracture zones to be embedded, as discrete entities, within the surrounding rock mass. In contrast to previous approaches (Lowell, 1975; Sorey, 1978; Kilty *et al.*, 1979; Goyal and Kassoy, 1980; Bodvarsson *et al.*,1982), fluid flux within the fracture is dictated by conditions controlling the regional flow system rather than by a specified fluid source at depth or by a specified uniform fluid flux in the fracture zone. An important difference lies in the fact that this approach allows fluid to enter, or leave, the fracture zone at any point along its length. Previous studies often assume that the fracture wall is impervious.

In this modeling study, fracture zones are represented by a series of connected planar segments with uniform thickness (b) and a homogeneous equivalent porous media permeability (k_f). Because an approximate linear relationship exists between permeability and fluid flux, various combinations of b and k_f produce the same patterns of groundwater flow in systems with matching water table configurations and matching $k_f \cdot b$; when b is less than about 100 m. The product

$k_f \cdot b$ (expressed in units of $m^2 \cdot m$) is termed the transmissivity of the fracture zone and is used in discussing the simulation results. Note that this definition of transmissivity differs from the product of hydraulic conductivity times thickness usually adopted in isothermal approaches. Figures 4.8a and 4.8b include a steeply dipping fracture zone, extending from the valley floor to the basal boundary. Fracture width b and permeability k_f are assumed constant everywhere along the fracture zone. The transmissivity of the fracture zone $k_f \cdot b$ is assumed to equal $10^4 \cdot k_u$ ($m^2 \cdot m$) and might reasonably correspond to several combinations of b and k_f; b of 1 m and k_f of $10^4 \cdot k_u$, b of 10 m and k_f of $10^3 \cdot k_u$, or b of 100 m and k_f of $10^2 \cdot k_u$.

Figure 4.8a illustrates the influence of the fracture zone described above, with k_u of 10^{-15} m^2, on groundwater flow and heat transfer within the asymmetric topography of Figure 4.6a. The total flow of groundwater increases by 75 percent to yield cooler temperatures everywhere in the domain. Patterns of fluid flow and heat transfer are greatly modified because eighty percent of the total fluid flow, and the entire basal heat flow, is captured by the fracture zone. Rapid fluid flow in the fracture zone, and the surrounding rock mass, yields almost isothermal conditions along the fracture and a spring temperature elevated only 3 °C above the ambient surface temperature of 10 °C. Temperatures are everywhere cooled below those of the corresponding conduction-dominated case and the basal heat

flow is effectively masked everywhere along the upper boundary (shaded region in Figure 4.8a).

Within the low-permeability basal unit, fluid flux in the fracture zone is 6 orders of magnitude less than that of shallower fracture segments because inflow from the basal unit is minimal. As a consequence, the conductive pattern of heat flow within the basal unit is undisturbed. Above the basal unit, inflow from the surrounding rock mass causes fluid flux in the fracture zone to increase almost linearly (about one order of magnitude); reaching a maximum at the bedrock surface.

Decreasing the permeability of the surrounding rock mass to 10^{-16} m^2, while retaining the transmissivity of the fracture zone at $10^4 \cdot k_u$ ($m^2 \cdot m$), reduces fluid flux in both the fracture zone and the surrounding rock mass. This effect, in turn, yields a a warmer thermal regime (Figure 4.8b) and a spring temperature 13 °C warmer than that of the higher-permeability case. The pattern of upwarped isotherms shown in Figure 4.8b differs considerably from those of Kilty *et al.* (1979) and Sorey (1978), who predict high temperature gradients at shallow depths in the fracture zone. This difference is attributed to the fact that previous workers assume an impervious fracture boundary and a uniform fluid flux within the fracture zone. In this study, the ability for fluid to enter, or leave, the fracture zone allows a non-uniform pattern of fluid flux to

develop. Fluid flux in the fracture zone increases about one order of magnitude between an depth of 2 km and the valley floor in the system shown in Figure 4.8. As a consequence, a more uniform temperature gradient develops along the fracture zone.

A conduction-dominated thermal regime is found when k_u equals about 10^{-18} m^2. This result is independant of the magnitude of the transmissivity of the fracture $k_f \cdot b$ because the fluid flux in the flow system is dominated by the permeability of the surrounding rock mass. Although rates of fluid flow are insufficient to cause a perceptible change in the temperature field, the volume of fluid flow in the fracture zone is sufficient to cause a spring temperature elevated 5 °C above the ambient of 10 °C.

Figure 4.9 illustrates the variation of spring temperature as a function of upper unit permeability (k_u), for both the normal and doubled heat flow cases. Peaks in spring temperature (25 °C for H_b equal to 60 mW/m^2 and 43 °C for H_b equal to 120 mW/m^2) are found when rock mass permeability equals about 10^{-16} m^2. This value of k_u also produces maximum advective heating in the unfractured convex slope profile (compare temperature residuals shown in Figures 4.2a, 4.2b and 4.2c). This behaviour reflects the fact that the overall character of the thermal regime is controlled by regional groundwater flow through the rock mass. Temperature residuals shown in Figure 4.2a indicate

that a region of heating develops near the valley floor that contributes to development of a thermal spring. Increasing k_u above 10^{-16} m^2 causes reduced spring temperatures (Figure 4.9) because the rapidly circulating groundwater absorbs all thermal energy applied at the base of the system with little increase in temperature. Decreasing k_u below 10^{-16} m^2 also causes reduced spring temperatures (Figure 4.9) because fluid flow to the fracture is reduced and a greater portion of the basal heat flow is transferred by conduction through the surrounding rock mass.

Changing the effective length of the fracture zone modifies its influence on the thermal regime. The effective length is increased by considering the influence of permeable cross-fractures that intersect the original fracture zone. The resultant increase in fluid flux throughout the domain causes a greater portion of the basal heat flow to be captured by the fracture zone. As a consequence, spring temperatures are warmer and recharge areas are cooler. For example, the length of the fracture zone shown in Figure 4.8b is increased by introducing a second fracture zone, 2 km in length, beneath the convex slope (within the upper permeable unit) to intersect the original fracture at right angles where both fractures meet the top of the basal unit. This increased length yields a greater spring temperature of 76 °C. Reducing the length of the fracture zone to 1 km causes only a slight reduction in spring temperature because eliminating inflow from deeper

regions of the upper permeable unit has only a small effect on fluid flux in the fracture zone.

The transmissivity of the fracture zone $k_f \cdot b$ dictates the degree of disturbance caused by the fracture zone. In the system shown in Figure 4.8b, the fracture zone exerts its maximum influence when $k_f \cdot b$ equals about $10^4 \cdot k_u$ ($m^2 \cdot m$). Increasing $k_f \cdot b$ to $10^5 \cdot k_u$ ($m^2 \cdot m$) has little effect on the regional flow system and causes only a 1 °C increase in spring temperature (open circle plotted in Figure 4.9). Reducing $k_f \cdot b$ to $10^3 \cdot k_u$ ($m^2 \cdot m$) has a greater influence, causing a 7 °C decrease in spring temperature (Figure 4.9). The fracture zone restricts fluid flow in the surrounding rock mass when $k_f \cdot b$ is less than $10^4 \cdot k_u$ ($m^2 \cdot m$). At values of $k_f \cdot b$ in excess of this value, fluid flux in the system is restricted only by the permeability of the surrounding rock mass.

The results shown in Figures 4.8 and 4.9 are representative only of the idealized geometries and conditions tested. These results should only be used as a guide to the character of thermal regimes influenced by permeable fracture zones because patterns of thermal disturbance and spring temperatures are strongly controlled by a variety of factors that are difficult to map and quantify. These factors include; fracture position, orientation, transmissivity of the fracture zone, length, and intersection with other fractures. In addition, the

three-dimensional nature of intersecting fracture zones and rugged mountainous terrain makes detailed extrapolation from two-dimensional simulations difficult. Figure 4.9 suggests, however, that an optimal range of bulk permeability exists (k_u = 10^{-17} m^2 to 10^{-15} m^2) wherein maximum spring temperatures are most probable. It should be noted that localized shallow heat sources, not considered in this study, could promote the development of high-temperature springs even when k_u lies outside this range. Results presented in this section suggest that it will be difficult to predict accurately the temperature of thermal springs in any but the simplest of cases.

4.4 IMPLICATIONS FOR HEAT FLOW STUDIES

Estimates of regional heat flow are often made by measuring vertical temperature gradients in shallow boreholes (less than 200 m deep), correcting the results for the influence of surface topography and calculating the regional heat flow using estimates of thermal conductivity (Sass *et al.*, 1971). In mountainous terrain, an additional correction may be required to account for advective disturbance of the thermal regime. Contour plots of temperature gradient ratio provide insight into the magnitude and spatial variation of errors in temperature gradient introduced by advective heat transfer. This method of presentation should be of particular interest to those attempting to interpret temperature gradients measured in

boreholes. Temperature gradient ratios are calculated by normalizing temperature gradients computed at each vertical finite element boundary with respect to temperature gradients calculated in the corresponding conduction-dominated case. Figure 4.10 shows contour plots of gradient ratio calculated for the temperature fields shown in Figures 4.1b, 4.1c, 4.1e and 4.1g. Note that Figure 4.10 illustrates the potential magnitude of errors introduced only by advective heat transfer. Heat flow estimates must also be corrected for the influence of surface topography, variations in thermal conductivity and the influence of thermal transients. Where exact corrections for these effects cannot be made, errors in heat flow estimates may exceed those indicated in Figure 4.10.

Where the gradient ratios shown in Figure 4.10 equal 1.0, temperature gradients are unaffected by the advective disturbance and measured temperature gradients match those of the corresponding conduction-dominated case. Shaded areas shown in Figure 4.10 highlight regions where measured temperature gradients may provide estimates of uncorrected regional heat flow with an error of less than 25 percent. Temperature gradients are only slightly affected at depth, even in systems with strong advective cooling, because the geometry of the boundary-value-problem is designed to ensure that the pattern of conductive heat flow in the basal low-permeability unit is undisturbed. In more complex situations, temperature gradient ratios at depth may

affected to a much greater degree. Where the gradient ratios differ from 1.0, the basal heat flow is effectively masked by groundwater flow.

Gradient ratios less than 1.0 indicate regions where temperature gradients measured in shallow boreholes would yield underestimates of uncorrected regional heat flow. In terrain with relief of 2 km over 6 km, such conditions should be expected when the bulk permeabilty of the mountain massif exceeds about 10^{-16} m^2 and humid climate causes high recharge rates. Mase *et al.* (1982) suggest that such conditions contribute to the regional low in heat flux (less than 30 mW/m^2) identifed in permeable volcanic rocks of the Cascade Range in California.

Negative gradient ratios (hatched regions in Figures 4.10b, 4.10c and 4.10d) indicate regions where temperature inversions and negative temperature gradients might be measured in shallow boreholes when bulk permeability equals about 10^{-15} m^2. Terrain with greater k_u produces expanded regions of negative gradient. Significant negative temperature gradients are reported in the upper several hundred metres of boreholes on the concave flank of Mount Hood, Oregon (Steele and Blackwell, 1982). If the concave domain shown in Figure 4.10d is a reasonable approximation of Mount Hood, it can be inferred that the permeability of the volcanic pile likely exceeds 10^{-16} m^2. In regions of reduced topographic relief, negative temperature gradients

will only be found (on a regional-scale) in terrain with greater bulk permeability. Brott *et al.* (1981) describe temperature inversions induced by regional groundwater flow within fractured basalts of the Snake River Plain. Topographic relief is approximately 1 km over 400 km and bulk permeability for the basalts generally exceeds 10^{-15} m^2. Negative temperature gradients are unlikely in high-relief terrain where arid climates yield reduced rates of groundwater recharge.

The gradient ratio map of Figure 4.10a suggests that thermal data collected in shallow boreholes located on the mountain flank are most likely to provide good indications of the magnitude of the basal heat flux when k_u is less than about 10^{-16} m^2 (or I_z is less than 2×10^{-10} m/sec). In terrain with k_u (or I_z) only one order of magnitude greater, shallow temperature data is unlikely to yield good estimates of regional heat flow (Figure 4.10b). Because k_u and I_z are difficult to estimate to a precision better than one or two orders of magnitude, it will be difficult to verify that temperature data collected from shallow boreholes provides a good estimate of regional heat flow. It should be noted, however, that the influence of thermal transients and uncertainties in understanding the thermal conductivity structure of the subsurface further reduce the likelihood that reliable estimates of basal heat flux can be made using data obtained from shallow boreholes.

Gradient ratio maps indicate that uncorrected regional heat flow may be overestimated by a factor in excess of 2.0 near the valley floor (Figure 4.10). In strongly disturbed regimes it appears necessary to drill at least 2 km below the valley floor to obtain reasonable estimates of regional heat flow. Heat flow measurements made in rugged mountainous terrain are, by necessity, often restricted to locations near the floor of narrow mountain valleys. Heat flow data collected from shallow boreholes (less than 200 m deep) in mountain valleys of the Coast Mountains, British Columbia yield consistent values of heat flow with plausible magnitude (about 80 to 100 mW/m^2) without correcting for possible advective heat transfer (Lewis *et al.*, 1985). This result suggests that regional groundwater flow in the Coast Mountains causes, at most, a weak advective disturbance. Furthermore, this implies that bulk permeability in the Coast Mountains is unlikely to exceed about 10^{-16} m^2. It should be recalled that an equivalent porous medium is assumed to provide an adequate representation of the fractured rock mass, with the exception of major through-going fracture zones. As a consequence, regions of reduced bulk permeability correspond to regions of decreased fracturing rather than to regions of decreased matrix permeability.

Souther (1975) notes that high-temperature phenomena such as boiling springs, fumaroles and mud pots are absent in the Coast Mountains of British Columbia; despite elevated

heat flow (Lewis *et al.*, 1985). Sixteen thermal springs, with temperatures seldom in excess of 65 °C, are scattered throughout a region of 1.3×10^4 km^2 (Souther and Halstead, 1973; Souther, 1975). Because these springs invariably issue from fractures in crystalline rock, the associated thermal regimes are presumed to be strongly controlled by permeable fracture zones. The sparse distribution of thermal springs suggests that conditions favoring elevated spring temperatures are found only in a few localized regions. In the absence of local heat sources, the location of the observed thermal springs may indicate regions where bulk permeability approaches 10^{-16} m^2. Elsewhere, bulk permeability likely falls outside the range of k_u (10^{-17} m^2 to 10^{-15} m^2) required for maximum spring temperatures. As noted previously, the plausible heat flow values reported for this region suggest that strong advective disturbance is absent at a regional scale and bulk permeability is likely less than 10^{-16} m^2.

Interpreting heat flow data can be complicated by the presence of alpine glaciers mantling a mountain massif. Figure 4.11 illustrates the influence of an alpine glacier on the temperature field in a convex domain with permeability 10^{-15} m^2 and infiltration rate 2×10^{-9} m/sec. The valley reference temperature (T_r) is reduced to 5 °C to represent a cooler climate. Using the approach described in Chapter 3, recharge beneath the glacier is limited to that derived from sub-glacial melting by thermal energy

originating at the basal heat source. Downslope of the glacier margin, rates of groundwater recharge equal the available infiltration rate on the free-surface. This transition, from reduced recharge beneath the glacier to high recharge downslope of the glacier margin, produces elevated subsurface temperatures and a reduced advective disturbance beneath the glacier. Borehole temperature data collected near glacier margins in high-permeability terrain may be difficult to interpret because the distorted groundwater flow system disturbs the patterns of heat transfer (Figure 4.11). The impact of alpine glaciers is reduced as permeability is reduced because less infiltration is accepted downslope of the glacier margin while rates of groundwater recharge generated by sub-glacial melting are little affected. It should be noted that similar results would be obtained where extensive units of low-permeability rocks or permafrost are found in upper regions of the domain.

Results presented in this section illustrate the use of numerical modelling to assess the disturbance of conductive thermal regimes by groundwater flow. A free-surface approach should be considered when confronted with a deep water table because temperature conditions at the water table are difficult to define without explicitly including the influence of heat transfer in the unsaturated zone. Such situations are most likely to be found in regions with high-permeability rocks and arid climate. A free-surface

approach may be unneccessary when temperatures at the water table can be assumed approximately equal to those at the ground surface. Such conditions might be found in low-permeability terrain where a water table close to the bedrock surface produces a thin unsaturated zone. Alternatively, high fluid flux found in high-permeability terrain with humid climate and deep water table may allow temperatures at the bedrock surface to be extrapolated vertically downward to an assumed water table. If the purpose of a modeling excercise is to identify regions where boiling might occur, a free-surface approach should be considered to ensure reasonable pressure conditions within the mountain massif.

4.5 CONCLUSIONS

1. Recognizing the pattern and magnitude of groundwater flow is fundamental to defining the pattern and magnitude of advective disturbance of conductive thermal regimes. A finite element model of fluid flow and heat transfer provides insight into the character of advective heat transfer in mountainous terrain. A free-surface approach eliminates the dependence of the solution results on difficult-to-estimate water table configurations by computing water table elevations as part of the solution process. Such an approach is most useful when assessing thermal regimes in high-permeability terrain with arid

climate. Here, the water table may lie deep below the bedrock surface. Conventional approaches that make *a priori* assumptions regarding the water table configuration require temperatures at the ground surface to be extrapolated to a water table that defines the upper boundary of the groundwater flow system. In more humid climates with lower permeability, water table elevations approach the bedrock surface and a free-surface approach may be unneccessary.

2. The position of the water table yields insight into the parameters that characterize the magnitude and onset of an advective disturbance. Where the water table lies below the bedrock surface, an advective threshold can be defined in terms of the available infiltration rate. Conductive thermal regimes are expected when available infiltration rates are less than about 10^{-11} m/sec. Conditions causing low available infiltration rates and deep water table elevations are most likely to be found in regions with arid climate. Where the water table coincides with the bedrock surface, the available infiltration rate no longer characterizes fluid flux within the domain. In such cases, an advective threshold specific to the topographic relief of the domain can be defined on the basis of bulk permeability. Numerical results suggest that the permeability-controlled advective threshold is about 10^{-18} m^2 in terrain with relief of 2 km over 6 km. The permeability threshold becomes proportionately greater as relief is reduced. Advective disturbance of thermal regimes is unlikely, on a regional

scale, where bulk permeability is less than 10^{-18} m^2.

3. High-relief topography amplifies the influence of surface topography on patterns of groundwater flow and advective heat transfer. Differing slope profiles and summit elevations on opposing valley walls yield an asymmetry in advective heat transfer that complicates the interpretation of thermal data sets. Thermal regimes beneath opposing valley slopes are effectively isolated when separated by a flat valley floor that is wider than the base of each adjacent mountain massif.

4. Numerical results indicate that special conditions are required in the variation of permeability within the mountain massif if free-convection cells are to develop. Otherwise, free-convection cells may be obliterated by topographically-driven groundwater flow.

5. Fracture zones can exert a profound influence on the pattern and magnitude of groundwater flow and advective heat transfer. There is a non-uniform variation of fluid flux within the fracture zone that reflects the character of the regional flow system. The strong interaction of fluid flow in the fracture zone and the surrounding rock mass produces an optimal range of permeability (between about 10^{-17} m^2 and 10^{-15} m^2) where the temperature of thermal springs may reach a maximum. In lower-permeability terrain, fluid flux is too slow to cause significant advective heat transfer. As a

consequence, spring temperatures approach ambient air temperature. In higher-permeability terrain, rapid fluid flux absorbs all thermal energy originating at the base of the domain with little increase in temperature. These conditions also contribute to spring temperatures approaching ambient air temperature.

6. Advective heat transfer causes an overall cooling of a mountain massif with small regions of heating near the valley floor. High-permeability and large available infiltration rates promote greater cooling and smaller regions of heating. In terrain with permeability in excess of about 10^{-15} m^2, the entire basal heat flow is absorbed by circulating groundwater and deflected to exit at the valley floor with little increase in subsurface temperatures. Such conditions mask the character of the basal heat flow and preclude using temperature data collected in shallow boreholes to estimate conductive regional heat flux.

7. Vertical temperature gradients may be overestimated by at least a factor of 2.0 where measured in mountain valleys. In high-permeability terrain (in excess of about 10^{-15} m^2), negative temperature gradients are predicted at median elevations on the mountain flank and within the mountain massif. Temperature data collected from shallow boreholes located on the mountain flank may yield reasonable estimates of vertical gradients and regional heat flow when bulk permeability is less than about 10^{-16} m^2.

8. The numerical model used in this study provides a basis for explaining the general character of thermal conditions observed in boreholes and at thermal springs located in mountainous terrain. Detailed examination of thermal anomalies at specific sites requires developing a three-dimensional equivalent of the existing two-dimensional model.

REFERENCES

Barry, R.G., Mountain weather and climate, Methuen, 1981.

Bodvarsson, G.S., S.M. Benson, and P.A. Witherspoon, Theory of the development of geothermal systems charged by vertical faults, Jour. Geophys. Res., 87, 9317-9328, 1982.

Brott, C.A., D.D. Blackwell, and J.P. Ziagos, Thermal and tectonic implications of heat flow in the Eastern Snake River Plain, Idaho, Jour. Geophys. Res., 86, 11709-11734, 1981.

Cheng, P., Heat transfer in geothermal systems, Adv. in Heat Transfer, Vol. 14, 1-105, 1978.

Domenico,P.A. and V.V. Palciauskas, Theoretical analysis of forced convective heat transfer in regional ground-water flow, Geol. Soc. Amer., Bulletin 84, 3303-3814, 1973.

Elder, J.W., Steady free convection in a porous medium heated from below, J. Fluid Mech., 27, 29-48, 1967.

Freeze, R.A., and J.A. Cherry, Groundwater, Prentice-Hall Inc., 1979.

Garven, G. and R.A. Freeze Theoretical analysis of the role of groundwater flow in the genesis of stratabound ore deposits: 2. Quantitative results, Am. Jour. Sci., 284, 1125-1174, 1984.

Goyal, K.P. and D.R. Kassoy, Fault zone controlled charging of a liquid-dominated geothermal reservoir Jour. Geophys. Res, 85, 1867-1875, 1980.

Kilty, K., D.S. Chapman, and C.W. Mase, Forced convective heat transfer in the Monroe Hot Springs geothermal area, Jour. of Volc. and Geoth. Res., Vol. 6, 257-272, 1979.

Kimura, S., and A. Bejan, The "heatline" visualization of convective heat transfer, J. of Heat Transfer, Trans. of the ASME, Vol. 105, 917-919, 1983.

Lewis, T.J., A.M. Jessop, and A.S. Judge, Heat flux measurements in Southwestern British Columbia: the thermal consequences of plate tectonics, Can. Jour. Earth Sci., 22, 1262-1273, 1985.

Lowell, R.P., Circulation in fractures, hot springs, and convective heat transport on mid-ocean ridge crests, Geophys. J. Roy. Astr. Soc., 40, 351-365, 1975.

Mase, C.W., J.H. Sass, A.H. Lachenbruch, and J.R. Munroe, Preliminary heat-flow investigations of the California Cascades, U.S. Geol. Survey, Open-File Report 82-150. 1982

Neuzil, C.E., Groundwater flow in low-permeability environments, Water Resour. Res., 22(8), 1163-1196, 1986.

Norton, D., and J. Knight, Transport phenomena in hydrothermal systems: Cooling plutons, Amer. Jour. of Sci., 277, 937-981, 1977.

Sass, J.H., A.H. Lachenbruch, R.J. Munroe, G.W. Greene, and T.H. Moses, Jr., Heat tflow in the Western United States, J. Geophys. Res., 76(26), 6376-6413, 1971.

Smith, L., and D.S. Chapman,The influence of water table configuration on the near-surface thermal regime, Jour. of Geodynamics, 4, 183-198, 1985.

Smith, L., and D.S. Chapman, On the thermal effects of groundwater flow 1. Regional scale systems, Jour. Geophys. Res., 88(1), 593-608, 1983.

Sorey, M.L. Numerical modeling of liquid geothermal systems, U.S. Geol. Surv. Prof. Paper 1044-D, 1978.

Souther, J.G. Geothermal potential of Western Canada, Proc. 2nd. U.N. Symp. on Development and Use of Geothermal Resources, San Francisco, Calif., Vol. 1, 259-267, 1975.

Souther, J.G., and Halstead, E.C., Mineral and thermal waters of Canada, Canada Dept. of Energy, Mines and Resources, Paper 73-18, 1973.

Steele, J. L., and D.D. Blackwell, Heat flow in the vicinity of the Mount Hood Volcano, Oregon, in Geology and geothermal resources of the Mount Hood area Oregon, Oregon Dept. of Geol. and Min. Ind., Special Paper 14, pp 31-42, 1982.

van der Kamp, G., Interactions betwee heat flow and groundwater flow - A review, Proj. 109-17, Waterloo Res. Inst., Univ. of Waterloo, Waterloo, Ont., 1982.

TABLE 4.1

SIMULATION SUMMARY AND GUIDE TO ILLUSTRATIONS - CHAPTER 4

FACTOR	FIGURE
TOPOGRAPHY	
Slope Profile	4.1
Valley Asymmetry	4.6
Radial Symmetry	4.7
GEOLOGY	
Bulk Permeability	4.1, 4.3
Permeable Fracture Zones	4.8
CLIMATE	
Available Infiltration	4.1, 4.3
Alpine Glaciers	4.11
Surface Temperature	NS
THERMAL REGIME	
Basal Heat Flow	4.1
Free-Convection	4.5
Thermal Springs	4.8, 4.9
ADVECTIVE THERMAL DISTURBANCE	
Onset	4.1, 4.4
Pattern	4.1, 4.3
Magnitude	4.2, 4.10

Notes:

NS Not Shown

TABLE 4.2

TYPICAL SIMULATION PARAMETERS - CHAPTER 4

Fluid Flow Parameters

k_b		permeability of basal unit	1.0×10^{-22} m^2
k_u	*	permeability of upper unit	1.0×10^{-15} m^2
I_z	*	vertical infiltration rate	2.0×10^{-9} m/s

Thermal Parameters

H_b	*	basal heat flow	60.0 mW/m^2
G_l	*	thermal lapse rate	5 K/km
T_r	*	reference surface temperature	10 °C
n_b		porosity of basal unit	0.01
n_u		porosity of upper unit	0.10
λ^s		solid thermal conductivity	2.50 W/mK
λ^f		fluid thermal conductivity	0.58 W/mK
λ^v		vapor thermal conductivity	0.024 W/mK
C_f		specific heat capacity of water	4186.0 J/kgK
S		saturation above water table	0.0
a_l		longitudinal thermal dispersivity	100.0 m
a_t		transverse thermal dispersivity	10.0 m

Note: * Denotes parameters changed in simulation series.

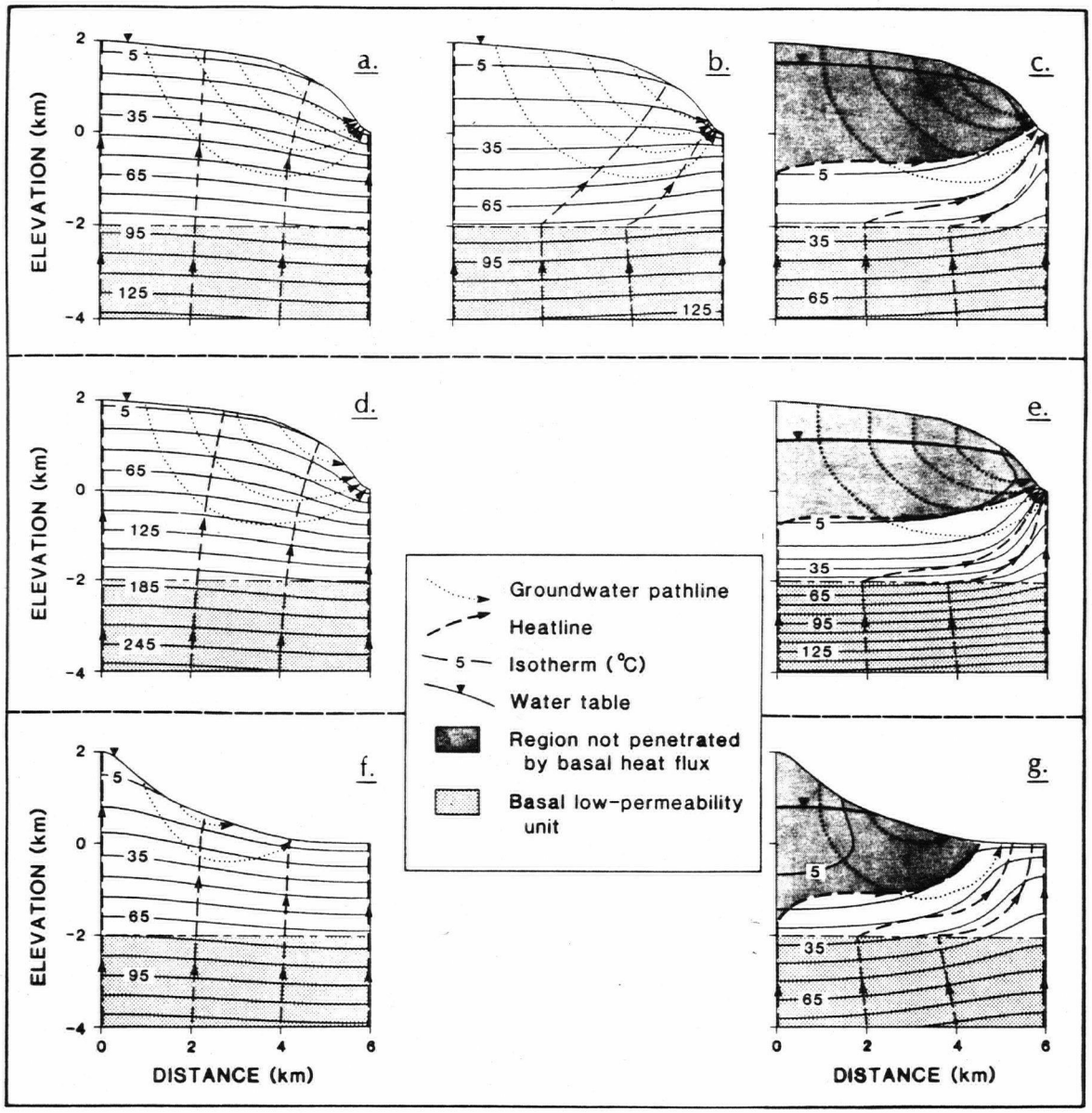

Figure 4.1. Patterns of groundwater flow and heat transfer in convex and concave topography simulated with the reference conditions of Table 4.2 (except where noted);

a. $k_u = 10^{-18}$ m^2,

b. $k_u = 10^{-16}$ m^2,

c. $k_u = 10^{-15}$ m^2 (reference case),

d. $k_u = 10^{-18}$ m^2 and $H_b = 120$ mW/m^2,

e. $k_u = 10^{-15}$ m^2 and $H_b = 120$ mW/m^2,

f. $k_u = 10^{-18}$ m^2,

g. $k_u = 10^{-15}$ m^2.

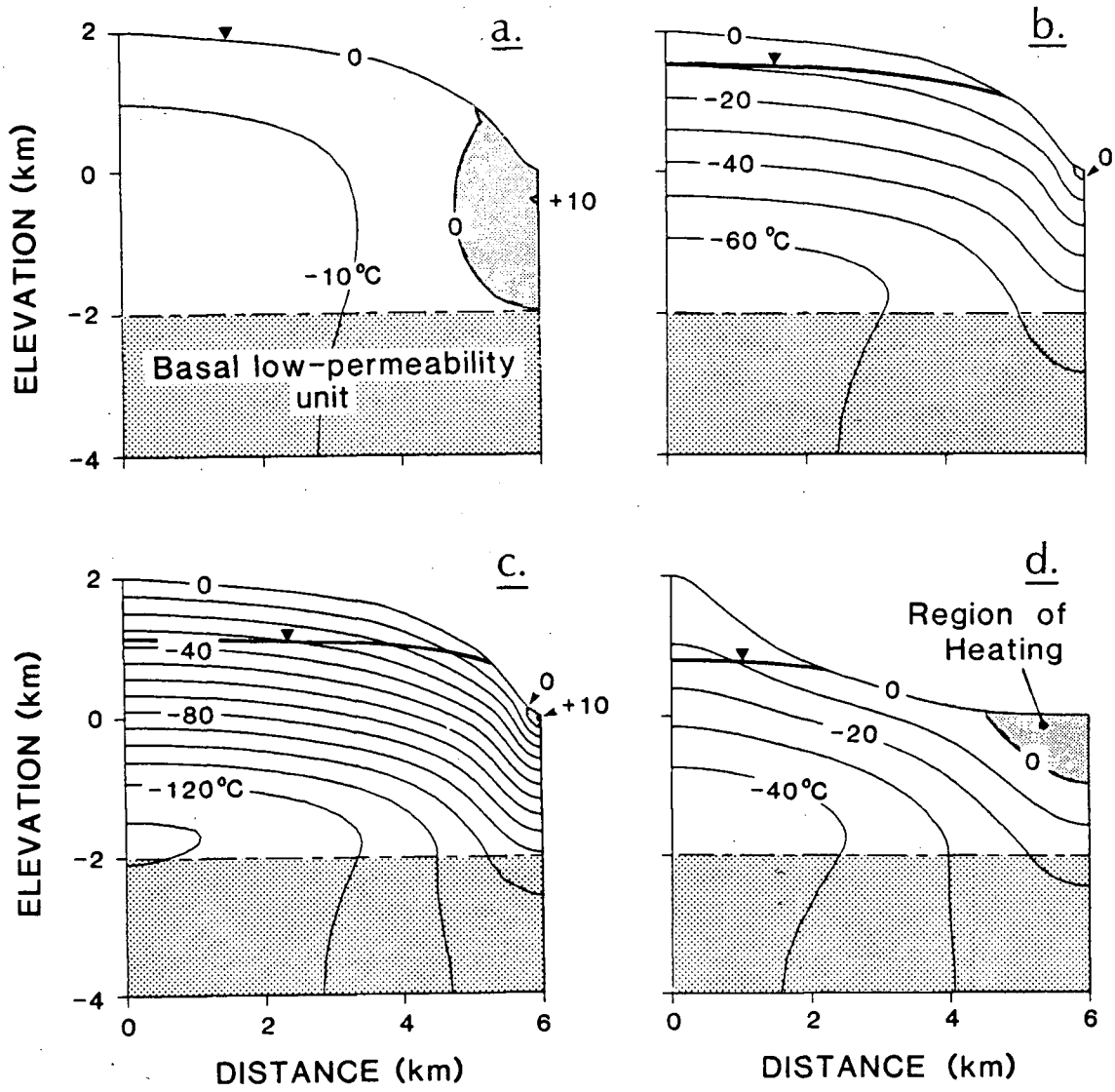

Figure 4.2. Contour plots of temperature residual (°C);
a. k_u = 10^{-16} m² and H_b = 60 mW/m²,
b. k_u = 10^{-15} m² and H_b = 60 mW/m²,
c. k_u = 10^{-15} m² and H_b = 120 mW/m²,
d. k_u = 10^{-15} m² and H_b = 60 mW/m².

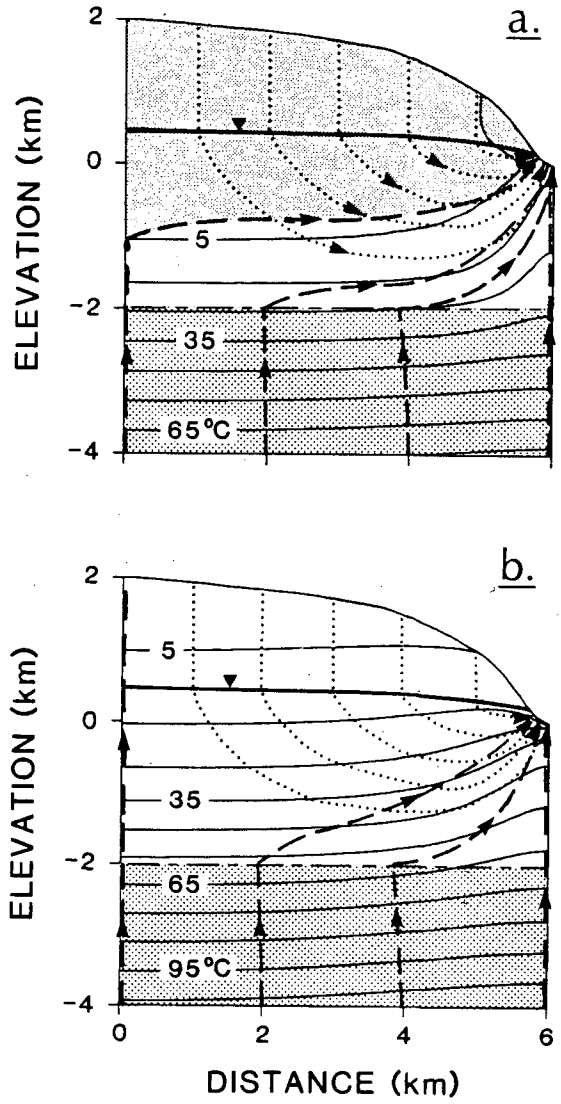

Figure 4.3. Matching water table configurations in convex topography with H_b = 60 mW/m²;
a. k_u = 5x10⁻¹⁵ m² and I_z = 2x10⁻⁹ m/sec,
b. k_u = 10⁻¹⁵ m² and I_z = 4x10⁻¹⁰ m/sec.

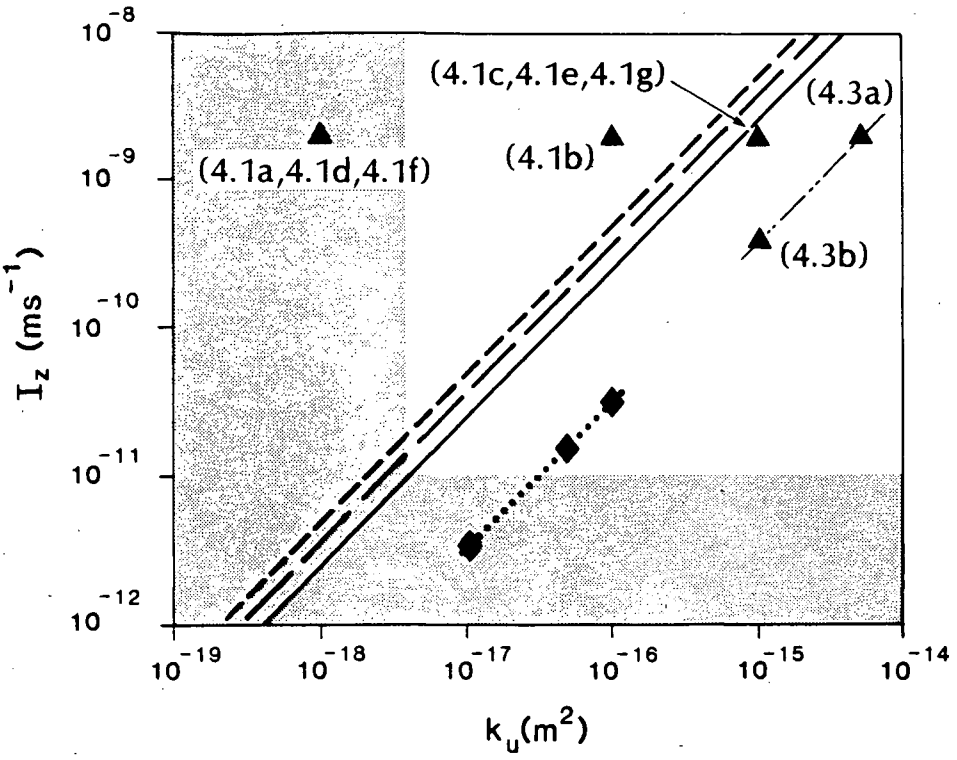

▲ (2a) Figure number showing simulation results for plotted I_z, k_u

Conduction-dominated: Convex slope profile, H_b = 60 mW/m^2

Water Table Thresholds	H_b mW/m^2	Relief km/km
Concave slope profile	60	2/6
Convex slope profile	120	2/6
Convex slope profile	60	2/6
Smith & Chapman (1983)	60	1/40
Max. water table elevation ≈ 460 m		
Convex slope profile	60	2/6

Figure 4.4. Influence of infiltration I_z and permeability k_u on water table elevations and advective thresholds.

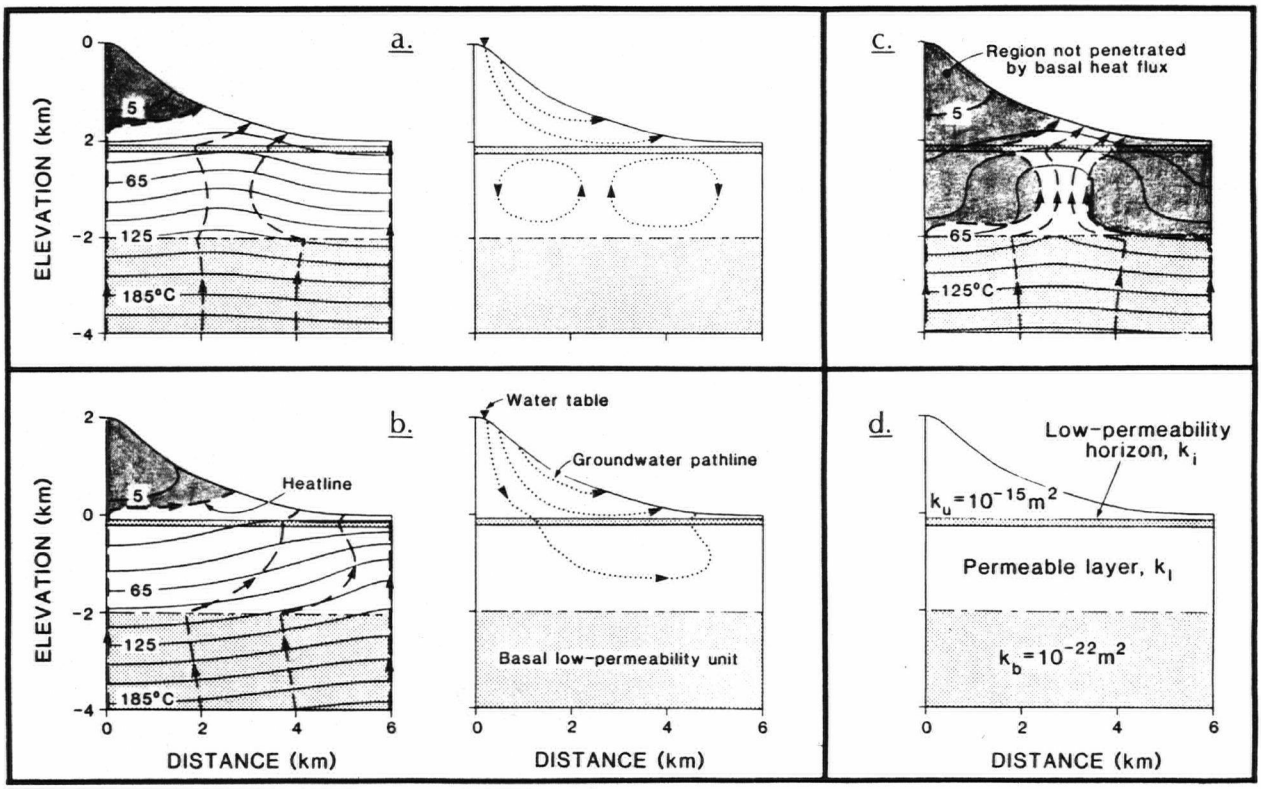

Figure 4.5. Thermal regimes and patterns of groundwater flow in mixed free- and forced-convection scenarios with H_b = 120 mW/m², I_z = 5x10⁻⁹ m/sec and k_u = 10⁻¹⁵ m²;
a. k_i = 10⁻¹⁹ m² and k_l = 5x10⁻¹⁵ m²,
b. k_i = 10⁻¹⁷ m² and k_l = 5x10⁻¹⁵ m²,
c. k_i = 10⁻¹⁹ m² and k_l = 5x10⁻¹⁴ m²
d. geologic conditions for simulations.

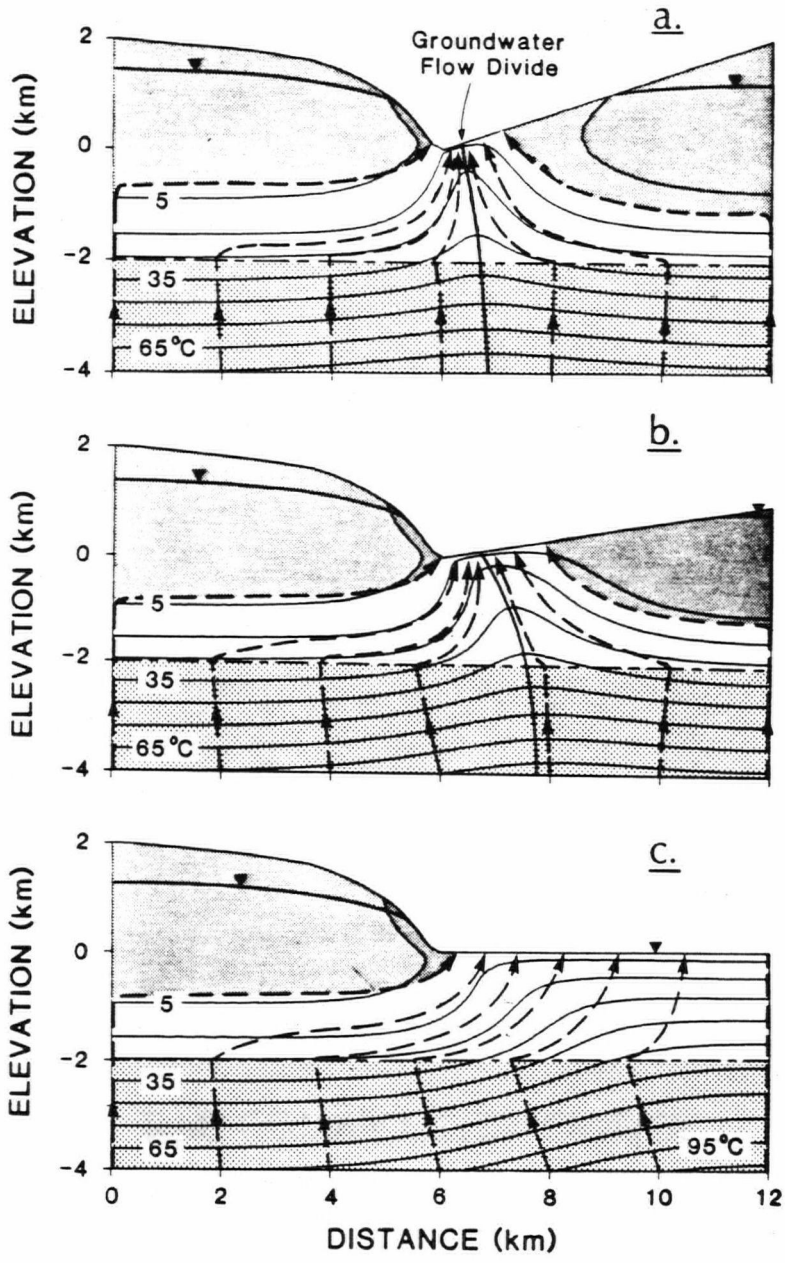

Figure 4.6. Thermal regimes beneath mountain valleys simulated with reference conditions of Table 4.2;

a. opposing summits have equal relief and differing slope profile,

b. linear summit has relief one half that of the convex summit,

c. convex summit adjacent to a flat plain.

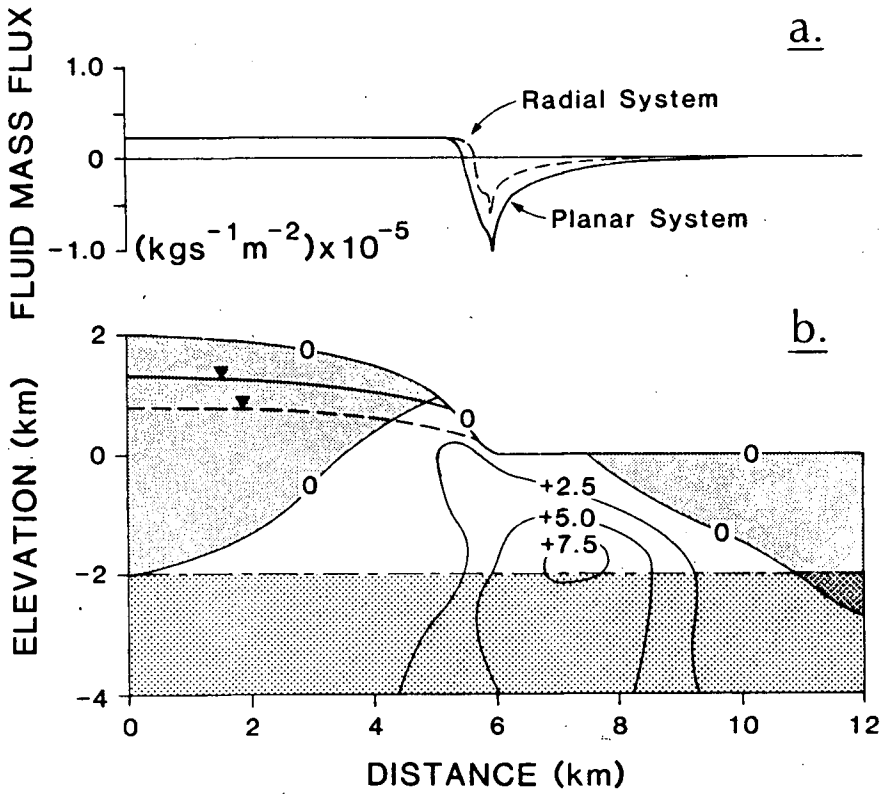

Figure 4.7. Comparison of thermal regimes in radial and planar symmetry;
a. fluid flux normal to the upper boundary,
b. temperature difference contours (°C).

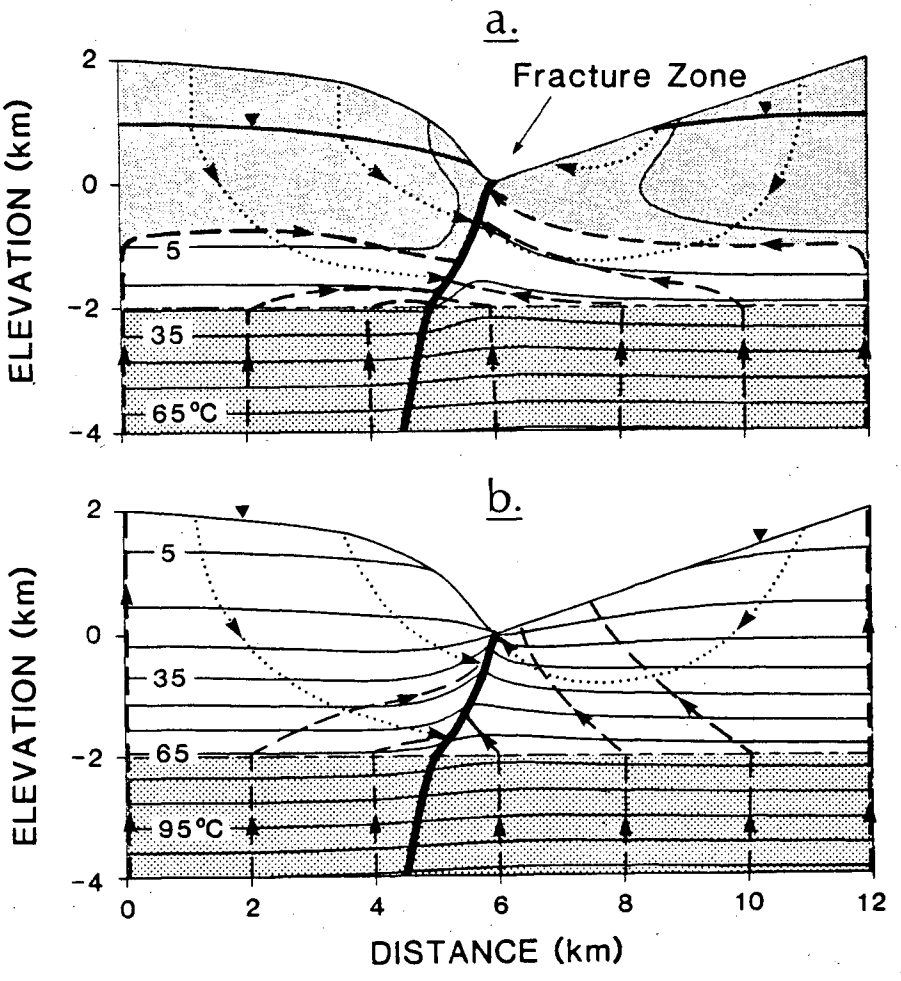

Figure 4.8. Influence of a steeply dipping fracture zone with uniform $k_f \cdot b = 10^4 \cdot k_u$ ($m^2 \cdot m$) on thermal regimes within the asymmetric topography of Figure 4.6a;
a. $k_u = 10^{-15}$ m^2,
b. $k_u = 10^{-16}$ m^2,

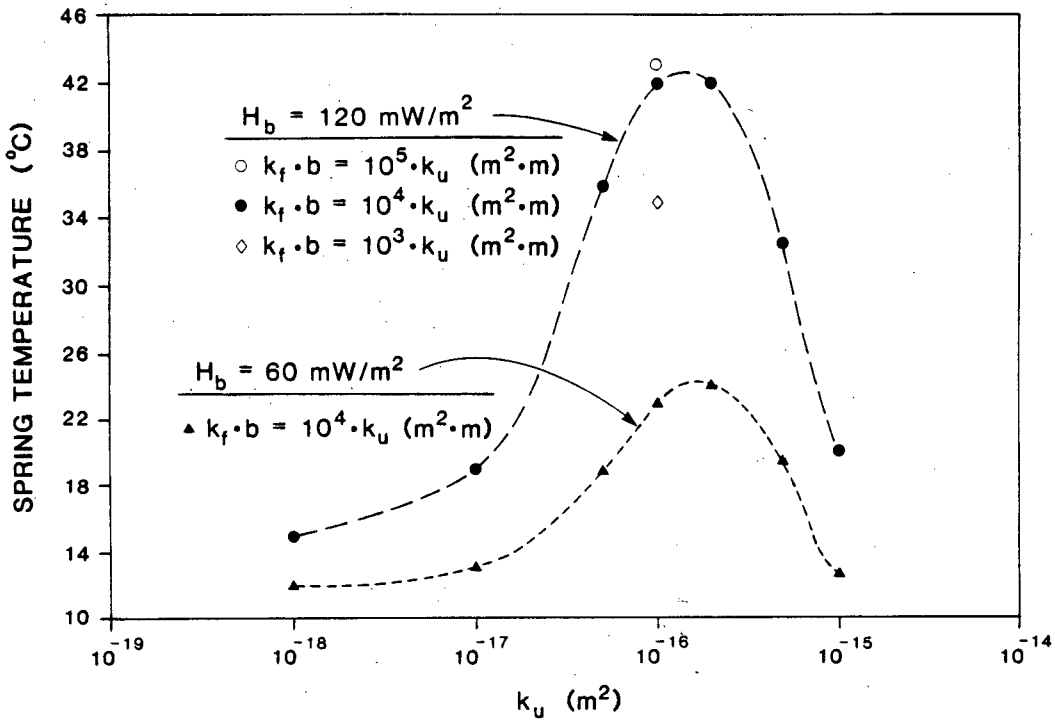

Figure 4.9. Spring temperature as a function of upper zone permeability k_u, transmissivity of the fracture zone $k_f \cdot b$, and basal heat flow H_b.

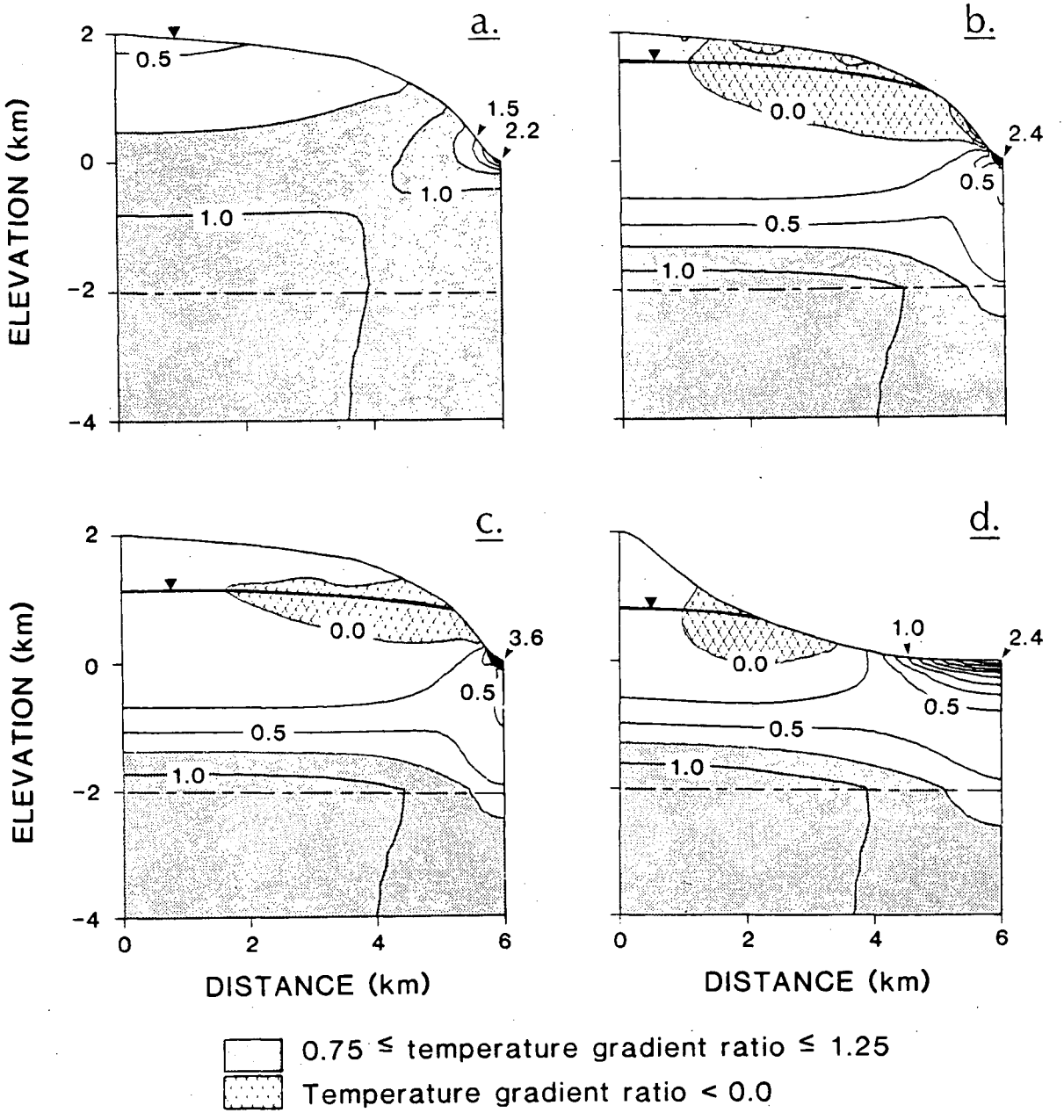

Figure 4.10. Contour plots of temperature gradient ratio;
a. k_u = 10^{-16} m² and H_b = 60 mW/m²,
b. k_u = 10^{-15} m² and H_b = 60 mW/m²,
c. k_u = 10^{-15} m² and H_b = 120 mW/m²
d. k_u = 10^{-15} m² and H_b = 60 mW/m²

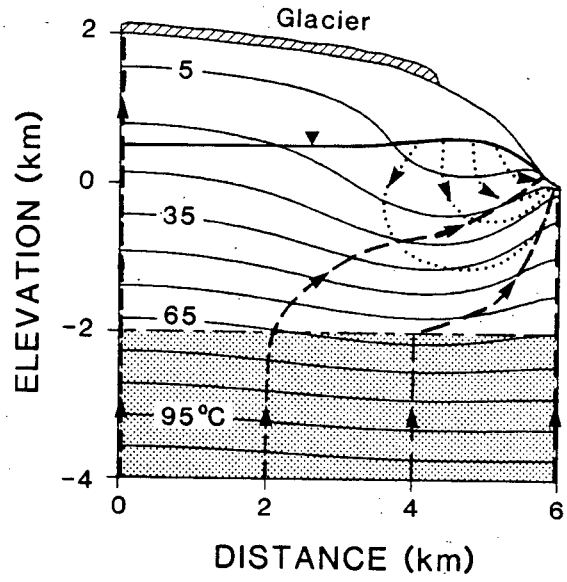

Figure 4.11. Influence of a glacier mantling a convex mountain from 1500 m to 2000 m above the valley floor.

CHAPTER 5

SUMMARY OF CONCLUSIONS

A finite element model is developed to simulate steady groundwater flow and heat transfer through vertical sections of terrain with mountainous topography. A free-surface approach eliminates the dependence of the solution results on difficult-to-estimate water table configurations by computing water table elevations as part of the solution process. Conventional approaches that make *a priori* assumptions regarding the water table position require temperatures at the ground surface to be extrapolated to a water table that defines the upper boundary of the groundwater flow system. This difficulty is avoided by assuming one-dimensional advective heat transfer by vertical fluid flow in the unsaturated zone. When the water table lies below the bedrock surface, the rate of groundwater flow in the unsaturated zone is controlled by the available infiltration rate. This parameter, viewed as a percentage of the mean annual precipitation rate, defines the maximum rate of groundwater recharge possible for a given set of climatic conditions. This method is most useful when simulating mountainous terrain where the water table lies deep below the bedrock surface. Numerical results suggest that such conditions are most likely in high-permeability terrain (greater than 10^{-15} m^2) with arid climate, or where

groundwater recharge is restricted by extensive alpine glaciers.

Simulation results indicate that slope profile, rock permeability, infiltration rate, glaciers and basal heat flow exercise a strong influence on water table configurations and the rates of groundwater flow. For example, a three-fold increase in permeability (or a three-fold decrease in available infiltration rate) can cause at least 500 m decline in water table elevation and a 45 percent change in total flow through a system with relief of 2 km over 6 km. Variations of similar magnitude are found to result when; a) two extremes of slope profile are compared (concave and convex), b) alpine glaciers act to restrict groundwater recharge, d) thin permeable fracture zones and horizons are incorporated in the flow system and d) two extremes of basal heat flow are compared (30 to 120 mW/m^2). Recognizing the influence of these factors on rates and patterns of advective heat transfer is fundamental to assessing the disturbance of conductive thermal regimes by groundwater flow.

The high topographic relief of mountainous terrain amplifies the impact of slope profile and thin permeable zones on patterns of groundwater flow and advective heat transfer. For example, asymmetry in ridge topography alone can cause significant displacement of upland groundwater divides that, in turn, may enhance inter-basin groundwater

flow. Furthermore, lowland groundwater divides displaced by asymmetry in valley topography can lead to uncertainties in defining the source of chemical or thermal signatures found in groundwater samples obtained from springs and shallow boreholes. Thin permeable fault zones and horizons (thickness of 0.1 m and permeability 10^4 times the surrounding rock or thickness of 100 m and permeability 10 times the surrounding rock) exert a strong influence on groundwater flow patterns. This influence further enhances the possibility of inter-basin groundwater flow and complicates accurate interpretation of chemical sampling results and borehole temperature measurements. The strong interaction of fluid flow in the fracture zone and the surrounding rock mass produces an optimal range of permeability (between about 10^{-17} m^2 and 10^{-15} m^2) where the temperature of thermal springs may reach a maximum. In terrain with bulk permeability values outside this range, spring temperatures approach ambient air temperature.

Simulation results indicate that simply identifying the position of the water table in mountainous terrain will provide little insight into the nature of the groundwater flow system and the character of the advective thermal disturbance. This result reflects the fact that the water table should be viewed as an internal characteristic of the flow system, rather than an important controlling factor. The position of the water table, however, does yield insight into the <u>parameters</u> that characterize the magnitude and

onset of an advective disturbance. Where the water table lies below the bedrock surface, an advective threshold can be defined in terms of the available infiltration rate. Conductive thermal regimes are expected when available infiltration rates are less than about 10^{-11} m/sec. Conditions causing low available infiltration rates and a deep water table are most likely found in regions with arid climate. In more humid climates where the water table coincides with the bedrock surface, the available infiltration rate no longer characterizes fluid flux within the domain. In such cases, an advective threshold can be defined on the basis of bulk permeability that is specific to the topographic relief of the domain. Numerical results suggest that the permeability-controlled advective threshold is about 10^{-18} m^2 in terrain with relief of 2 km over 6 km. The permeability threshold becomes proportionately greater as relief is reduced.

The numerical model used in this study provides a basis for explaining the character of thermal conditions observed in boreholes and at thermal springs located in mountainous terrain. In addition, the numerical results provide insight into the possible errors associated with making heat flow measurements in mountainous terrain. Active circulation of groundwater in terrain with permeability in excess of about 10^{-15} m^2 effectively masks the character of the basal heat flux. Such conditions preclude using temperature data collected in shallow boreholes to estimate conductive

regional heat flux and to identify underlying geothermal systems. Errors associated with estimating regional heat flux in advectively disturbed thermal regimes are quantified using a temperature gradient ratio. This ratio expresses the deviation of vertical temperature gradients from those of the corresponding conductive case. Vertical temperature gradients may be overestimated by at least a factor of 2.0 where measured in mountain valleys. In high-permeability terrain (in excess of about 10^{-15} m^2), negative temperature gradients are predicted at median elevations on the mountain flank and within the mountain massif. Temperature data collected from shallow boreholes located on the mountain flank may yield reasonable estimates of vertical gradients (and regional heat flow) when bulk permeability is less than about 10^{-16} m^2.

CUMULATIVE REFERENCE LIST

Baca, R.G., R.C. Arnett, and D.W. Langford, Modelling fluid flow in fractured-porous rock masses by finite element techniques, International Journal for Numerical Methods in Fluids, 4, 337-348, 1984.

Barry, R.G., Mountain weather and climate, Methuen, 1981.

Bear, J., Dynamics of fluids in porous media, American Elsevier, 1972.

Bear, J., Hydraulics of Groundwater, McGraw-Hill, 1979.

Birch, F., Flow of heat in the Front Range, Colorado, Bull. Geol. Soc. Amer., 61, 567-630, 1950.

Black, G.L., D.D. Blackwell, and J.L. Steele, Heat flow in the Oregon Cascades, in Geology and Geothermal Resources of the Central Oregon Cascades Range, ed. by G.R. Priest and B.F. Vogt, Oregon Dept. of Geol. and Min. Ind., Special Paper 15, 69-76, 1983.

Blackwell, D.D., A transient model of the geothermal system of Long Valley Calder, California, Jour. Geophys. Res., 90, 11229-11242, 1985.

Blackwell. D.D., and J.L. Steele, A summary of heat flow studies in the Cascade Range, Geoth. Resources Council Trans., 7, 233-236, 1983.

Bodvarsson, G.S., S.M. Benson, and P.A. Witherspoon, Theory of the development of geothermal systems charged by vertical faults, Jour. Geophys. Res., 87, 9317-9328, 1982.

Bodvarsson, G.S., and K. Pruess, Modeling studies of geothermal systems with a free water surface, Stanford Ninth Annual Workshop on Geothermal Resources Engineering, 1983.

Bortolami, G.S., B. Ricci, G.G. Susella, and G.M. Zuppi, Hydrogeochemistry of the Corsaglia Valley, Maritime Alps Piedmont Italy, Jour. of Hydrol., 44, 57-79, 1979.

Brott, C.A., D.D. Blackwell, and J.P. Ziagos, Thermal and tectonic implications of heat flow in the Eastern Snake River Plain, Idaho, Jour. Geophys. Res., 86, 11709-11734, 1981.

Bryson, R.A., and F.K. Hare, Climates of North America, Elsevier, 1974.

Buntebarth, B., Geothermics, Springer-Verlag, 1984.

Chapman, D.S., and L. Rybach, Heatflow anomalies and their interpretation, Jour. of Geodynamics, 4, 3-37, 1985.

Cheng, P., Heat transfer in geothermal systems, Adv. in Heat Transfer, Vol. 14, 1-105, 1978.

Domenico,P.A. and V.V. Palciauskas, Theoretical analysis of forced convective heat transfer in regional ground-water flow, Geol. Soc. Amer., Bulletin 84, 3303-3814, 1973.

Elder, J.W., Steady free convection in a porous medium heated from below, J. Fluid Mech., 27, 29-48, 1967.

Faust, C.R., J.W. Mercer, S.D. Thomas, and W.P. Balleau, Quantitative analysis of existing conditions and production strategies for the Baca Geothermal System, New Mexico, Water Resour. Res., 20(5), 601-618, 1984.

Fox, F.M., The Simplon tunnel, Minutes of the Proceedings of the Inst. of Civil Engineers, 168, 61-86, 1907.

Freeze, R.A., and J.A. Cherry, Groundwater, Prentice-Hall Inc., 1979.

Freeze, R.A., and P.A. Witherspoon, Theoretical analysis of regional groundwater flow: 2. Effect of water-table configuration and subsurface permeability variation, Water Resour. Res., 3, 623-634, 1967.

Frind, E.O., Simulations of long-term transient density-dependant transport in groundwater, Adv. Water Resourc., 5, 73-88, 1982.

Garven, G. and R.A. Freeze, Theoretical analysis of the role of groundwater flow in the genesis of stratabound ore deposits: 2. Quantitative results, Am. Jour. Sci., 284, 1125-1174, 1984.

Gosnold, W.D., Heat flow and ground water flow in the great plains of the United States, Jour. of Geodynamics, 4, 247-264, 1985.

Goyal, K.P. and D.R. Kassoy, Fault zone controlled charging of a liquid-dominated geothermal reservoir Jour. Geophys. Res, 85, 1867-1875, 1980.

Halstead, E.C., Groundwater investigation, Mount Kobau, British Columbia, Canada Inland Waters Branch, Dept. of Energy Mines and Resources, Tech. Bull. 17, 1969.

Hennings, F., On the question of long railway tunnels Construction, ventilation and operation, Bull. of the Internl. Railway Congress Assoc., 24(10), 943-983, 1910.

Horne, R.N., and M.J. O'Sullivan, Numerical modeling of a desaturating geothermal reservoir, Numerical Heat Transfer, 1, 203-216, 1978.

Huyakorn, P.S., and G.F. Pinder, Computational methods in subsurface flow, Academic Press, 1983.

Ingebritsen, S.E., and M.L. Sorey, A quantitative analysis of the Lassen hydrothermal system, North Central California, Water Resour. Res., 21(6), 853-868, 1985.

Jamier, D., Etude de la fissuration, de l'hydrogeologie et de la geochemie des eaux profondes des massifs de l'Arpille et du Mont Blanc, PhD. dissertation, Faculte des Sciences, Universite de Neuchatel, Switzerland (in French), 1975.

Jamieson, G.R., and R.A. Freeze, Determining hydraulic conductivity distributions in a mountainous area using mathematical modeling, Groundwater, 21(2), 168-177, 1983.

Keays, R.N., Construction methods in the Moffat Tunnel, Amer. Soc. Civil Eng., 62, 63-112, 1928.

Keenan, J.H., F.G. Keyes, P.G. Hill, and J.G. Moore, Steam Tables, 162 pp., John Wiley, 1978.

Kilty, K., D.S. Chapman, and C.W. Mase, Forced convective heat transfer in the Monroe Hot Springs geothermal area, Jour. of Volc. and Geoth. Res., Vol. 6, 257-272, 1979.

Kimura, S., and A. Bejan, The "heatline" visualization of convective heat transfer, J. of Heat Transfer, Trans. of the ASME, Vol. 105, 917-919, 1983.

Lahsen, A., and P. Trujillo, The geothermal field of El Tatio, Chile, Proc. 2nd. U.N. Symp. on Development and Use of Geothermal Resources, San Francisco, Calif., Vol. 1, 157-175, 1975.

Lauscher, F., Wettweite typen der hohenabgangigkeit des Niederschlags, Wetter U. Leben., 28, 80-90, 1976.

Lewis, T.J., A.M. Jessop, and A.S. Judge, Heat flux measurements in Southwestern British Columbia: the thermal consequences of plate tectonics, Can. Jour. Earth Sci., 22, 1262-1273, 1985.

Lowell, R.P., Circulation in fractures, hot springs, and convective heat transport on mid-ocean ridge crests, Geophys. J. Roy. Astr. Soc., 40, 351-365, 1975.

Majorowicz, J.A., F.W. Jones, H.L. Lam, and A.M. Jessop, Terrestrial heat flow and geothermal gradients in relation to hydrodynamics in the Alberta Basin, Canada, Jour. Geodynamics, 4, 265-283, 1985.

Martinec, J., H. Oeschager, U. Schotterer, and U. Siegenthaler, Snowmelt and groundwater storage in an alpine basin, in, Hydrological Aspects of Alpine and High Mountainous Terrain, ed. J. W. Glen, IAHS Publ. 138, 169-175, 1982.

Mase, C.W., J.H. Sass, A.H. Lachenbruch, and J.R. Munroe, Preliminary heat-flow investigations of the California Cascades, U.S. Geol. Survey, Open-File Report 82-150. 1982

Mears, F., The eight mile Cascade Tunnel, Great Northern Railway Part II. Surveys, construction methods and a comparison of routes, Amer. Soc. Civil Eng., Trans., 96, 915-1004, 1932.

Neuman, S.P., and P.A. Witherspoon, Finite element method of analyzing steady seepage with a free-surface, Water Resour. Res., 6(3), 889-897, 1970.

Neuzil, C.E., Groundwater flow in low-permeability environments, Water Resour. Res., 22(8), 1163-1196, 1986.

Norton, D., and J. Knight, Transport phenomena in hydrothermal systems: Cooling plutons, Amer. Jour. of Sci., 277, 937-981, 1977.

Patankar, S.V., Numerical heat transfer and fluid flow, McGraw Hill, 1980.

Paterson, W.S.B., The physics of glaciers, Pergamon, 1981.

Prats, M., The effect of horizontal fluid flow on thermally induced convection currents in porous mediums, Jour. Geophys. Res., 71(2), 4835-4837, 1966.

Province of British Columbia, Groundwater observation wells of British Columbia, British Columbia Water Resources Service, Water Investigations Branch, 1974.

Raithby, G.D., and K.E. Torrance, Upstream weighting differencing schemes and their application to elliptic problems involving fluid flow, Comput. Fluids, 2, 191-206, 1974.

Reader, J.F., and Fairbank, B.D., Heat flow in the vicinity of the Meager Volcanic Complex, Southwestern British Columbia, Geoth. Resour. Council Trans., Vol. 7, 535-539, 1983.

Ross, B., A conceptual model of deep unsaturated zones with negligible recharge, Water Resour. Res., 20(11), 1627-1629, 1984.

Ruffner, J.A., and F.E. Blair, Climates of the States with current tables of normals 1941-1970 and means and extremes to 1975, National Ocean and Atmospheric Adimin., Vols. I and II, 1975.

Sass, J.H., A.H. Lachenbruch, R.J. Munroe, G.W. Greene, and T.H. Moses, Jr., Heat tflow in the Western United States, J. Geophys. Res., 76(26), 6376-6413, 1971.

Sauty, J.P., A.C. Gringarten, H. Fabris, D. Thiery, A. Menjoz, and P.A. Landel, Sensible energy storage in aquifers, 2, Field experiments and comparisons with theoretical results, Water Resour. Res., 18(2), 245-252, 1982.

Schadt, M.H., Les resultats scientifiques du percement du tunnel du Simplon, Bulletin Technique de la Suisse Romande, 125-178, 1905.

Scharli, U., and L. Rybach, On the thermal conductivity of low-porosity crystalline rocks, Tectonophysics, 103, 307-313, 1984.

Schermerhorn, V.P., Relations bewteen topography and annual precipitation in Western Oregon and Washington, Water Resour. Res., 3(3), 707-711, 1967.

Sklash, M.G., and R.N. Farvolden, The role of groundwater in storm runoff, Jour. of Hydrol., 43, 45-65, 1979.

Slaymaker, H.O., and L.J. Zeman, Influence of altitude and continentality on watershed hydrology in the Coast Mountains of British columbia, Proc. Canadian Hydrology Symposium, National Research Council, 1975.

Smart, C.C., The hydrology of the Castleguard Karst, Columbia Icefields, Alberta, Canada, Arctic and Alpine Research, 15(4), 471-486, 1985.

Smith, L., and D.S. Chapman,The influence of water table configuration on the near-surface thermal regime, Jour. of Geodynamics, 4, 183-198, 1985.

Smith, L., and D.S. Chapman, On the thermal effects of groundwater flow 1. Regional scale systems, Jour. Geophys. Res., 88(B1), 593-608, 1983.

Smith, M.W., Microclimatic influences on ground temperatures and permafrost distribution, Mackenzie Delta, Northwest Territories, Canadian Journal of Earth Science, 12, 1421-1438, 1975.

Sorey, M.L., Evolution and present state of the hydrothermal system in Long Valley Caldera, Jour. Geophys. Res., 90, 11219-11228, 1985a.

Sorey, M.L., Types of hydrothermal convection systems in the Cascade Range of California and Oregon, Proc. Workshop on Geothermal Resources of the Cascade Range, ed. M. Guffanti and L.J.P. Muffler, 63-67, 1985b.

Sorey, M.L. Numerical modeling of liquid geothermal systems, U.S. Geol. Surv. Prof. Paper 1044-D, 1978.

Souther, J.G. Geothermal potential of Western Canada, Proc. 2nd. U.N. Symp. on Development and Use of Geothermal Resources, San Francisco, Calif., Vol. 1, 259-267, 1975.

Souther, J.G., and Halstead, E.C., Mineral and thermal waters of Canada, Canada Dept. of Energy, Mines and Resources, Paper 73-18, 1973.

Spalding, D.B., A novel finite difference formulation for differential equations involving both first and second derivatives Int. J. Numer. Methods Eng., 4, 551-559, 1972.

Steele, J. L., and D.D. Blackwell, Heat flow in the vicinity of the Mount Hood Volcano, Oregon, in Geology and geothermal resources of the Mount Hood area Oregon, Oregon Dept. of Geol. and Min. Ind., Special Paper 14, pp 31-42, 1982.

Storr, D., and H.L. Ferguson, The distribution of precipitation in some mountainous Canadian watersheds, in, Distribution of Precipitation in Mountainous Areas, Geilo Symposium, Norway, Proc. World Meteor. Assoc., WMO/OMM No. 326, Vol. II, 243-263, 1972.

Thompson, W.T., How and why to distinguish between mountains and hills, Prof. Geographer, 16, 6-8, 1964.

van der Kamp, G., Interactions betwee heat flow and groundwater flow - A review, Proj. 109-17, Waterloo Res. Inst., Univ. of Waterloo, Waterloo, Ont., 1982.

Verruijt, A., Theory of Groundwater Flow, Macmillan Press, 1970.

Walsh, J.B., and E.R., Decker, Effect of pressure and saturating fluid on the thermal conductivity of compact rock, Jour. Geoph. Res., 71, 3053-3061, 1966.

Waring, G.A., Thermal springs of the United States and other countries of the world - a summary, U.S. Geol. Survey Prof. Paper 492, 1965.

Watson, J.T.R, R.J. Basu, and J.V. Sengers, An improved representative equation for the dynamic viscosity of water substance, Jour. Phys. Chem. Ref. Data, 9(3), 1255-1279, 1981.

Woodbury, A.D., and L. Smith, On the thermal effects of three-dimensional groundwater flow, Jour. Geophys. Res., 90, 759-767, 1985.

Zablocki. C.J., R.I. Tilling, D.W. Peterson, R.L. Christiansen, G.V. Keller, and J.C. Murray, A deep research hole at the summit of an active volcano, Kilauea, Hawaii, Geoph. Res. Lett., 1(7), 323-326, 1974.

APPENDIX I

NOMENCLATURE

b	width of fracture zone	L
C_f	specific heat capacity of fluid	L^2/t^2T
D_{ij}	conduction dispersion tensor for fluid in rock matrix	L^2/T
D_s	conduction dispersion tensor for fluid in fracture zone	L^2/T
G_l	thermal lapse rate	T/L
g	gravitational constant	L/t^2
H_b	basal heat flux	M/t^3
h	equivalent freshwater head	L
I_z	available infiltration rate	L/T
I^*	infiltration ratio	dimensionless
K	hydraulic conductivity	L/t
K_o	reference hydraulic conductivity	L/t
k_b	permeability of basal unit	L^2
k_f	permeability of fracture filling	L^2
k_{ij}	permeability tensor for porous medium	L^2
k_u	permeability of upper unit	L^2
L	horizontal distance between vertical boundaries	L
L_c	characteristic length for individual finite element	L
L_p	pathline length	L
m_n	mass flux normal to upper boundary	M/L^2t
n	porosity	dimensionless
n_b	porosity of basal unit	dimensionless
n_f	porosity of fracture material	dimensionless

n_i	outward normal to free-surface	dimensionless
n_u	porosity of upper unit	dimensionless
Pe	Peclet Number	dimensionless
p	fluid pressure	ML/t^2
Q	total mass flow	M/t
ΔQ	percentage change in total mass flow	dimensionless
Q^*	dimensionless total flow	dimensionless
$\bar{q}$	magnitude of fluid flux	L/T
q_i	fluid flux vector	L/T
q_{n_i}	fluid flux normal to the free-surface	L/T
q_s	fluid flux along fracture zone	L/T
q_x	horizontal component of fluid flux	L/T
q_z	vertical component of fluid flux	L/T
Ra	Rayleigh Number	dimensionless
s	coordinate direction parallel to fracture element	L
S	degree of saturation	dimensionless
T	temperature	T
T_r	reference surface temperature	T
t_c	characteristic transit time along pathline	t
W	width of boundary value problem normal to page	L
WT_{max}	elevation of highest point on water table	L
ΔWT_{max}	change in elevation of highest point on water table	L
x	horizontal coordinate	L
x_0	x-coordinate at left boundary	L
x_L	x-coordinate at right boundary	L
z	vertical coordinate (elevation)	L

z_x^s	vertical coordinate at the upper boundary of domain for specified x position	L
z_x^w	vertical coordinate at the water table for specified x position	L
a_l	longitudinal thermal dispersivity	L
a_t	transverse thermal dispersivity	L
β	thermal expansivity for water	1/T
λ_{ij}^e	thermal conductivity tensor for solid-vapor-fluid composite	ML/t^3T
λ_{ij}^s	thermal conductivity tensor for solid	ML/t^3T
λ^f	fluid thermal conductivity	ML/t^3T
λ^v	vapor thermal conductivity	ML/t^3T
ρ_f	fluid density	M/L^3
ρ_o	fluid density at specified reference temperature	M/L^3
ρ_r	relative fluid density	M/L^3
θ	orientation of tangent to water table measured from horizontal	radians
μ	dynamic fluid viscosity	M/Lt

APPENDIX II

DISTINCTION BETWEEN POINT OF DETACHMENT AND HINGE POINT ON A SEEPAGE FACE

Conventional approaches to solving free-surface groundwater flow problems assume that a single point, the exit point, marks the boundary between the free-surface and the seepage face. Two conditions occur at this point; the free-surface deviates from the seepage face and the upper limit of discharge on the seepage face is defined. These conditions occur at a single point for free-surface problems similar to the triangular earth dam shown in Figure II.1. In this isothermal example, a homogeneous isotropic hydraulic conductivity K is assumed for all panels shown in Figure II.1. The horizontal base CD is impermeable while segments BC and DE are constant head boundaries with head differential $\Delta h = h_1 - h_2$. The form of free-surface AB, the length of the seepage face AE and the position of the exit point A are controlled by this head differential, the geometry of the dam, the hydraulic conductivity K and the pattern of infiltration applied on the upper surface of the dam.

In a simplified mountain groundwater flow problem, the vertical lefthand boundary of Figure II.1a becomes a symmetry boundary (Figure II.1b). At a high uniform infiltration rate (I_{z0}) the water table coincides with the ground surface across the flow system. In this case, a free-surface is absent and the entire upper surface can be considered a seepage face. The hinge point (HP) at point E on the seepage face marks the boundary between recharge and discharge and fulfills one condition of an exit point by defining the upper limit of discharge. The point of detachment A is undefined in Figure II.1b because a free-surface is absent under conditions where the water table is everywhere at the bedrock surface. Reducing the infiltration rate to

(I_z) causes a free-surface to develop (Figure II.1c) with a point of detachment (POD) at A and a hinge point (HP) at E. In this case, a single point cannot be defined that fulfills the definition of an exit point and recharge may occur on the seepage face between the POD and HP. Further reducing the infiltration rate decreases the separation between POD and HP (A and E). In low-relief topography, the separation becomes negligible and the usual exit point definition is valid. In high-relief mountainous topography, the separation between POD and HP can be substantial and must be considered in the numerical formulation.

Bear (1972, pg. 272) notes that mapping free-surface groundwater flow problems into the hodograph plane is a useful method for examining flow conditions at the boundaries. While the boundary between the free-surface and the seepage face is initially unknown in the physical plane, in the hodograph plane it is completely defined. This mapping procedure provides an analytical argument that supports the concept of separated POD and HP on seepage faces in mountainous terrain. Details on methods of mapping from the physical to hodograph planes can be found in Bear (1972) and Verruijt (1970).

Figure II.1d is the hodograph representation of the physical system of Figure II.1c. In the hodograph plane, vertical and horizontal components of fluid flux (q_x, q_z) at each point on the boundary of the physical system form the hodograph. The outline of the hodograph is defined as the locus of points marking the distal ends of specific discharge vectors originating at point C (see vectors $\mathbf{F}_1$, $\mathbf{F}_2$ and $\mathbf{F}_3$ shown in Figures II.1c and II.1d). In the mapping process, however, the spatial relationships between adjacent points in the physical plane are no longer defined in the hodograph plane. Along the horizontal impermeable boundary CD, q_z is zero and q_x increases with increasing distance from the origin to a maximum value equal to the hydraulic

conductivity K at point D. Similarly, along the vertical impermeable boundary CB, q_x is zero and the magnitude of q_z increases to a maximum with absolute value equal to the vertical infiltration rate I_z at B.

In the hodograph plane, the free-surface is described by a circular arc with radius $(K - I_z)/2$ (Bear, 1972). The highest point on the free-surface occurs at the intersection with the vertical flux axis (point B) while the lowest point occurs at the POD (point A) where the free-surface intersects the upper boundary of the domain.

Three fluid flux vectors $\mathbf{F}_1$, $\mathbf{F}_2$ and $\mathbf{F}_3$ are shown in Figure II.1c with their corresponding hodograph representation in Figure II.1d. In the physical plane, vector $\mathbf{F}_3$ is directed outward indicating discharge across the seepage face, while vector $\mathbf{F}_1$ is directed inward and indicates recharge. At the hinge point, vector $\mathbf{F}_2$ is parallel to the upper boundary in the physical plane and perpendicular to the corresponding line AD in the hodograph plane (Figure II.1d). Because $\mathbf{F}_2$ is parallel to the upper physical boundary, fluid flux normal to the boundary at point E is zero. Therefore, point E is the hinge point that marks the boundary between recharge and discharge on the seepage face.

Increasing the vertical infiltration rate from I_{z2} to I_{z1} causes the HP to move upslope from E_2 to E_1 and the POD to move upslope from A_2 to A_1 in the physical plane of Figure II.1e. The HP remains fixed in the hodograph plane (points E_1 and E_2), because this point <u>always</u> marks the point of zero flux normal to the upper boundary in the hodograph representation (Figure II.1f). Separation between POD and HP increases with increasing infiltration in the physical plane (Figure II.1e). Although the physical distance between POD and HP cannot be defined in the hodograph plane, it seems logical to assume that increasing

separation in the hodgraph plane corresponds to increasing separation in the physical plane (Figure II.1e).

In the simple systems shown in Figures II.1c and II.1e, the horizontal and vertical components of fluid flux are explicitly defined at points A, B, C, D and E in the hodograph plane (Figures II.1d and II.1f). Hydraulic head solutions obtained with the finite element method are used to estimate the free-surface configuration and calculate boundary fluxes. Boundary fluxes calculated with the finite element model correspond well to those defined in the hodograph plane.

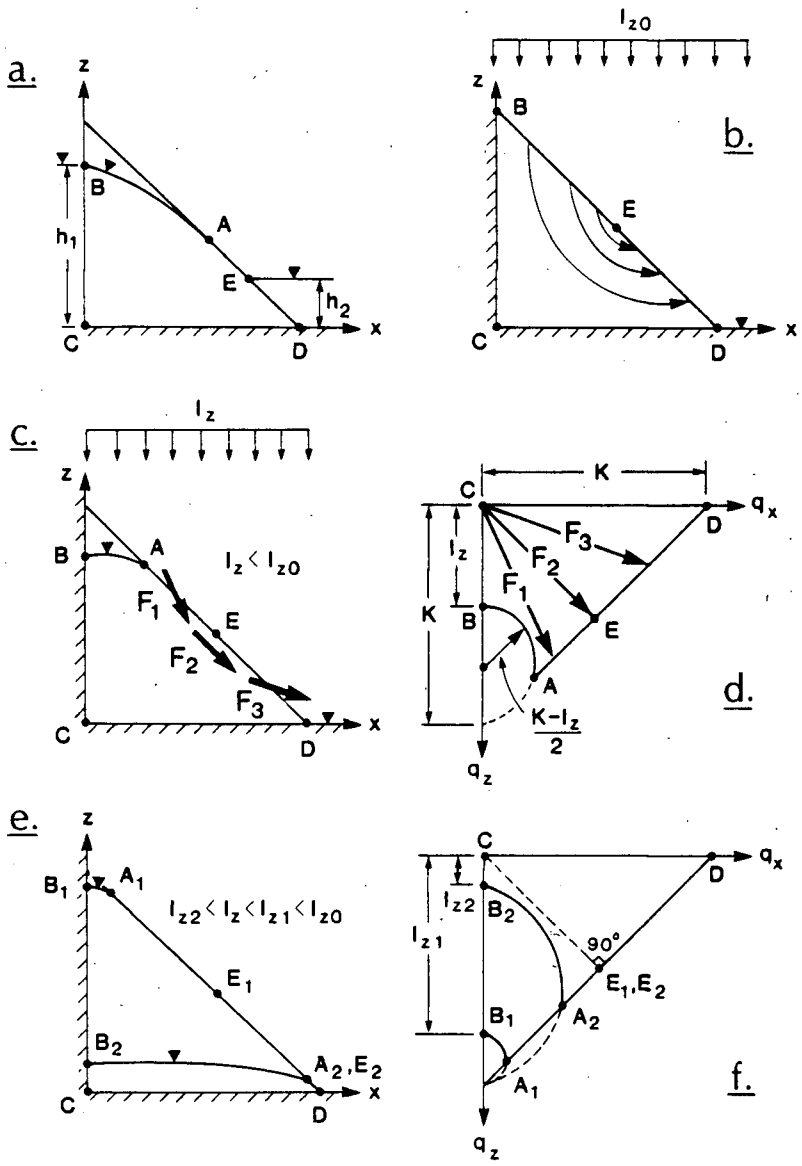

Figure II.1. Mapping water table configurations and flow patterns from physical to hodograph planes;
a. triangular dam,
b. idealized fully saturated mountain profile,
c. mountain free-surface problem with infiltration rate I_z,
d. hodograph of (c),
e. mountain free-surface problem with infiltration rates I_{z1} and I_{z2},
f. hodograph of (e).